Design of a 3D printed pre-loaded liquid lithium divertor target and testing at Magnum-PSI

Mata Gonzalez, J.

Award date:
2017

Awarding institution:
Universitat Politècnica de Catalunya

Master's Thesis

Double Master's Degree in Industrial Engineering and Nuclear Engineering

DESIGN OF A 3D PRINTED PRE-LOADED LIQUID LITHIUM DIVERTOR TARGET AND TESTING AT MAGNUM-PSI

Jaume Mata González

Eindhoven, September 2017

Supervisors: Peter Rindt & Niek Lopes Cardozo

UNIVERSITAT POLITÈCNICA DE CATALUNYA
BARCELONATECH
Escola Tècnica Superior d'Enginyeria Industrial de Barcelona
ETSEIB

TU/e Technische Universiteit Eindhoven University of Technology
Where innovation starts

ACKNOWLEDGEMENTS

I would like to express my especial appreciation to my daily supervisor Peter Rindt for his constant help and guidance during the development of the thesis. I would also like to express my deepest gratitude to Niek Lopes Cardozo, also supervisor of this project, for always finding a spot in his tight agenda to meet with me or give me some feedback.

I would also like to thank Patrick van den Bosch and Peter Hoogerhuis from Smit Röntgen for believing in this project since the first day and for being so welcoming with me. Special mention as well to Marc van Maris for sharing his expertise and spending hours with me with the electron microscope. Also express my gratitude to all DIFFER people that made possible the experiments at Magnum-PSI, especially to Thomas Morgan and Ronald Wolbeer, it was an amazing experience for me. I would like to thank as well Marius Wirtz from Jülich and Dmitry Terentyev and Chao Yin from SCK·CEN for collaborating with the material characterization of this project. Finally, I want to give special thanks to Clazien Saris and Hélène Kemperman from the fusion department at the TUe for always being so fast and efficient whenever I asked them for a favour.

To conclude this section, I would like to thank my mother for making everything so easy for me and my father for everything he ever taught me.

ABSTRACT

New concepts are being investigated to develop a divertor that can withstand the increasing heat loads and particle fluxes in future fusion reactors, one of which is the introduction of a liquid metal layer on the plasma facing surface (PFS). The goal of this project is to combine the liquid lithium divertor (LLD) concept with the 3D printed tungsten and demonstrate its feasibility under fusion-relevant conditions. To answer this question, three prototypes were designed, manufactured and tested under fusion-relevant conditions at Magnum PSI.

An initial material characterization at elevated temperature was done to the 3D printed tungsten. Results show that after stress relieving the samples, the thermal diffusivity is around 22% lower than the pure W (purity of 99.97 wt%) [1] and the tensile strength is smaller than the ITER grade W by a factor of two. Results from the tensile tests show as well that the printed tungsten did not reach plastic deformation, even when the specimens were heated to 600ºC and heat treated.

Three designs of a LLD target were made optimising the thermal stresses and the wicking flow of the Li towards the PFS. The novelty of these concepts is their gradient porous structures, going from bigger open spaces at the bottom to a more compact geometry at the top. This allows for more storage of liquid lithium (LL) closer to the base while the higher content of solid at the top improves the extraction of heat from the PFS. In addition, the channels through which the LL wicks were modelled following an elliptic profile, narrowing as they get closer to the PFS. This enhances the capillary action and keeps the flow moving towards the top surface even when the target is running out of lithium. The internal structures are formed by small elements (1-4 mm thick) to enable good expansion of the bulk material and minimize the induced thermal stresses.

FEM simulations were done with the dry targets to analyse the stress levels of the designs in a worst case scenario. Results show that for temperatures of 3000ºC at the PFS, stresses inside the structure could be up to two orders of magnitude lower than in the solid designs proposed for the ITER tiles. With LL on the surface acting as a protective layer, temperature of the bulk material is much lower and so are the induced stresses. This indicates that even if the printed material is weaker, it has sufficient tensile strength for this purpose. The LL supply rate to the surface was also estimated following the model proposed by P. Rindt [2], and calculations show that the flow is increased by at least a factor of 20 in the new designs.

During the experiments at Magnum-PSI the three prototypes were exposed for 10s at heat fluxes up to 30 MW/m^2 measured at the plasma source and estimated up to 17.5 MW/m^2 at the target. Results show a temperature plateau at the PFS with peak temperatures of 625ºC and images from IR and Phantom cameras show a stable LL bed on the surface texture, without dry spots or droplet ejections. Scanning electron microscopy reveals that, even though some damage is seen on the textured surface, large intact areas in the center of the targets are present. All these results indicate that 3D printed LLD can survive the fusion-relevant conditions and successfully confine the Li on the PFS.

These results encourage future research of the 3D printed LLD concept, which should include optimization of the printed tungsten for fusion applications and further analysis of the prototypes with longer exposures and higher heat loads. Furthermore, the low stress levels and temperatures seen in the targets open the possibility to rethink the bulk material choice and consider other candidates with better neutron resistance.

TABLE OF CONTENTS

1 INTRODUCTION

Since the discovery and control of fire, humans have been using external energy sources to improve their life. Technology progress and the rise of world population are followed by an increase in energy demand [3,4]. In the recent decades, more concern has been growing due to greenhouse effect and many agreements have been reached in order to regulate the emissions of the gases that enhance it. Two examples are the Kyoto protocol [5], signed in 1998, or the COP21, held in 2015 in Paris and seeking to promote a sustainable innovation.

With this current outlook, nuclear fusion stands as one of the energy sources with higher potential for big scale production. As mentioned in ITER's website [6], this technology has several advantages compared to nowadays energy sources: abundant energy per unit mass, sustainable and almost inexhaustible fuels, no CO_2 emissions or long-lived radioactive waste, intrinsic safety, etc.

International fusion research is currently focusing its efforts on magnetic confinement reactors, particularly in tokamak development, with the ITER project as the flagship machine. Among others, one of the main challenges for nowadays scientists and engineers is the design of a divertor that can stand the extreme heat loads and particle fluxes this component must face: for the future DEMO reactor, these conditions are expected to reach up to 20 MW/m^2 during slow transient events under cumulative neutron dose of up to 13 dpa. Such irradiation can produce crystal defects and transmutation products eventually leading to detrimental effects like reduction of heat conductivity [7]. The divertor is a PFC located at the bottom of the reactor. It acts as the exhaust of the machine, removing impurities from the plasma such as sputtered particles from the vessel. So far, the main designs have consisted of a solid target, most notably made of tungsten, but problems such as erosion and melting have motivated the study of liquid metal (LM) surfaces, with lithium as the most researched candidate [8].

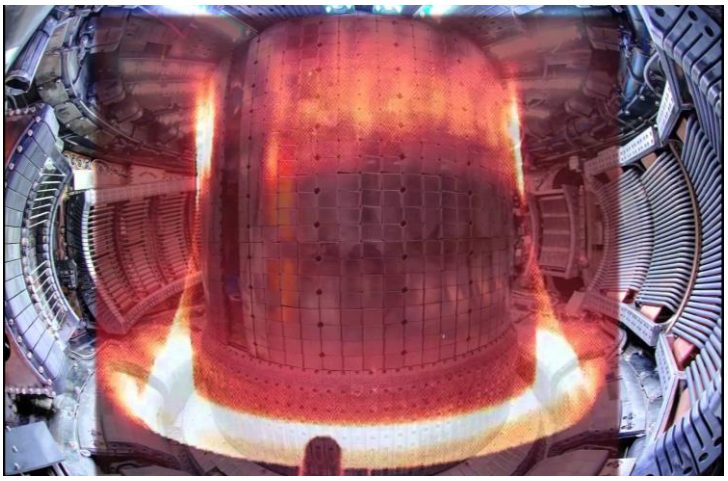

Figure 1-1 *Alcator C-Mod Tokamak [9].*

Liquid lithium acting as a first barrier brings many advantages to the divertor. Firstly, the liquid phase itself avoids problems such as radiation swelling, embrittlement or material melting, and allows the possibility to introduce filtering systems to recover the tritium. Since the LL layer does not stop neutrons, the bulk material would still suffer from radiation damage but it would be less problematic thanks to the Li interface. Secondly, due to the low Z of the lithium, contamination levels of the plasma caused by sputtering or evaporation are expected to be much lower than those of solid surface if the Li loss rate is limited [10]. In addition, vapor shielding from evaporated lithium has proven to be very effective in reducing the heat load that reaches the divertor's surface by radiating this power to the surrounding walls [11]. However, the use of LL causes some other

challenges that must be overcome, such as the stability of LL films, droplet ejection or deposition of lithium on the surface of the chamber [12]. Moreover, impurities can accumulate in the LL flow, sputtering back to the plasma and making LL no longer an effective particle pump. For this reason, recirculation and filtering systems for LL will have to be implemented at some point, introducing more complexity to the new reactors' designs.

In the last decade many research groups have been studying the behaviour of the liquid metals and LL in particular on fusion relevant surfaces. One example are the experiments of P. Fiflis et al., where the lithium contact angles for materials like tungsten or molybdenum are determined at different temperatures [13].

Besides this, many experimental tests inside the reactor have been performed to test LL limiter configurations. Results from the Frascati Tokamak Upgrade (FTU), for example, showed that the component withstood thermal loads exceeding 5 $MW \cdot m^{-2}$ although some improvement was needed in the PFS to better control the LL flow and reduce Li evaporation [14]. More experimental campaigns have been carried out in other tokamaks such as the Hefei Tokamak-7 (HT-7) [15] or its successor, the Experimental Advanced Superconducting Tokamak (EAST) [16], where static and flowing LL limiters have been tested respectively. Care must be taken, however, when results with limiter configurations are extrapolated to a divertor regime. External pressure facing the LL target is to be orders of magnitude higher in divertor plasmas and a higher equilibrium concentration of hydrogen isotopes will be reached accordingly.

Less studies have been performed with divertor configurations, so far only in the Kazakh Tokamak for Material studies (KTM) [17] and the National Spherical Torus Experiment/-Upgrade (NSTX/NSTX-U). Several campaigns have been done in the last one on LLD since 2008. Results show that LL on the divertor's surface results in more than 50% reduction in the peak heat flux hitting the target. In addition, even with significant application of lithium and its consequent evaporation, no adverse effects on plasma operations were evident [18].

The main reason that inspired this project is that, despite all the research mentioned above, there is still no evidence of LLD configurations designed for 3D printing. Metal additive manufacturing (AM) has the potential to bring new possibilities to the fusion sector due to the complex geometry capabilities and the high degree of detail achievable in the printed components. This technology combined with the LL PFS concept can be a solution to withstand the extreme conditions in future fusion reactors like DEMO, with higher heat loads and particle fluxes [7].

1.1 Objective and scope

The main goal of this project is to demonstrate the capabilities of 3D printed tungsten in the nuclear fusion world. To do so, three designs for a pre-loaded liquid lithium divertor target are presented continuing the concept proposed by P. Rindt [19]. To analyse the behaviour of the printed designs, the targets were tested under fusion conditions at a linear plasma device, the Magnum PSI [20], where divertor conditions were reproduced.

Parallel to the target design, a basic characterization at elevated temperature of the printed tungsten was also performed. The goal of this analysis is to determine the combination of different variables that optimizes the mechanical and thermal properties of the printed tungsten.

In order to adequately guide the study, the following research question will have to be answered at the end of this project:

Can a liquid lithium divertor target produced by metal 3D printing stand heat loads up to 15 MW/m^2 during 10s at Magnum PSI?

This fusion-relevant power density has been determined after considering that ITER divertor is expected to face up to 20 MW/m^2 during a normal ITER plasma pulse [1]. **Figure 1-2** shows that a pulse duration of 10s should be representative of the steady state heat load conditions:

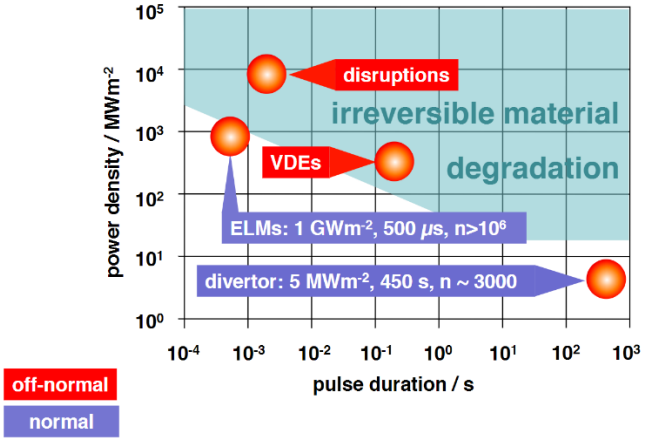

Figure 1-2 *Expected power densities and durations of different events in ITER. Background colour shows the resistance of tungsten targets for each condition. During steady state, the divertor tiles should be able to handle power densities up to 20 MW/m^2. Notice that in ITER the targets will be highly cooled whereas at Magnum PSI this system is not so effective for the designed prototypes due to the distance between the base and the PFS [1].*

The design focuses only on the target facing the plasma. No consideration is given to other elements such as the cooling system or the filtering of the LL. Furthermore, no LL supply system is included and, for this reason, a pre-loaded component is necessary.

Finally, no insight is given to radiation effects such as embrittlement or additional swelling. Magnum-PSI does not produce fusion reactions, so no neutrons are generated in the machine.

1.2 Technical breakdown

In order to address the feasibility of this novel divertor concept, the following approaches are considered during the design process:

1.2.1 Thermal approach

The designed targets are expected to face heat loads of the order of 15 MW/m^2 caused by the interaction of the ion flux with the LL at the surface. It is possible to evacuate some of this incoming heat through the cooling system incorporated in the target holder of the Magnum PSI, but this would be limited by the materials' choice and the distance between the coolant and the PFS. This makes it necessary to print the designs with a metal that can handle high temperatures without melting and offers a good thermal conductivity in order to transfer as much heat as possible away from the PFS.

Temperature inside the component must be kept between the melting and the boiling point of lithium to guarantee a good wicking action, otherwise bubbles can accumulate inside the prototypes. Evaporation of the surface lithium is expected to happen and it is positive because it generates a protection cloud known as vapour shield [21]. Nonetheless the loss rate has to be small enough to avoid an early dry-out of the prototypes and to prevent the LL from being spread all over the target chamber of Magnum PSI.

Finally, and according to the material data available when starting the project (see Appendix A), the 3D printed tungsten has lower mechanical properties than the conventional metal. For this reason, the designs have to ensure that stresses caused by the thermal load are small enough to avoid cracks or permanent deformations.

1.2.2 Lithium wicking approach

Since the targets have to be pre-loaded and no supply or pumping system is included, the LL has to flow passively towards the PFS. In the Magnum setup the plasma shots are in the horizontal plane, so the LL cannot be driven by gravity. As a consequence, the wicking of the liquid metal is guided by the capillary forces. This concept was already proposed by P. Rindt [19].

The LL supply rate has to be higher than the loss rate mentioned in the thermal approach to avoid a dry spot on the PFS. Given the geometry restrictions set by the target holder it is necessary to actuate on the permeability and pressure drop (which includes the capillary pressure term) in order to maximize the supply rate. Further analysis regarding this topic is done in section 2.2.3.

1.2.3 Test different models

The performance of the targets is expected to be very much dependent on the design, in particular the temperature and stress distributions as well as the LL wicking capacity. In addition, the combination of LL and 3D printed metal has never been tested under fusion-relevant conditions. For this reason, it has been decided to make one model as close to the original as possible since it has already been tested successfully, and two designs optimised for the 3D printing capabilities:

- The first one, named *Conventional*, is more similar to the concept proposed by P. Rindt [19], with an internal reservoir as a central element.
- Two more designs complete the set, one named *V-shape* and the other *Tree*. These two should not contain a reservoir like the first concept but store the LL all over the sample. In addition, the capillary action should be enhanced by the internal structure.

The three models are further described and analysed in chapters 5, 6 and 7.

1.2.4 Additive Manufacturing

This technology offers many advantages to the design and manufacture phases. As mentioned in the introduction, not only does it have a high degree of detail but also allows the component to have very complex geometry, with internal cavities and well defined porous structures. Nonetheless, there are some restrictions imposed to the inner parts such as the overhang or the tilt angle as no support elements can be introduced (see section 4.3). These limitations have to be taken into account when designing elements like the reservoir in the conventional concept or the geometry of the two porous designs.

1.3 Project breakdown

In order to successfully answer the research question, three intermediate phases had to be accomplished. These steps are the following:

1.3.1 Material characterization

The designs were manufactured by Smit Röntgen, one of the few companies in the world specialised in 3D printing pure tungsten [22]. This technology is very innovative for this metal and little data was available about its properties at the beginning of the project (see Appendix A). To improve the design of the prototypes, it was decided to determine some relevant properties for the project at high temperature.

The material study can be found in chapter 3.

1.3.2 Design of the targets

The first step consisted in listing all the requirements the final samples had to fulfil (see chapter 4). From this point an iterative process started with numerous brainstorm sessions and continuous analyses of the intermediate designs. Due to time restrictions, the design and the material characterization were done simultaneously, which made it necessary to estimate the properties of the printed tungsten until the last two weeks of this phase.

At the end, three concepts were selected to be tested at Magnum PSI. The design and analyses were done with the SolidWorks since an educational version was available with the UPC credentials.

The designs and analyses of the prototypes can be found in chapters 5, 6 and 7.

1.3.3 Experiments at Magnum PSI

The last phase of the project was testing the printed targets under fusion relevant conditions. Multiple shots were done to the three designs with increasing heat flux. The objective was to determine the maximum load each prototype could resist without failing (see the failure criteria in chapter 4).

The experimental setup and results of the tests can be found in chapters 8 and 9.

2 RELEVANT LITERATURE

The bibliography analysed during the execution of this project has been mostly related to liquid lithium in the fusion world and material properties of 3D printed metals. This chapter is intended to summarise the most relevant information regarding these two topics.

2.1 Prior work

P. Rindt presented a conceptual design of a pre-loaded liquid lithium divertor target for the NSTX-U reactor [19]. The proposed prototype has an internal reservoir to store the Li, and thanks to the capillary forces the LM wicks to a textured surface:

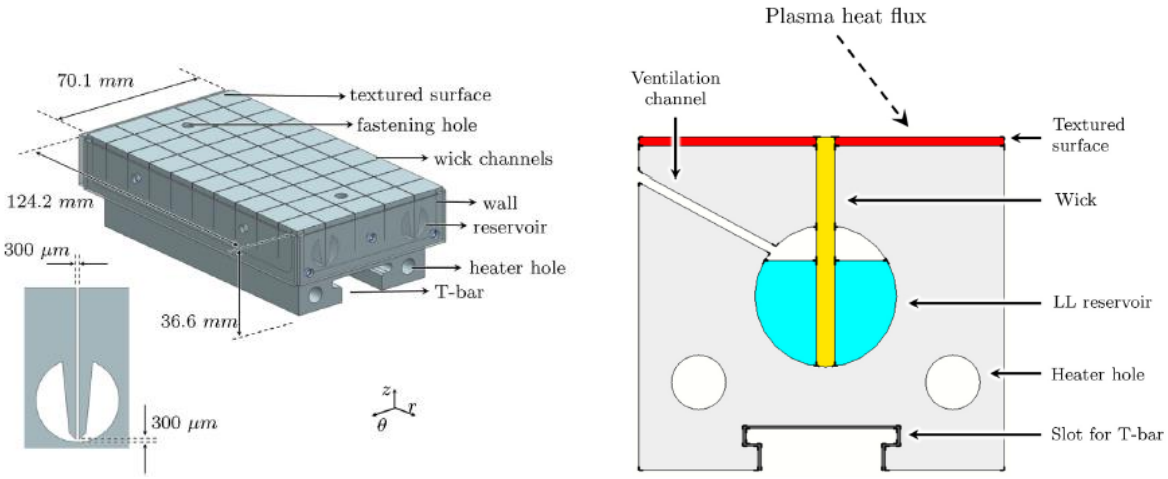

Figure 2-1 *Conceptual design of the pre-loaded liquid lithium divertor target proposed by P. Rindt [19]. The LL, stored in a reservoir, wicks to the textured surface by the action of the capillary forces. A ventilation channel connects the internal reservoir with the surrounding environment to avoid lower pressures inside the prototype that could pull the LL back to the storage volume.*

To reduce the stress induced by the thermal loads, the target is composed of several brushes that allow for expansion of the bulk material (TZM in this case). The channels between these brushes are also used as wicks through which the LL climbed to the PFS. The presence of the Li between the brushes enables as well the conduction of heat in the horizontal plane, which is essential to homogenise the temperature across the target.

This prototype was designed to be manufactured using conventional methods, so it included elements like screws, and the PFS is either a texture done with EDM technique or a welded mesh. The model proposed by P. Rindt, which is shown in **Figure 2-1**, was updated and adapted to be tested at Magnum PSI. The exposed targets look like this:

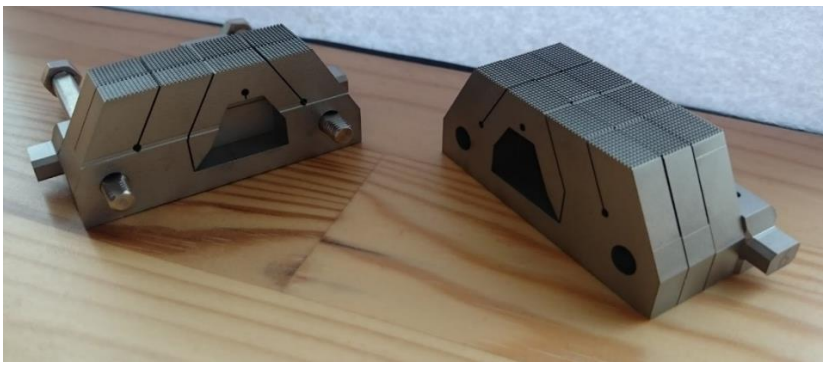

Figure 2-2 *Prototype of a pre-loaded liquid lithium divertor target proposed by P. Rindt. This particular model has a texture on the PFS done with EDM. This design was tested at Magnum PSI in April 2017 [2].*

2.2 Liquid Lithium as Plasma Facing Component

Before starting with the designs, it was necessary to understand the behaviour of this liquid metal in order to optimize the wicking action inside the component or the texturing of the PFS.

2.2.1 Capillary Porous System (CPS)

Two main solutions are currently being investigated to embed the liquid lithium on the PFS of limiters and divertors: Free flow and CPS proposals.

The first one relies on a system of trenches through which the LL flows. This movement is generated by the thermoelectric magnetohydrodynamics (TEMHD) forces that origin with the combination of the thermoelectric effect between the Li and the metal plate and the external magnetic field [23].

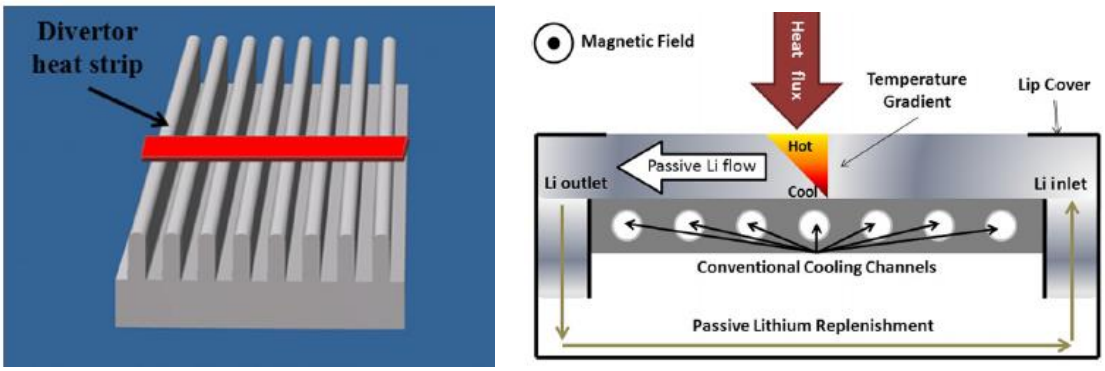

Figure 2-3 *Lithium Metal Infused Trenches (LiMIT) concept. The trenches run in the radial (poloidal) direction such that they lie primarily perpendicular to the toroidal magnetic field and the divertor heat stripe. This concept uses the TEMHD effect caused by the temperature gradient for heat removal and to drive the LL through the slots of the metal plate [23].*

This system offers more protection to the solid part of the target and is an active removal of particles and heat load due to the higher speeds of the Li flow (favours particle transport and convection). The problem is that the LL on the surface presents higher splashing and flow instabilities due to the weaker attachment to the surface [24]. As a result, higher quantities of Li are ejected to the plasma.

The targets in this project are based on the second concept, the CPS, initially proposed by V.A. Evtikhin et al. [25]. This system relies on the capillary forces that arise when a LM is contained in a porous substrate. Due to the high surface tension of LMs and with an adequate pore size, a flow can move passively against gravity or avoid splashing under MHD induced forces. Experiments performed at NSTX with a LLD configuration show no macroscopic ejection of liquid metal even under peak current densities into the PFCs exceeding 100 kA/m^2 [26]:

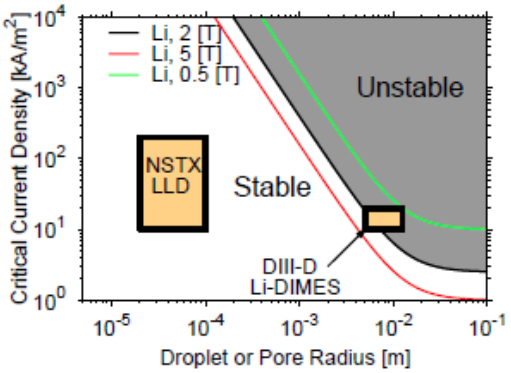

Figure 2-4 *Stability diagram for LL under electromagnetic body forces (with gravity and surface tension stabilizing) for different magnetic fields. Operating spaces for NSTX LLD and Li-DIMES experiment are also indicated, with magnetic fields of 0.5 and 2 T respectively. No Li ejection was observed during the 2010 campaign at NSTX [26].*

The capillary porous system is a simpler and more mature concept than the free flow and requires less amount of LM. It also solves the ejection problem and allows for a more flexible choice of the geometry in the PFS as seen in **Figure 2-5**. The problem with this option is that more heat is transferred to the solid part of the target as the LM is almost stationary. This also reduces the particle pumping effect that characterizes the free flow concept.

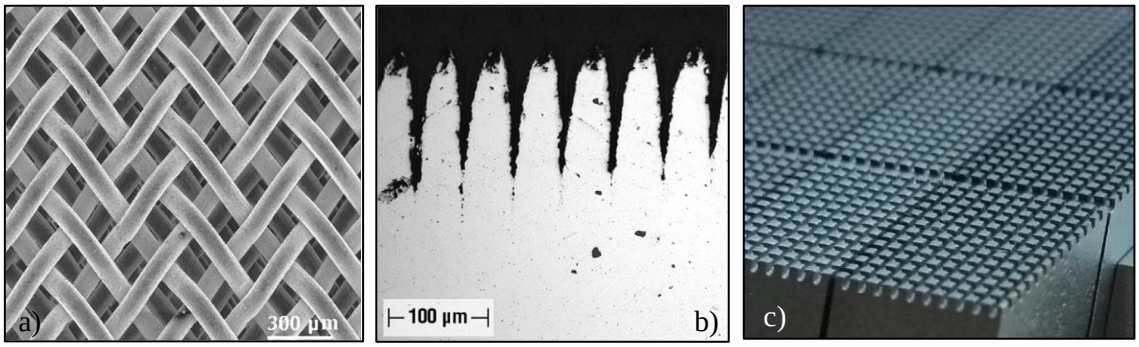

Figure 2-5 *From left to right: a) Mo wire mesh with R_{eff} = 75 µm and d_{wire} = 100 µm [27]. b) Laser textured surface on TZM substrate with 50 µm spacing and a total depth below 160 µm [28]. c) EDM textured surface on TZM substrate where channels are 300 µm wide and 450 µm deep [2]. These are three examples of the many CPS designs tested to confine the LL on the PFS of the targets when they are exposed to plasmas.*

2.2.2 Vapour Shielding effect

Another advantage of the CPS is that fusion relevant heat fluxes can easily evaporate the LM on the surface, creating a protection cloud known as vapour shielding effect. This acts as an interface between the plasma and the solid and radiates part of the heat load going to the target. An experiment performed by GG van Eden with liquid tin and molybdenum as bulk material showed a 1/3 reduction of the incident power flux thanks to the effect of the vapour shielding [21]:

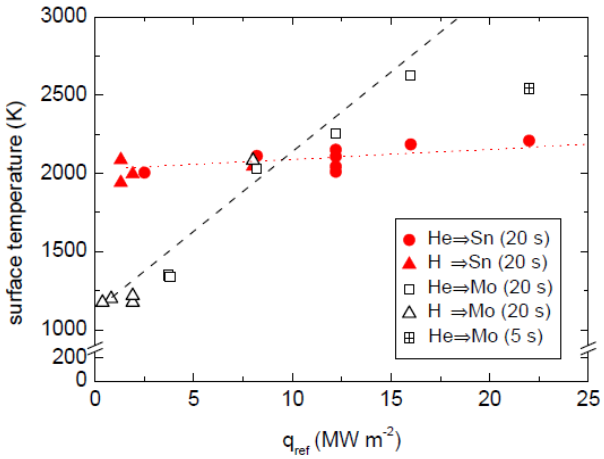

Figure 2-6 *Surface temperature measurements of a target exposed to plasma at Magnum PSI with (red markers) and without (white markers) liquid tin on the PFS. For wetted targets (red) temperature stays very constant regardless of the heat flux, whereas for dry targets (white) temperature increases severely with the impinging flux* [21].

2.2.3 Liquid lithium loss rate

To sustain this vapour shield it is necessary to pay a toll. While part of the LM is re-deposited on the target's surface, the rest is lost to the plasma or the surrounding walls. The amount lost depends on the liquid metal itself but also on the particle flux or the type of plasma. TW Abrams did a deep study in his PhD dissertation about erosion and re-deposition of lithium and boron coatings under high flux plasmas [29]. One of his conclusions is that the loss rate can be determined using an erosion yield and the impinging particle flux. According to Abrams, the sputtering of lithium reaches a certain yield with temperature when bombarded by high flux of deuterium (D) particles. Saturation of the LL with D is reached and so the atomic erosion of the liquid metal layer is limited:

$$\Gamma_{Li\ loss,gross} = Y \cdot \Gamma_{ion}$$

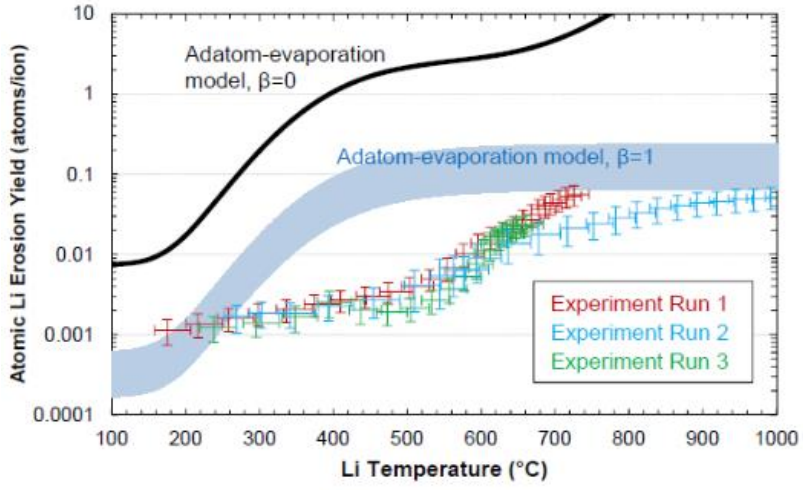

Figure 2-7 *Atomic Li erosion yields vs. temperature during deuterium plasma bombardment inferred from three different sets of experimental measurements of Li-I emission at Magnum-PSI. The predictions of the adatom-evaporation mixed-material model done by Abrams for D/Li concentration β = 1 (expected) and β = 0 are also overlaid. With D saturation there is an erosion yield around 0.1 atoms/ion whereas with no D in the Li the evaporation rate increases with temperature* [29].

The sputtered and evaporated lithium goes to the plasma and ionizes. At this point the Li ion is driven by the magnetic field and can return to the surface, where it re-deposits. The same ion can also recombine with an electron from the plasma, forming a neutral atom and depositing again on the target. This re-deposition, expressed with the term *R*, reduces the gross loss rate and can be estimated with the following expression:

$$\Gamma_{Li\ loss,net} = (1 - R) \cdot \Gamma_{Li\ loss,gross} = (1 - R) \cdot Y \cdot \Gamma_{ion}$$

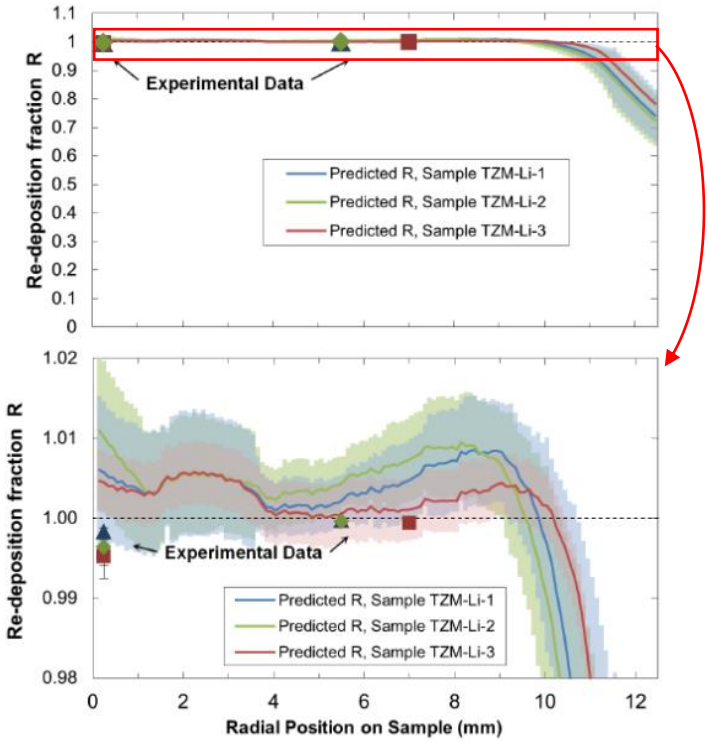

Figure 2-8 *Predicted re-deposition fractions in Magnum-PSI with error bands for three Li and TZM disc targets [29]. Measured re-deposition fractions are also overlaid. It can be observed that for 25 mm diameter samples, the re-deposition fraction for Li in Magnum-PSI can be almost 100%. This reduces considerable the LL loss rate.*

Once the net loss rate is determined the volumetric loss can be found with a simple factor conversion:

$$Volumetric\ loss = \Gamma_{Li\ loss,net} \cdot \frac{1}{N_A} \cdot A \cdot \frac{1}{\rho} \cdot S$$

Where NA is the Avogadro's number, A the atomic mass of lithium, ρ the liquid lithium's density at 625ºC [30] and S the area of the plasma facing surface.

According to the geometrical restrictions imposed by Magnum-PSI (see section 4.1) and the numbers proposed by TW Abrams to calculate the LL net loss rate [29], a rough estimation for the expected volumetric loss during the experiments at Magnum PSI is:

$$Volumetric\ loss = [(1 - 0.95) \cdot 0.1 \cdot (2 \cdot 10^{24})] \cdot \frac{1}{6.023 \cdot 10^{23}} \cdot 6.941 \cdot \frac{10^{-3}}{0.476} = \mathbf{2.42 \cdot 10^{-4}} \frac{\boldsymbol{l}}{\boldsymbol{s \cdot m^2}}$$

The particle flux has been set at $2 \cdot 10^{24}$ $m^{-2} \cdot s^{-1}$ since it is the number proposed by Abrams for his experiments at Magnum PSI. A worst-case scenario has been considered, so the re-deposition fraction has been set at 0.95 even though experimental results show it was always above 0.99.

2.2.4 Liquid lithium supply rate to the Plasma Facing Surface

In order to avoid dry spots on the top surface of the target, the lost Li has to be replenished at least at the same speed as the erosion rate described above. Li is stored inside the target and wicks to the surface by capillary action. According to Darcy's law, at constant elevation (considered in this case as the component is few millimetres high) the volumetric flow $\dot{Q}$ through a porous medium can be determined by the following expression:

$$\dot{Q} = -\frac{k \cdot A \cdot \Delta P}{\mu \cdot L}$$

Where k is the intrinsic permeability of the medium (m^2), A the porous cross section of the target (m^2), ΔP the total pressure drop between the plasma facing surface and the lowest section filled with lithium (Pa), μ is the dynamic viscosity of the LL (Pa·s) and L the length over which the pressure drop takes place (m).

To make the wicking flow big enough it is possible to actuate on the pressure drop, the permeability and the cross section. The length is limited by the dimensions of the prototype and the LL viscosity is a temperature dependant property and cannot be altered.

a) Permeability

According to a study performed by J.F. Despois and A. Mortensen [31] the permeability of open porous material can be calculated with this equation:

$$k = \frac{\Delta \cdot r^2}{\pi}\left[\frac{\Delta - \Delta_0}{3(1-\Delta_0)}\right]^{3/2}$$

Where Δ is the pore volume fraction, r is the original particle radius (m) and Δ_0 is a constant value depending on the geometry of the pores. For porous media, r is very close to the average pore radius, so this formula shows that with higher porosity and bigger pore dimensions, permeability can be increased. As a result, the wicking flow increases.

b) Pressure drop

In these conditions, it is the result of the forward capillary pressure minus the backward capillary pressure and the magnetic drag in each section [19]:

$$\Delta P = \frac{2 \cdot \gamma \cdot \cos\alpha}{r_u} - \frac{2 \cdot \gamma \cdot \cos\alpha}{r_l} - \sum_{i=1}^{n} \sigma \cdot B^2 \cdot L_i \cdot \frac{dL_i}{dt}$$

Where γ is the surface tension of the LL (N/m), α is the contact angle between LL and tungsten (rad), r_u and r_l are the upper and lower pore radius (m), σ is the electrical conductivity of LL (S/m), B is the magnetic field strength (T), dLi/dt is the speed in a specific section (m/s) and Li the length of the section (m).

This expression shows that the bigger the difference between the upper and lower pore size, the higher the pressure drop and thus a higher wicking flow. Note that the upper pore must be smaller than the lower pore to favour the capillary action towards the PFS.

The other parameters of this expression could not be altered during the design process as they depend on the materials chosen or the settings at Magnum PSI.

2.3 3D printed tungsten and Smit Röntgen

In the beginning of the project, many materials were studied in order to find a suitable 3D printable metal that could withstand fusion relevant conditions. Fortunately, a collaboration could soon be established between Smit Röntgen and the TUe. As mentioned in the project breakdown, this company was among the firsts manufacturers to print pure tungsten parts and is nowadays a leader in this industry. Since Smit Röntgen facilities are next to Eindhoven and tungsten is the material proposed for ITER's divertor tiles, it was decided to build the targets with 3D printed pure tungsten.

Smit Röntgen started a decade ago in the 3D printing industry developing and manufacturing pure tungsten parts for medical applications. Currently they are also working on components for other uses such as thermal and radiation shielding or balance weights.

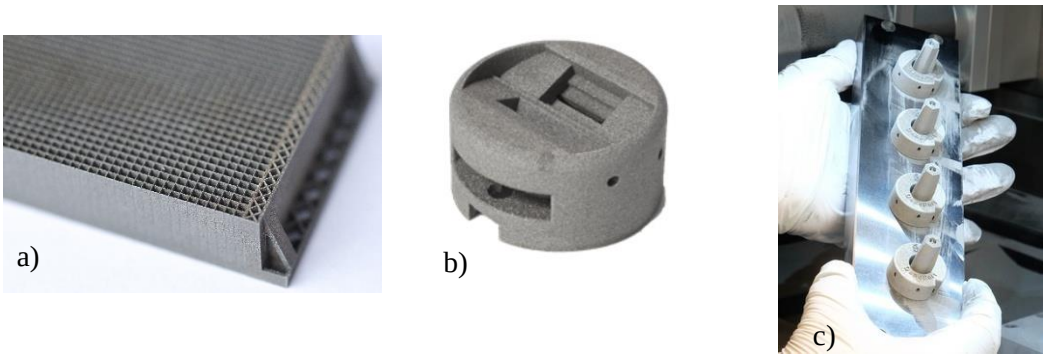

Figure 2-9 *From left to right, a) collimator for the medical industry (e.g. for X-ray beam), b) thermal and radiation shielding (e.g. to protect instrumentation) and c) balance weights (e.g. for the aerospace industry)* [22]

2.3.1 Powder Bed Laser Melting

Smit Röntgen uses Powder Bed Laser Melting (PBLM) technique to print the parts. With this method they are capable of reaching very high precision and low porosities in the manufactured components: minimum tolerance achievable of 25 μm and maximum relative density of 97%.

PBLM, also known as Selective Laser Melting (SLM), is a 3D printing technique that uses a laser to melt successive layers of metallic powder. A CAD 3D file is sent to the printer where the design is sliced into 2D layers with a thickness that can vary depending on the desired detail and the capabilities of the printer. The laser heats and melts the particles according to the sliced CAD drawing and once the layer is completed, the printed part moves one step down so that the bed of metallic powder covers again all the surface.

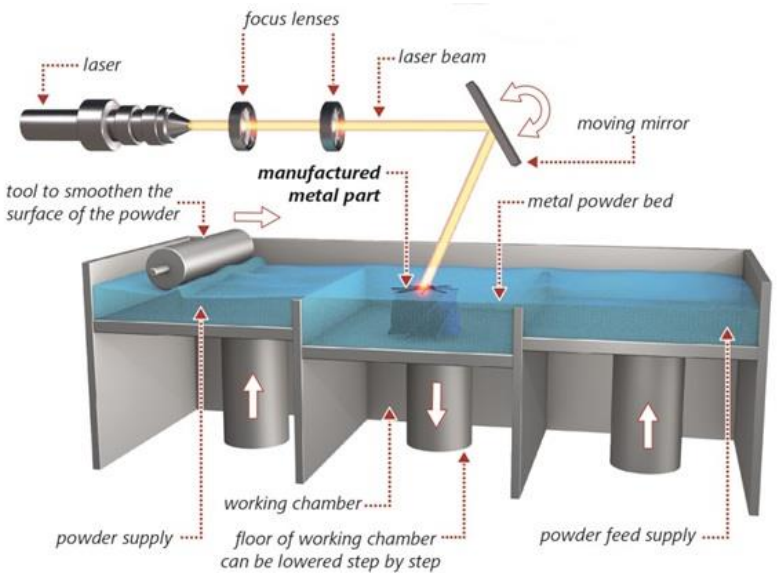

Figure 2-10 *Schematic of the printing process using SLM technique. The powder is supplied by independent chambers and a smoothing tool. The manufactured part is placed in the working chamber with a platform that is lowered as the layers are printed. A mirror directs the laser beam to melt the particles according to the CAD file* [32].

2.3.2 Printing tungsten

No information can be disclosed about the calibrations used by Smit Röntgen to print the tungsten parts. Nonetheless, an American manufacturer of 3D printers capable of printing pure tungsten published in February 2016 a paper explaining the technology they use [33]. Common printable metals with lower melting temperatures and thermal conductivities, such as Aluminium or Titanium alloys, use Continuous-Wave or long-pulsed lasers with pulse durations that can go down to the nanosecond or picosecond scale. To be able to print tungsten or other high temperature resistant materials, the mechanism proposed by this company is to reduce the pulse duration of the laser to the femtosecond scale. With this solution, problems induced by simply increasing the energy of the laser, such as heat diffusion outside the focal volume or residual stress, are avoided. In addition, the company claims this technology can print features as small as 10 µm and reach relative densities up to 99%.

No details are given in the paper about how the pulse duration is reduced to 10^{-15} s. It does mention, however, that the laser beam has a maximum output pulse energy of 500 µJ and an averaged peak power of 1 kW.

2.4 Magnum PSI

The experiments of the targets were performed at Magnum-PSI (Plasma Surface Interactions). This machine is a linear plasma generator built in the DIFFER PSI-Lab, in Eindhoven (The Netherlands), designed to study plasma-wall interactions in a big fusion reactor such as ITER. A cascaded arc plasma source produces a hot, dense plasma which is guided to the target by a superconducting magnet.

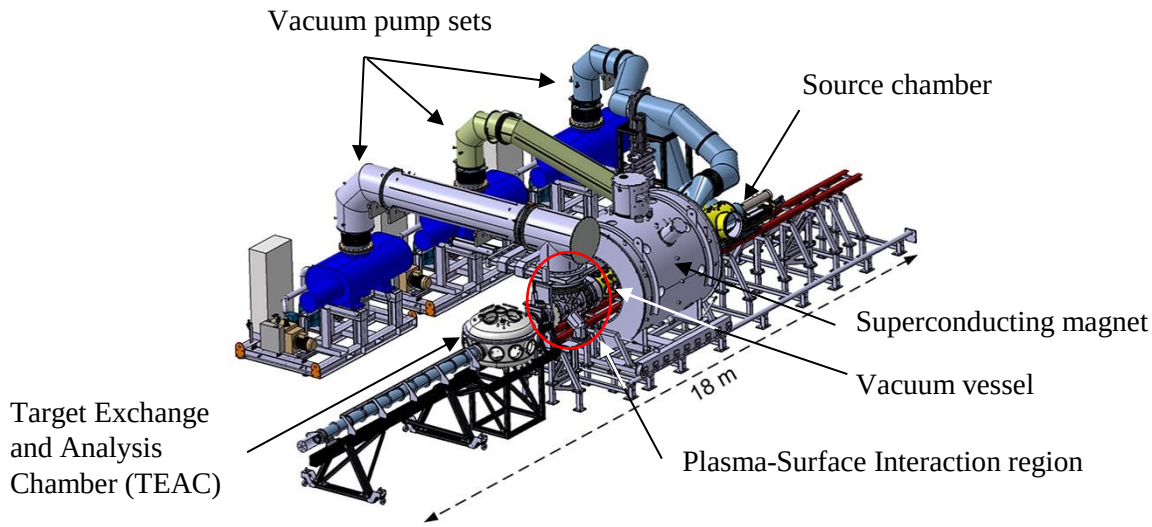

Figure 2-11 *Magnum PSI set-up in a 3-dimensional view. The plasma is produced in the source chamber and is guided to the target by the superconducting magnet. All the volume from the source chamber to the TEAC is under vacuum during operation. The vacuum vessel (yellow component) is divided into three areas, which is why the three pump sets are needed [34].*

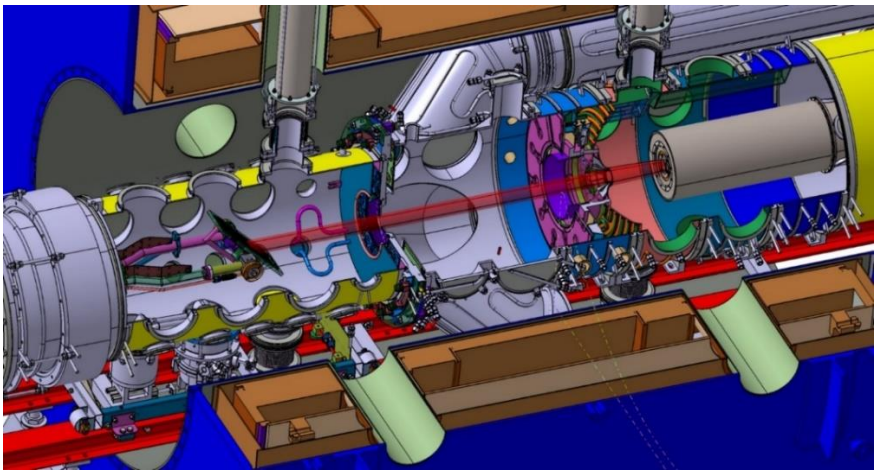

Figure 2-12 *3D sketch showing the interior of the vacuum vessel of Magnum PSI during a shot. On the left it is possible to see the target with a certain tilt in the exposure region, and on the right there is the source. The plasma beam is coloured in red. Notice that the vessel is divided into three compartments and they are all confined inside the superconducting magnet (big blue and brown structure) [2].*

The linear plasma device was designed to study plasma-surface interactions under the so-called 'strongly-coupled' regime. This is reached when the mean free-path of the particles released from the surface is smaller than the plasma size and they are trapped in the plasma-surface interaction region. For this purpose, the most relevant parameters regarding the performance of Magnum PSI are the following:

- Particle flux (Γ): between 10^{23} and 10^{25} $m^{-2}\cdot s^{-1}$
- Electron density (n_e): between 10^{19} and 10^{21} m^{-3}
- Electron temperature (T_e): up to 10 eV
- Magnetic field: up to 2.5 T in steady state
- Heat flux: above 50 MW/m^2 at the source in steady state
- Pulsed source: transient plasma up to 2 $GW\cdot m^{-2}$ with a repetition rate of 70 Hz
- Different gases such as H, He or Ar can be used to create the plasma

More information regarding the capabilities of Magnum PSI can be found on [20]. Notice that this article was written before the upgrade of the machine. It now has a superconducting magnet, but at that moment the magnetic field was generated with copper coils.

Many diagnostics are available to monitor relevant parameters during the experiments: calorimetry of the cooling water, Thomson scattering, pyrometry and infrared thermography, fast and slow camera imaging (Phantom and PIXIS respectively), optical emission spectroscopy, etc. In addition, customized equipment can be installed to the setup if needed, such as gauges through the clamping rings to monitor internal temperature of the targets, a quartz crystal microbalance to determine the loss rate of the exposed material or a bolometer to measure the power radiated by the target.

Further description of the diagnostics including their setup, calibration and error analysis can be found in TW Abrams' PhD dissertation [29].

3 MATERIAL CHARACTERIZATION

A characterization of the printed tungsten was performed by Smit Röntgen, but this study was at room temperature (RT), where the tungsten is in the brittle regime. In this project, the imposed fusion-relevant environment requires the target to operate at temperatures where the tungsten is in the ductile regime, above 400ºC [35]. Metals tend to behave differently depending on whether their temperature is below or above the Ductile to Brittle Transition Temperature (DBTT). For this reason, and given the different behaviour between printed and conventional metals, new measurements of the mechanical and thermal properties of the printed tungsten had to be performed.

The main goal of this material analysis is to find the combination of variables that make the tungsten as strong as possible, given the common fact among printed metals to have lower strength than the same conventional material [36]. In addition, these measurements helped during the last phase of the design process.

To reduce the duration of the experiments, the heating/cooling processes and to minimize the printing costs, all the tests were performed using micro specimens. Thanks to the TEC collaboration between the TUe, SCK-CEN and the Jülich Research Centre (FZJ), the tensile tests were done at SCK-CEN (Belgium) while the thermal diffusivity was measured at FZJ (Germany).

3.1 Definitive test plan

To optimise the printed tungsten for the fusion-relevant conditions, different combinations of temperature, heat treatment, relative density and surface finish were proposed. The variables included in the test plan are the following:

a) **Temperature** – The equipment used for the mechanical tests cannot reach temperatures above 600ºC. For this reason, tensile tests were done at 350ºC, 475ºC and 600ºC and thermal diffusivity was measured at steps of 100ºC until 600ºC. Experiments had to be performed over the DBTT to avoid brittle behaviour of the tungsten, hence this minimum temperature.

b) **Heat Treatment** – In the datasheet provided by Smit Röntgen (see Appendix A), the ultimate tensile strength at room temperature for the printed material is significantly lower than for the conventional tungsten (>35 vs 1000 MPa [37]). According to a study performed at NIST [38], stress relieved austenitic stainless steel printed with SLM shows higher tensile strength and hardness but slightly lower yield strength than the same material without heat treatment. This motivated the introduction of annealing treatments to this characterization. In addition to the As printed samples, two heat treatments were considered: stress relief and recrystallization. These treatments had to be done under vacuum conditions to avoid problems like oxidation of the tungsten, as the rate increases at temperatures above 200ºC in dry atmosphere [39].

   i. Stress relief – two hours at 1000ºC [1]. Performed at the DIFFER vacuum furnace.
   ii. Recrystallization – one hour at 1600ºC [1]. Had to be performed at FZJ since the vacuum furnace at DIFFER could not reach temperatures above 1200ºC.

c) **Relative density** – Higher porosity in the material increases the permeability but reduces the strength, thermal conductivity and electrical conductivity [40&41]. One option for the designs is to include regions with low relative density to create a sponge-like layer that would absorb the LL. Tests were performed with higher (93%) and lower (84%) relative density to observe how this variable influences the response of the printed tungsten.

d) **Surface finish** – After the printing, the sample can be post-processed in the Smit Röntgen facilities using EDM to reach better surface finish. One hypothesis was that by using this technique some surface imperfections could be eliminated, such as external pre-cracks originated due to rapid cooling. In the test plan, most samples would be tested As printed and some would undergo an EDM post-processing.

Once the testing conditions were decided and an agreement was reached regarding the number of samples, the characterization of the printed tungsten was ready to start. The chosen approach was to test a reference condition and then proceed by changing one variable at a time to check the influence this had on the material's response. This base condition was set at:

a) Temperature = 600ºC: Higher temperatures were expected in Magnum PSI.
b) Heat treatment = Stress relief: Expected to improve the mechanical properties [32].
c) Relative density = High: Expected to improve the mechanical and thermal properties [40&41].
d) Surface finish = As printed: EDM post-processing was very time demanding.

Three repetitions of each condition should be measured to reduce the deviation of the results. The measurements included in the plan are summarised in the following sections:

3.1.1 Tensile test

With this experiment the Yield strength and the Young's modulus were determined. These tests were performed at SCK-CEN using tensile specimens (see Appendix B). The proposed plan was:

Table 3-1 *Proposed test plan to measure the mechanical properties of the printed tungsten.*

#	TEMPERATURE [ºC]	HEAT TREATMENT	REL. DENSITY	SURFACE FINISH
3	600	Stress relief	93%	As printed
3	350	Stress relief	93%	As printed
3	475	Stress relief	93%	As printed
3	600	As printed	93%	As printed
3	600	Recrystallization	93%	As printed
3	600	Stress relief	84%	As printed
3	600	Stress relief	93%	EDM post-processed

3.1.2 Laser Flash Analysis

With this test the thermal diffusivity was determined. These experiments were performed at FZJ using disc specimens (see Appendix B). Flat parallel surfaces of the discs are required for a better measurement of this property, so it was decided to post-process all the round surfaces with EDM. Before sending the samples to Jülich, glass blasting was done to the discs to remove the copper layers formed by the EDM wire. The proposed plan was:

Table 3-2 *Proposed test plan to measure the thermal diffusivity of the printed tungsten.*

#	TEMPERATURE [ºC]	HEAT TREATMENT	REL. DENSITY	SURFACE FINISH
3	RT – 600	Stress relief	93%	EDM post-processed
3	RT – 600	As printed	93%	EDM post-processed
3	RT – 600	Recrystallization	93%	EDM post-processed
3	RT – 600	Stress relief	84%	EDM post-processed

3.2 Results

This section shows the preliminary results from the tensile tests and the laser flash analyses done so far. The material characterization is not yet completed, but the measurements presented had never been done before and have been useful during the design phase of the prototypes.

It must be noted that only one sample was tested at every condition. One of the drawbacks of the metal AM industry is the poor repeatability of the printed parts, so big uncertainties are linked to these results.

3.2.1 Tensile test

The experiments show that in every measurement the printed samples failed without reaching plastic deformation. The reason behind this prompt rupture can be the presence of numerous cracks formed during the printing process. When compared with the ITER grade pure tungsten, the printed samples are weaker (around 50%) but in the same order of magnitude.

Results show as well that the sample with 93% relative density presents a fracture strength 37% higher than the sample with 84% relative density. Regarding the temperature effect, the specimen tested at 350ºC broke before the same specimen tested at 600ºC, reaching a fracture strength around 10% lower. Finally, both heat treatments increase the elasticity of the material (reduce the Young's Modulus), but the stress relief increases the fracture stress around 20% while the recrystallization reduces this peak by 5%.

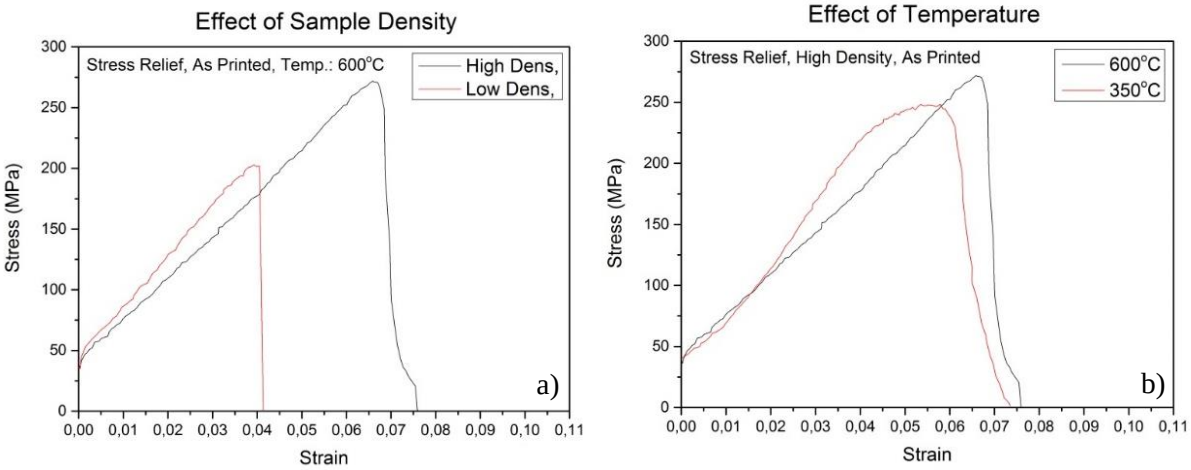

Figure 3-1 *a) Strain-Stress Curve of 3D-printed W at different temperatures. Unlike with conventional metals, at higher temperature the material shows higher strength. b) The same curve but with different densities. As expected, the sample with lower density breaks before the high-density specimen.*

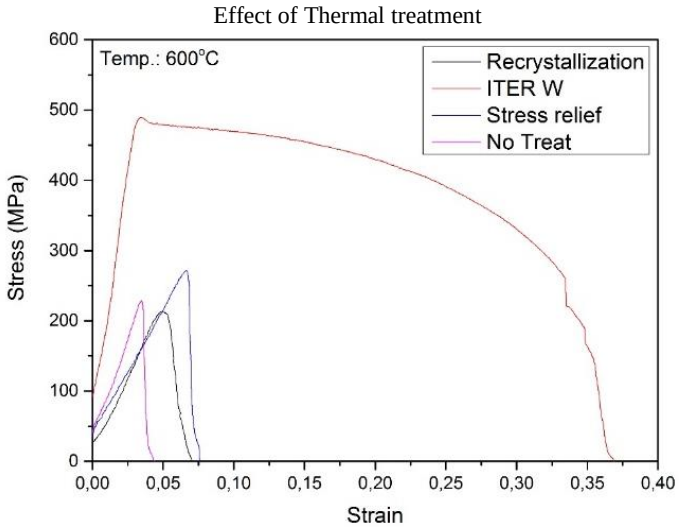

Figure 3-2 *Strain-Stress Curve of 3D-printed W (600ºC, high density, as printed) at different thermal treatments vs ITER grade pure W. Both heat treatments reduce the Young's modulus of the printed material, making it more ductile. As expected, recrystallization reduces the strength of the tungsten, but in this case the stress relief increases it, reaching a failure strength above 270 MPa. Finally, a comparison can be seen with the optimised W used for ITER. The printed tungsten, although weaker, is in the same order of magnitude.*

In conclusion, to obtain the strongest printed tungsten with the studied variables it is necessary to print it with the highest relative density achievable and to perform a stress relief at 1000ºC during 2h. According to these results, temperature does not influence significantly the strength of the printed tungsten, but the specimen at 600ºC performs better than the one at 350ºC. Compared to the optimised W grade for ITER, the mechanical properties of the printed tungsten are lower but in the same order of magnitude.

3.2.2 Laser Flash Analysis

The experiments done at FZJ show that thermal diffusivity is increased by 10% with stress relief treatment and with density, being an almost linear relation with the latter. As expected, an increase in temperature reduces the thermal diffusivity of the material (-34% from 600ºC to RT) and, as a consequence, the thermal conductivity.

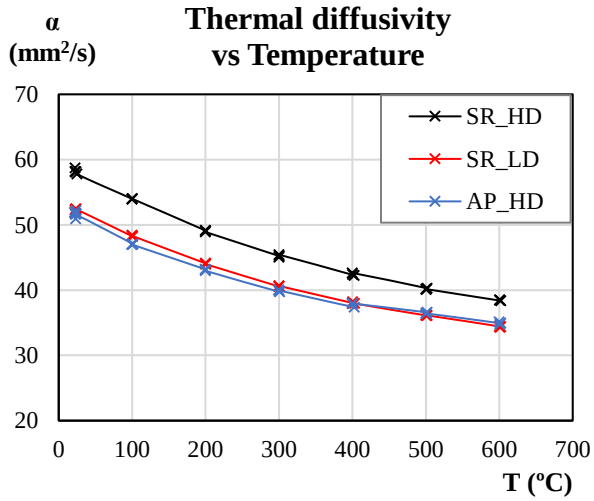

Figure 3-3 *Thermal diffusivity of the 3D printed tungsten at different temperatures. Each curve represents one sample, and their characteristics can be found in* ***Table 3-3****.*

Table 3-3 *Characteristics of the tested disc samples*

	Code	Heat treatment	Density (g/cm³)	Thickness
	SR_HD	Stress relief	High (18.2517)	3.12 mm
	SR_LD	Stress relief	Low (16.9467)	3.18 mm
	AP_HD	No treatment	High (18.2178)	3.13 mm

4 DESIGN SPECIFICATIONS

To be able to obtain successful final designs the following requirements have to be fulfilled:

4.1 Target requirements

- The designs must be 3D printed with a fusion relevant high Z material. This group have good compatibility with Li at high temperatures [24] and is favoured over carbon-based materials in the design of LL PFC because the carbon easily absorbs Li. In addition, C–H composites and carbon dust are formed [19].

- The goal of the project is to design a divertor target that operates with LL on the PFS, so the surface must be wetted during all the exposure time. To have a dry spot on the PFS which cannot be re-wetted is considered as a failure criterion.

- The LL on the surface must be stable to droplet ejection. Big loss of the LL is not desirable as it increases the impurities in the plasma and reduces the time until the targets get dry.

- The prototypes must be pre-loaded with LL before the experiment at Magnum PSI. No supply system is included in the designs, so an internal storage system is necessary to guarantee a flow of liquid lithium to the PFS.

- At least 1 g of lithium should be stored inside the target. This is to guarantee a minimum exposure time before the samples dry out.

- The final designs must be compatible with the target holder of the Magnum PSI and the clamping rings. Therefore, the prototypes should have a top hat shape with a base of 30 mm diameter and <4 mm height and the main body should be 25 mm diameter.

4.2 Thermal specifications

- The pre-loaded target should be able to stand peak heat fluxes of 15 MW/m^2 during at least 10s. This value has been set considering the expected heat load received at the divertor region during a normal ITER plasma pulse, which can go up to 20 MW/m^2 [1].

- The chosen bulk material must resist high temperatures without melting (up to lithium boiling point, around 1330ºC) and have good thermal conductivity. The model proposed by P. Rindt shows peak temperatures of 1470 K for peak heat fluxes of 10 MW/m^2 [19].

- The component cannot suffer plastic deformation or reach recrystallization during the plasma exposure. This is considered as another failure criterion since the target can no longer be used because of the permanent modification in the geometry and the material properties.

4.3 Additive Manufacturing Constraints

- A hole is needed to extract the material dust from the inside of the component after the printing process. According to the engineers from Smit Röntgen, the diameter should be at least 0.5 mm.

- The internal geometry of the targets must be compatible with 3D printing capabilities of Smit Röntgen:

    - ✓ Minimum tolerance achievable of 25 µm.
    - ✓ Minimum feature size of 100 µm (1 mm to reach maximum relative density).
    - ✓ Maximum horizontal overhang of 1 mm.
    - ✓ Tilt angle should be kept above 45º.

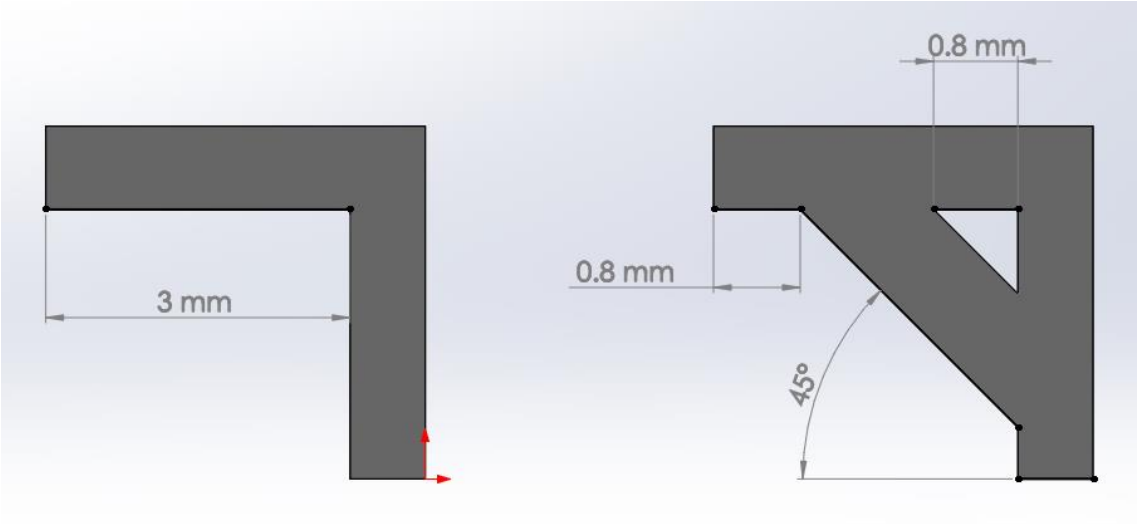

Figure 4-1 *The design on the left will have problems due to excessive overhang during the printing process. If the structure shown on the right is used this problem can be solved. The indicated 45º is the tilt angle. If this is smaller, problems such as whiskers or drooping could occur at the bottom of the tilted bar.*

5 DESIGN

In this chapter, the subsystems in which the design has been divided will be first defined. Next, the comparison criteria for the different concepts will be established. Finally, the concepts considered for all subsystems will be discussed, concluding with the chosen designs.

5.1 Subsystems of the porous designs

Three different designs were tested at Magnum PSI: two porous models and one conventional. This last one is an adaptation of the concept proposed by P. Rindt [2] and some subsystems presented in this section are not applied to its design.

1. Plasma facing surface

Here is where the plasma hits the target, and to protect the bulk material from the high heat loads a LL bed must be present in the interface during all the exposure. The surface should include some kind of structure to confine the lithium, avoid droplet emission and keep the loss rate of this liquid metal at a reasonable rate. At the same time, this surface needs openings to allow the lithium to wick upwards, but there are no specifications applying to its geometry.

2. Lithium storage

As no supply system is considered, it is necessary to have enough empty space inside the target to pre-load it with LL. The reservoir can be kept similar to the one proposed by P. Rindt, with a big central volume, but with the porous geometry this element can also be integrated within the internal structure. All the wicking channels and cavities can form a “distributed reservoir”.

3. Lithium transport

Like in the concept proposed by P. Rindt, the LL in this case is also driven by the capillary forces as no pumping system is considered. The novelty in these designs is that the 3D printing allows for almost unlimited possibilities for the internal geometry, making it possible to introduce a gradient in the pore radius of the wicking structures to enhance the capillary forces (see section 2.2.4). In addition, and like with the PFS, these channels have no specifications regarding its geometry.

4. Lithium filling

A method to pre-load the targets has to be considered during the design phase as the solid lithium cannot be placed in the reservoir after the component has been printed.

5. Bulk geometry

This is the key subsystem since it has to include all the solutions chosen for the other subsystems and combine them to make them compatible. The internal tungsten structure of the new designs should be capable of efficiently transfer heat from the PFS to the base of the target, should be optimized to minimize thermal stresses caused by the impinging heat load and should have a geometry that enhances the lithium wicking towards the surface. All of this taking into account the restrictions imposed by the 3D printers, such as a minimum thickness of the parts.

6. Interface with Magnum PSI

The targets have to fit the clamping rings and target holder of the Magnum PSI. This limits the external geometry, being a top hat shape with maximum diameters of 30 and 25 mm and a height of the base < 4 mm.

5.2 Comparison criteria

Because of the nature of the porous structure, the subsystems 2-5 have to be all taken into account at the same time during the design phase. As explained in the previous section, the bulk geometry needs to enhance the LL transport to the surface, can have a distributed reservoir and its design should facilitate the filling of the target. For this reason, two groups are established for the comparison criteria:

1. Plasma facing surface
   a. Wetting capacity
      It is necessary for the LL to spread quickly and easily throughout the PFS to guarantee there are no dry spots during plasma exposure.
   b. LL confinement
      Lithium droplets should be avoided and vaporization kept within a reasonable rate to prevent a prompt dry-out of the targets.
   c. Maximum temperature achieved
      Heat extraction towards the base is very important to keep the PFS below the recrystallization temperature of tungsten or avoid excessive thermal expansion.
   d. Induced thermal stress
      The design should lead to low stresses to guarantee the integrity of the targets.

2. Internal structure
   a. Wicking capacity
      Good wicking implies a sufficient LL flow with a high number of channels homogeneously distributed so that enough LL is supplied all over the PFS.
   b. Storage capacity
      Internal geometry must enable the storage of at least 1 g of LL as indicated in the specifications.
   c. Filling complexity
      The design should consider a feasible and effective method to introduce the LL in the target.
   d. Robustness against thermal expansion
      Expansion of the structure should be controlled to prevent wicking channels from getting blocked.
   e. Maximum stress levels
      The design should lead to low stresses to guarantee the integrity of the targets.
   f. Heat transfer to the base
      The final concepts should effectively remove the heat from the PFS and transfer it to the cooled base of the target.

5.3 Subsystem choices

This section includes a short description of the proposed concepts for each subsystem and compares them according to the criteria listed. To reach the best solutions, literature references were checked and back of the envelope calculations performed. In addition, FEM analyses were very useful during the detailed design phase to tune the targets for an optimum performance regarding the temperature and stress criteria. These simulations are shown in section 7.2.

5.3.1 Plasma facing surface

The first aspect considered for the PFS was the method to be used in order to keep the LL attached to the surface and homogeneously spread. For this purpose, three options were contemplated: small blocks, trenches or a mesh.

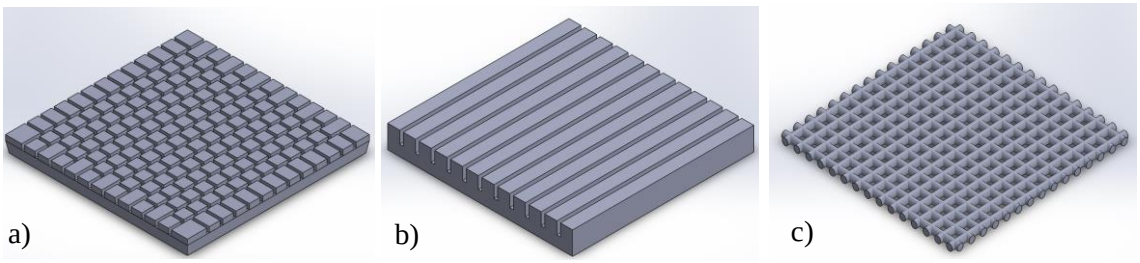

Figure 5-1 *The three solutions considered for the PFS: a) the small blocks, b) a system of trenches or c) a mesh.*

Regarding the wetting capacity, the blocks allow the LL to move in the two directions whereas the trenches only in one direction, making the homogeneous spread more difficult. At first sight, the mesh seems to limit the movement and only allow it below the wires or if the LL wicks on top of the mesh. The possibility to move in the two directions offered by the brushes also guarantees the supply in a certain spot in case one channel gets blocked e.g. due to expansion or melting.

As explained in section 2.2.1, the trenches system gives a better thermal and physical protection to the solid part since more heat is removed via the LL flow thanks to its higher speeds. But this velocity also causes more instabilities and sputtering of the Li, meaning that the attachment is worse and thus more Li has to be loaded inside the targets. The blocks, even though they transfer more heat to the bulk material, provide a better confinement of the surface lithium, thus reducing the loss rate. As for the mesh, experiments performed by P. Rindt [2] with a LL divertor target indicate problems with the LM spreading quickly around the exposed surface. The mesh seemed to suffer from thermal expansion and the contact with the solid part was problematic, leaving an open space through which the LL could not wick well enough.

For the reasons mentioned above, the choice for the Li confinement method was the CPS made of small blocks. These elements lay on top of the solid structure, where the wicking channels of the target lead to. Given the accuracy of the printers and the effect of the parts' size on the relative density, it was decided that these blocks should be 200x200 µm squares with a height of 100 µm. The separation between them was set at 50 µm since it was an optimal separation for the channels at the PFS according to the analytical model proposed by P. Rindt [19].

The next step was to decide what geometry is more adequate to supply the LL to the PFS. The wicks through which the Li flow to the surface are surrounding the brushes of the bulk geometry. This is a good solution to minimize thermal stresses and improve heat transfer in the solid structure [19]. Two main ideas are proposed for the surface geometry:

a) Supply more lithium in the centre
Higher heat loads are expected in the centre of the target due to the Gaussian profile of the plasma beam from Magnum PSI [20]. These designs include circular grids with higher channel density in the centre of the PFS:

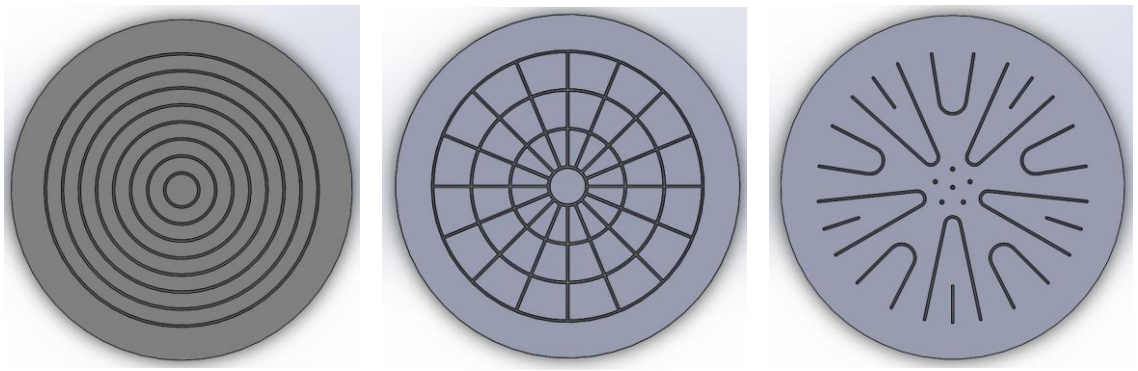

Figure 5-2 *Design proposals for the PFS with bigger channels density in the centre. This allows to supply more LL to the regions of the target with a higher heat load given the Gaussian profile of the plasma beam.*

b) Supply the same amount of lithium all over the surface

This makes the design more flexible and not so oriented to only operate at Magnum PSI and with a particular set of clamping rings. These proposals are based on a regular grid that does not depend on the external dimensions or geometry of the target:

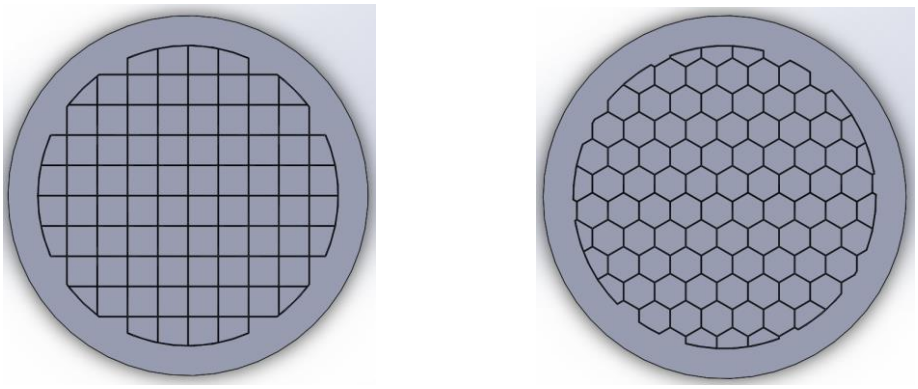

Figure 5-3 *Design proposals for the PFS based on a regular grid. This enables for a homogeneous wetting and a more flexible design in case the concept is to be extrapolated to other machines.*

Regarding the first concepts, big differences exist in the channels density depending on the region of the surface. Larger elements can be found in the external parts of the target, which also imply higher stresses and thermal expansion (proportional to the length). These cannot be made smaller because the central elements have minimum dimensions imposed by the 3D printing technology (at least 1 mm is needed to reach maximum relative density). In addition, if the plasma beam is not perfectly centered during the experiments, some problems can origin due to insufficient lithium supply or poor wetting, causing excessive heating or melting of the tungsten. All these problems can be solved using the regular grids proposed in the second group. Finally, the regular elements (squares or hexagons) can be designed as small as necessary to avoid stress or thermal expansion problems, keeping them above 1 mm to get the maximum relative density.

In conclusion, the best solution considered to act as the plasma facing surface is a system of small blocks placed on top of a solid regular grid made of squares or hexagons.

5.3.2 Lithium storage

One of the big advantages of the 3D printing for this project is that it allows to design the internal geometry with open cavities and channels to connect them. This offers the possibility to get rid of the classic concept of reservoir, where a big empty volume is placed in the centre of the target, and create a distributed reservoir.

With this new concept, by adapting the porosity in every level enough void space can be left inside the targets to store sufficient LL. No cavities should be isolated but they should all be connected by the wicking channels that transport the LL to all the regions of the PFS.

A more open geometry can be modelled in the lowest parts since they should not suffer from the heat loads as much as the top region. With this design, most of the LL is stored at the bottom, while in the top part more tungsten is included. This also helps to extract heat from the PFS as the tungsten has higher thermal conductivity than lithium.

5.3.3 Lithium transport

Since in section 5.3.1 the concept with regular grid was chosen, it makes sense to design the wicking channels with a rectangular cross section so they adapt perfectly to the separation between the top squares or hexagons.

The targets make use of the capillary forces to supply the PFS with enough lithium. Considering the concepts explained in section 2.2.4, the most effective method to enhance this is by increasing the difference between the upper and lower pore radius, keeping in mind that the first must be smaller than the second. In these designs, the pore size refers to the distance between the two parallel faces of the wicking channel. The separation at the top of the channel should be big enough to avoid problems caused by the thermal expansion, and the separation at the bottom should be small enough to guarantee the LL can climb upwards.

To enhance the capillary action, the first idea was to reduce linearly the width of the channels as they go up so that the top pore would always be smaller than the lower pore. This works as long as there is enough LL inside the target, since the separation at the base is much bigger than the separation at the PFS. The problem starts when the target is running out of Li and the lower pore radius comes closer to that of the PFS. For this reason, an elliptic reduction of the channel's width is seen as a better option:

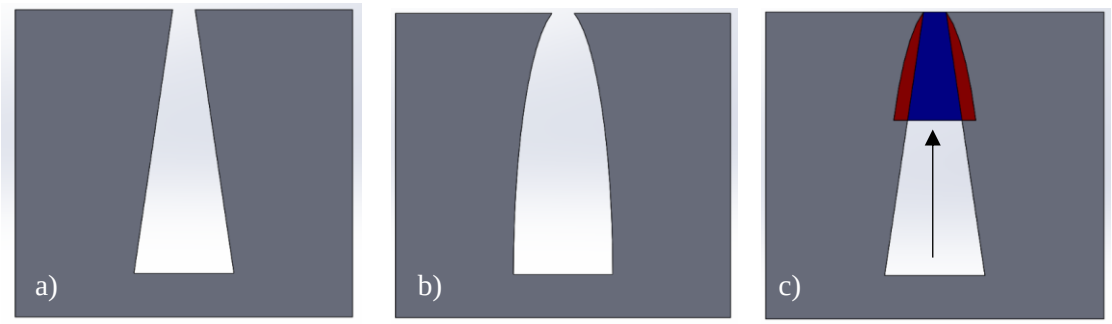

Figure 5-4 *Comparison between linear (a) and elliptic (b) decrease in the channels' width. The same dimensions have been kept at the top and bottom of the wick. The third image (c) reflects the situation where the target is drying out and the upper and lower pore sizes come closer. Notice the difference between the linear channel size (blue) and the additional distance offered by the elliptic design (red). With this second design, the capillary forces can be kept close to the initial values even when the target is almost empty. It must be noted that this is a simplified 2D representation; in the final prototypes the wicks are not straight columns but irregular paths in the 3D space.*

With this parabolic design, not only are the capillary forces kept higher until the target dries out but also allows for more storage capacity. The exact dimensions at the top and bottom of the channels have to be determined considering other factors such as storage volume required, thermal expansion at the PFS or minimum thickness of the printed parts.

5.3.4 Lithium filling

A filling method with LL had to be taken into account during the design process as these targets cannot be opened to place a solid piece of Li inside.

One option considered was to make the wicking channels go all the way from the base of the target till the top so that you can see through them. The problem with this method is that once the prototypes are placed on the target holder at Magnum PSI, there will not be any ventilation hole to compensate for the pressure difference inside the target and, as a result, the LL would not flow upwards. For these reason, this proposal was dismissed.

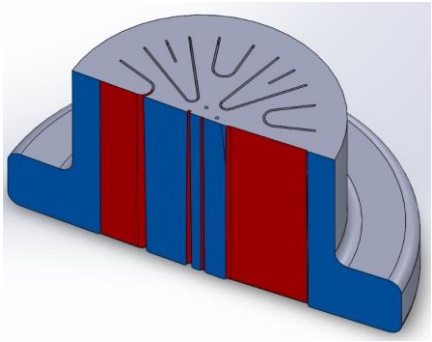

Figure 5-5 *Example of the first proposal to fill the targets. The idea was to soak the prototypes in a LL bath and let it wick by capillarity to the PFS. The blue and grey regions in the image represent the solid tungsten parts, and the red parts are the inside of the wicking channels of this cross section.*

The second option considered was to use the hole needed for the printing process (see section 4.3) to insert the LL in the targets. This hole should be placed as far as possible from the PFS since it is also used as ventilation channel, so it should contain as little Li as possible during the experiments at Magnum PSI. In addition, the hole should be much bigger than the separation of the wicking channels at the PFS, otherwise the capillary forces would not be sufficient to pull the LL. According to P. Rindt, for a 50 µm separation at the PFS, the distance of the wicks or the hole at the bottom should be of the order of mm to get the maximum flow.

Once inside the samples, the LL should be able to move in all directions to guarantee the best filling possible. This implies that from the bottom of the targets, the Li should "see" all the internal structure including external walls and PFS. An injection tool could also be designed to make the filling easier.

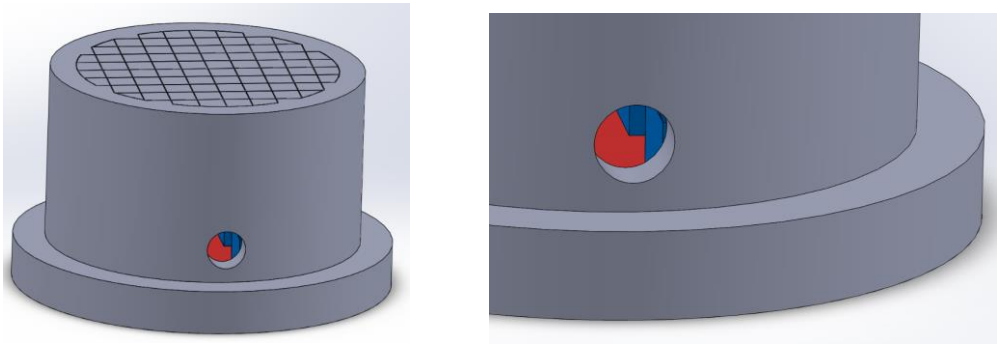

Figure 5-6 *Example of the second proposal to fill the targets. The idea is to use the hole needed to extract the dust after the printing to insert the LL inside the targets. The internal geometry should enable the lithium to move in every direction. In the images, the internal structure is in colour blue and the colour red is the inner part of the base.*

5.3.5 Bulk geometry

This is the key subsystem of the targets since it has to include all the solutions chosen for the other subsystems and combine them in a way there are all compatible.

The initial idea was to use a design software specialised in modelling porous structures, such as *Netfabb* [42] or *Ntopology* [43]. With these programs it is possible to create a 3D mesh and easily modify variables such as the thickness of the printed parts or the pore dimensions and locations.

The problem is that with the student version or the free trial it is not possible to design complex 3D structures, so this option had to be dismissed.

At this point, two main concepts were developed to create the final bulk geometry:

a) V-shape design

Named like this due to the inverted V look, this model originated from the idea of recreating the 2D meshes done by FEM software when it uses triangular elements.

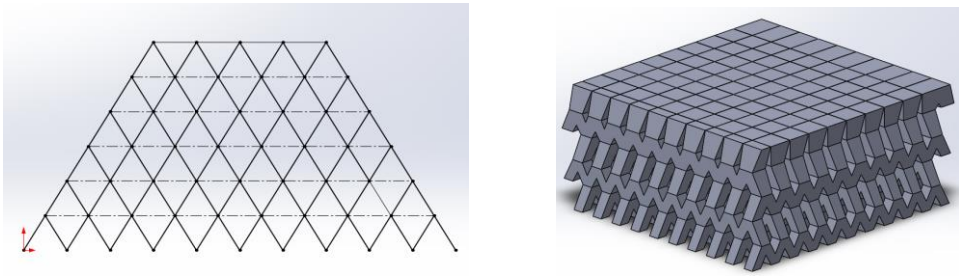

Figure 5-7 *Sketch of the V-shape original idea and internal structure of the design. It is formed by consecutive layers of rows that change direction in every step. Thickness of the Vs increases as they get closer to the PFS in order to gradually decrease the pore radius of the wicking channels. The top face of the target consists in a regular grid made of squares.*

The lowest layer is a set of rows with connected Vs in one direction. The next layer is another set of rows with connected Vs but at 90º. And so on until reaching the PFS. In every layer the thickness of the Vs increases. This causes the separation between two parallel rows to decrease as they get closer to the top. This distance reduction is modelled so that it follows an elliptic profile to optimize the lithium transport as decided in section 5.3.3. In the top layer, additional cuts to the geometry are performed in order to obtain the regular grid made of squares.

With this structure, the distributed reservoir is feasible since there are many cavities and they are all connected. In addition, higher storage capacity is left at the bottom of the target while the top region contains more printed tungsten. Finally, the filling hole should be placed between two of the bottom rows to make the insertion of LL easier.

Given the small dimensions of these Vs, the design is robust against thermal expansion. In addition, the numerous connections between two consecutive layers make the heat transfer towards the bottom of the target very efficient, homogenizing and lowering the maximum temperature and the stresses caused by the thermal loads.

b) Tree design

As the name indicated, the second concept is based on the shape of trees. The branching geometry, going from coarser to finer elements, gives the structure good mobility and higher solid content at the top.

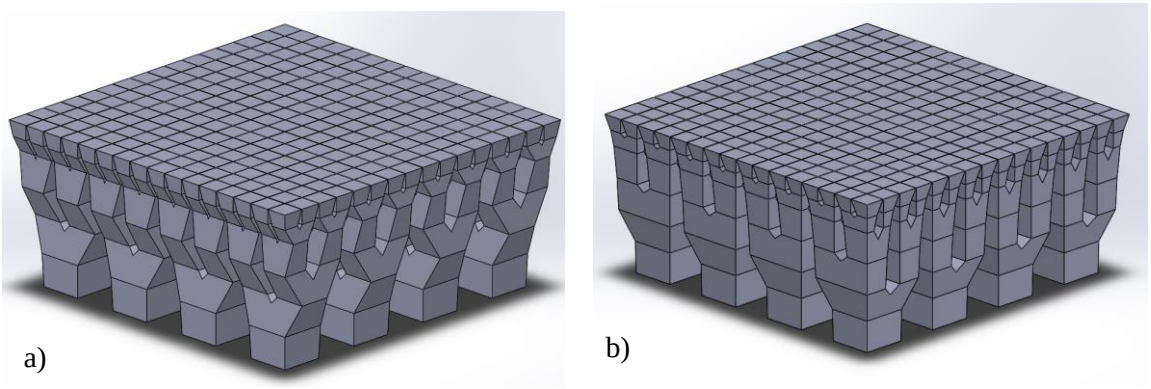

Figure 5-8 *Internal structure of the two candidates for the tree design: a) the square version and b) the rectangular version. In both cases, the structure starts with a trunk that is divided into two branches several times until reaching the PFS. In addition, the trees are not the same in the X and Y directions due to the branching system. The difference between the two versions lies on the section of the branches. In b), the rectangular shape allows the wicking channels to narrow more regularly as they get close to the PFS.*

The idea consists in a main trunk that starts at the base of the target. This first element is divided into two, and each of these two parts divide again into two more. And so on until reaching the PFS. As the branches get closer to the top, the distance between them diminishes as decided in section 5.3.3.

Like in the previous concept, this structure also enables the distributed reservoir since there are many cavities that are all connected, and big open spaces have been left at the bottom to store enough lithium to satisfy the requirements. With the big separation between the bottom trunks, the filling hole could easily be placed between two "trees" to insert the LL without any problem.

Regarding the thermal response, the tungsten can expand without problems given the low connectivity of the structure in the plane perpendicular to the main thermal gradient. Furthermore, the geometry with the trunk and brunches provides the structure with great movement capacity, translating into minimum stress levels. The only drawback would be in case of dry-out: trees would be isolated as no heat could be transferred between them through the LL. This would generate different temperatures in each tree depending on the heat load received by the squares at the top.

The difference between the square tree and the rectangular tree lies on the cross section of the branches. The square shows that in every step, while the width of the wicking channel was reduced in one direction, it increased in the other. This was because as the number of branches increased, their section became smaller. In order to reduce the separation between branches in the two directions at every step, a rectangular cross section had to be introduced. This second version allowed for a more regular narrowing of the wicking channels, keeping the upper distance always smaller than the lower one.

Both the V-shape and the rectangular tree geometries are able to satisfy the requirements of the targets and can integrate the selected solutions for each subsystem. For this reason, and since the performance of the target is very much dependant on its internal geometry, it was decided to elaborate a complete design with each structure and compare their response during the experiments at Magnum PSI.

5.4 Definitive designs

At the end, three different designs are proposed: two porous concepts that use a distributed reservoir (V-shape and tree designs) and a more conventional concept with a big central reservoir (adaptation from P. Rindt design). The concepts chosen for each subsystem are listed here for each design:

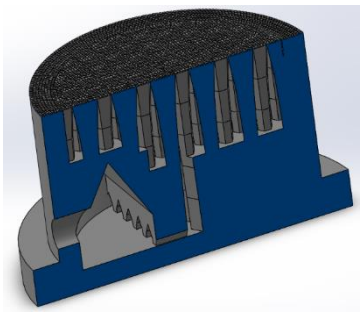

Figure 5-9 *Cross section of the conventional design. Notice the small gates that connect the reservoir with the main wick.*

Conventional design

- PFS: Hexagonal brushes with mini blocks on the top surface.
- Li storage: main central reservoir.
- Li transport: wicks in hexagonal grid pattern with elliptical varying width.
- Li filling: insertion through the ventilation hole.
- Bulk geometry: similar to the original design.

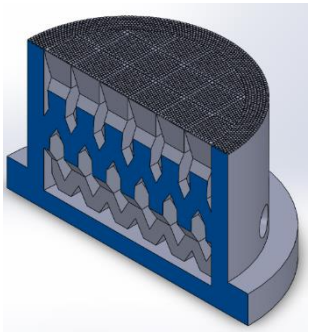

Figure 5-10 *Cross section of the V-shape design.*

V-shape design

- PFS: Bigger square brushes with mini blocks on the top surface.
- Li storage: distributed reservoir.
- Li transport: wicks with elliptical varying width leading to a square grid at the PFS.
- Li filling: insertion through the ventilation hole.
- Bulk geometry: gradient porous structure with five layers of rows of connected Vs.

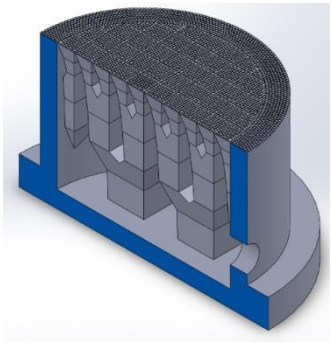

Figure 5-11 *Cross section of the tree design.*

Tree shape design

- PFS: Smaller square brushes with mini blocks on the top surface.
- Li storage: distributed reservoir.
- Li transport: wicks with elliptical varying width leading to a square grid at the PFS.
- Li filling: insertion through the ventilation hole.
- Bulk geometry: gradient porous structure with five layers, following the branching structure of a tree.

6 DETAILED DESIGN

As explained in the previous chapter, three different designs are proposed: the V-shape, the Tree and the Conventional model. The three concepts include all the solutions chosen for each subsystem (see section 5.3). The main difference between the three proposals lies on the internal structure of the targets. For the conventional model, another different trait is the existence of a central reservoir whereas the two porous designs integrate the concept of distributed reservoir.

6.1 External geometry

The three proposals have the same external geometry to be compatible with Magnum PSI:

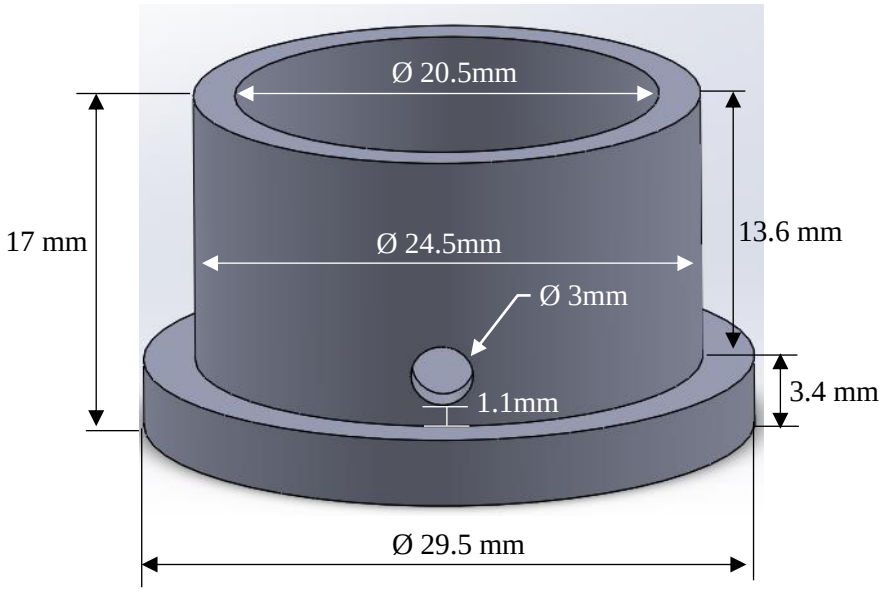

Figure 6-1 *External dimensions shared by the three proposed designs. These are imposed by the clamping rings and a safety margin left to guarantee a correct fit and allow space for thermal expansion.*

The clamping rings used during the experiments have diameters of 30 and 25 mm and a height of 4 mm. To guarantee that the printed targets fitted inside the rings and to leave some space for thermal expansion, the external dimensions of the designs are slightly reduced. With this, a safety margin of 0.25 mm was left in each radial direction and 0.6 mm were left for the height of the base. This last number was bigger since a grafoil layer had to be placed in the interface with the clamping ring to improve the contact between the two metals. To avoid any Li leakages through the base or the sides of the targets, a 2 mm thick layer of tungsten was included in the design.

The height of the targets, 17 mm, can be divided into the 2 mm from the base layer to prevent leakages and the 15 mm for the internal structure. Since the geometries described in section 5.3.5 consist in different layers, it was decided to design the structures with 5 layers of 3 mm each. With shorter targets the amount of stored Li would be reduced, and with taller targets the cooling at the PFS would be less efficient (in Magnum-PSI the target holder is cooled).

An injection tool with a nozzle was designed to improve the filling. In order to adequately couple the tool with the target, the hole was made with a diameter of 3 mm and separated 1.1 mm from the base. It is important that this hole is much bigger than the separation of the channels at the PFS to guarantee that the capillary action is effective.

6.2 Plasma facing surface

Another common aspect in the three designs is the type of PFS. In the porous models, it consists of square brushes separated 60 µm, and in the conventional model the brushes are hexagonal but keep the same distance. For the conventional and tree designs, the polygons are 2 mm wide, while for the V-shape the side of the square had to be made bigger (3.4 mm) due to the minimum thickness of the parts in the bottom layer.

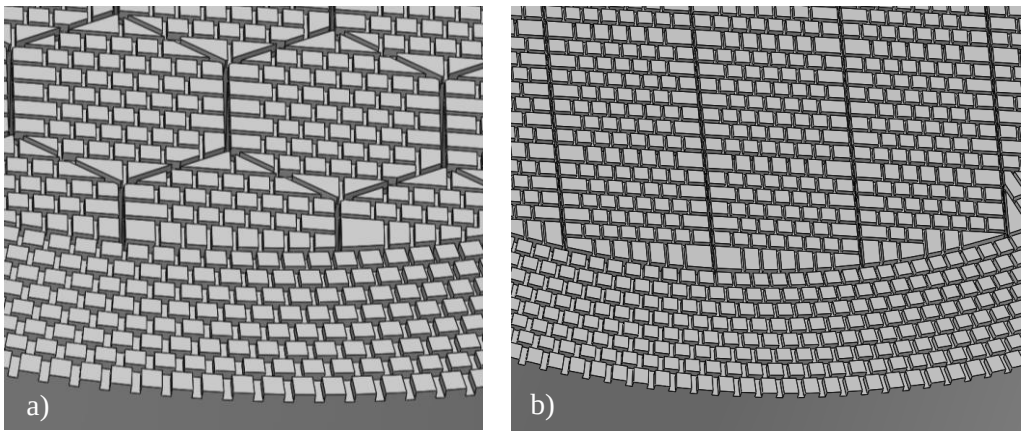

Figure 6-2 *Detail of the PFS of the conventional design (a) and the tree design (b). In the two images the brushes can be seen as well as the wicking channels and the small blocks used as texture of the top faces.*

The texturing in the three cases is the same: small blocks with a square base of 200x200 µm and a height of 100 µm, separated 50 µm from each other. Due to the low relative density achievable at such low dimensions, the blocks were not designed smaller. The blocks at the edges of the brushes are slightly bigger in order to cover all the area and avoid too tiny elements or wider separations.

6.3 Bulk geometry and storage capacity

The internal structure is what changes the most between the three designs. For this reason, this geometry will be analysed independently for each concept.

6.3.1 Conventional design

This version adapts the concept proposed by P. Rindt [19] to fit in the same clamping rings used by the porous targets and to be manufactured using 3D printing technology.

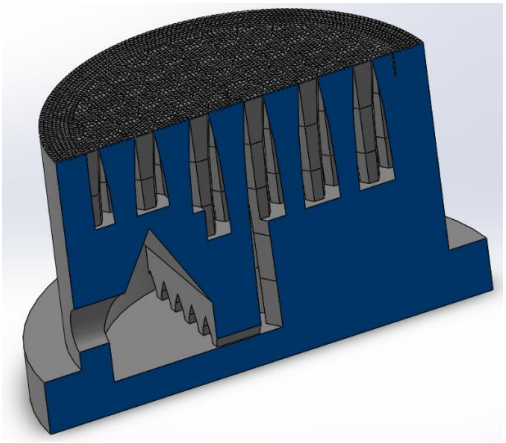

Figure 6-3 *Cross section of the conventional design. From this perspective it is possible to see the gates that drive the LL from the reservoir to the main wick.*

In this version, the reservoir does not have horizontal ceiling as this is not printable (see section 4.3). For this reason, a 60º roof was designed, with a maximum height of 9 mm and width of 7 mm to have enough storage capacity. The LL is loaded in the reservoir, and from this chamber it flows through the small gates showed in **Figure 6-3** to the main wick. Once here, Li climbs towards the PFS and expands to the rest of the channels in the steps at 8, 6 and 5 mm from the PFS seen in **Figure 6-4**. These steps are necessary to prevent the channels from intersecting with the reservoir. It is preferable to keep this big volume closed on the top to guarantee that no LL flows back from the wicking channels to the chamber.

On the other side of the target, it can be noted that the channels are only 8 mm deep even though they could go down to the base. This was designed this way to keep the new version more similar to the original (see **Figure 2-2**).

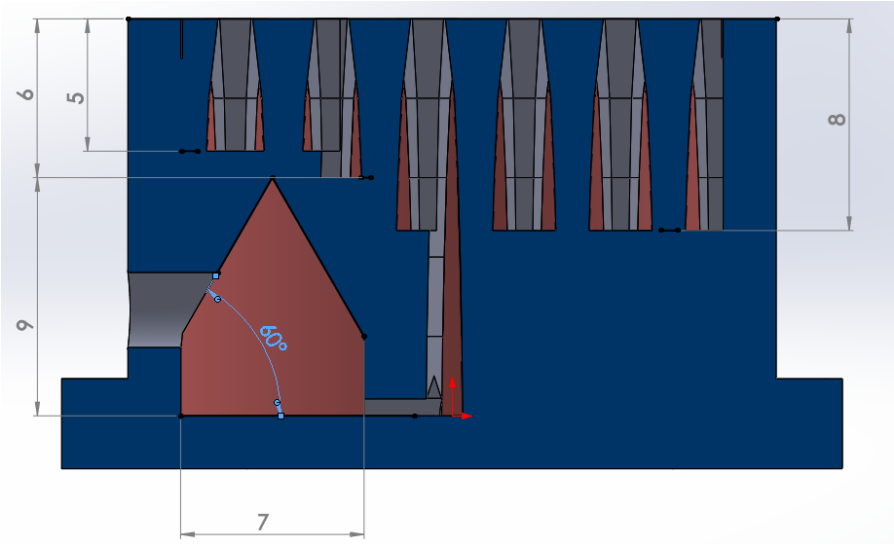

Figure 6-4 *Cross section of the conventional design. In red the inner part of the external wall. Some of the most relevant dimensions for the modelling are indicated. Notice the elliptic profile of the pillars, narrowing the wicking channels as they get closer to the PFS.*

With the dimensions set, and according to the CAD file, this design has capacity to store 1.03 g of lithium. This number is obtained from dividing the empty volume inside the target (the CAD file provides the volume of solid) by the LL density. Later on, measurements of the pre-loaded printed target showed that it actually stored more Li than expected (see section 8.1). One reason might be that these 1.03g are calculated considering that no LL is placed on the outside of the target and that no Li diffuses inside the printed tungsten (6% porosity).

6.3.2 V-shape design

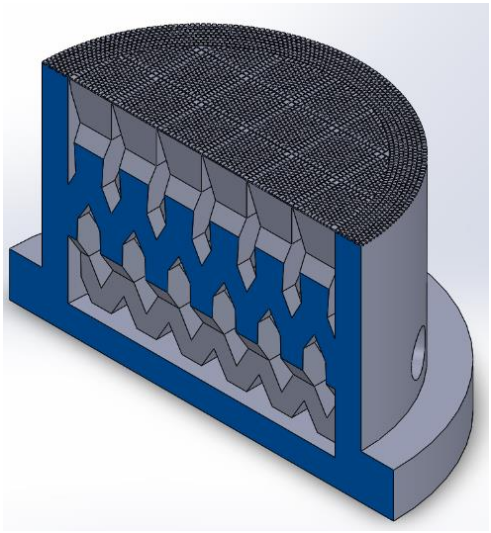

Figure 6-5 *Cross section of the V-shape design. This perspective shows the square brushes on the PFS and how the thickness of the Vs increases as they get closer to the top.*

In this first porous design, the thickness of the lowest layer was set at 1.5 mm to guarantee that the maximum relative density could be reached. This gives the structure better thermal conductivity and higher strength according to the results of the material tests (section 3.2). The thickness of the next layers (see **Figure 6-6**), was set to make the wicking channels adjust to the elliptic profile described in **Figure 6-9**.

To allow enough storage capacity, the lowest rows are separated 1.96 mm. This distance decreases until reaching the 60 µm at the PFS.

The filling hole is placed in a position that allows the LL to enter the target trough one of the big hexagonal cavities that can be seen in **Figure 6-6**:

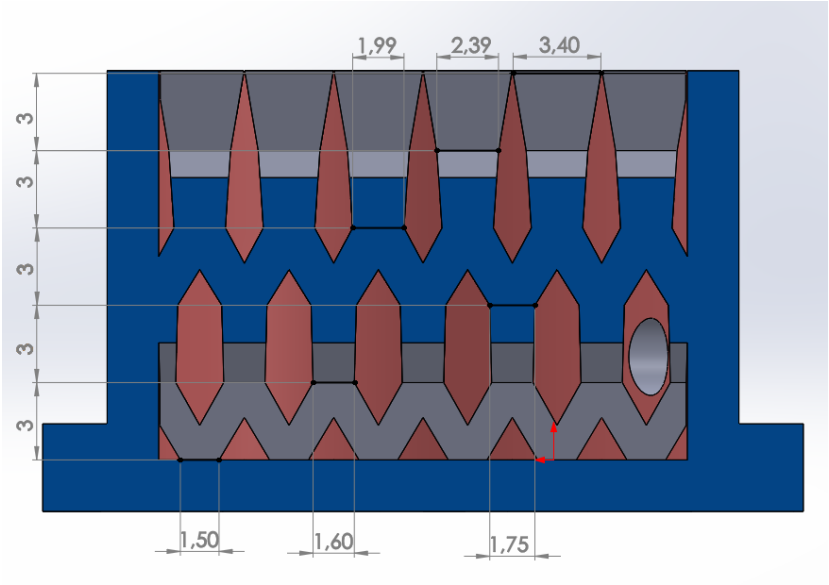

Figure 6-6 *Cross section of the V-shape design. In red the inner part of the external wall. The thickness of the Vs in every layer is indicated. Notice the five layers of 3 mm each and the increase of the Vs thickness.*

With the dimensions set, and according to the CAD file, this design has capacity to store 1.35 g of lithium. This number is obtained using the same procedure as for the conventional model. Like in the previous case, measurements done on the pre-loaded printed target showed that it also stored more Li than expected (see section 8.1).

6.3.3 Tree design

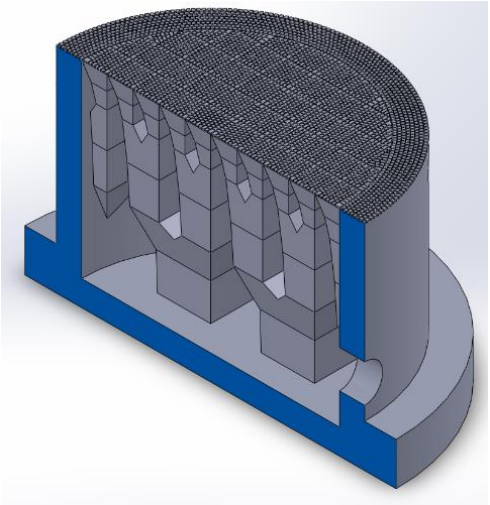

Figure 6-7 *Cross section of the tree design. Notice the different size of the brushes when compared to those of the V-shape in* ***Figure 6-6****. The image also shows how some branches appear from the wall of the target and not from a trunk connected to the base.*

As explained in section 5.3.5, the chosen tree structure is the one with rectangular branches as it offers a better control over the dimensions of the channels.

In this design the top brush is 2 mm wide with a separation of 60 µm. The rest of the branches are adapted to leave the wicking channels with an elliptic profile.

In this concept, the separation between the bottom trunks is increased from the indicated by the parabolic shape to increase the storage capacity. For this reason, there is this big gradient in the second layer.

The position of the filling hole, between two main trunks, allows the LL to enter the target without any difficulty and spread around the interior.

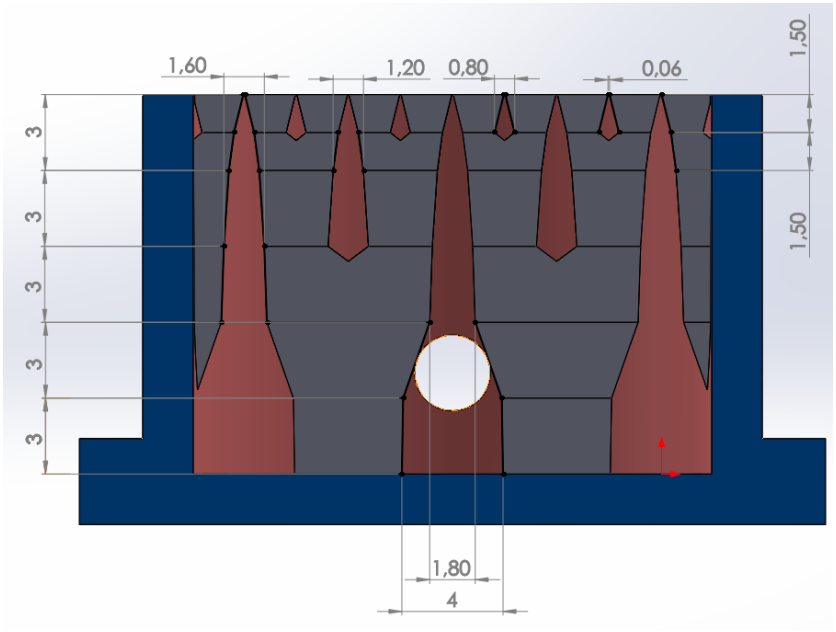

Figure 6-8 *Cross section of the tree design. In red the inner part of the external wall. The width of the channels in every layer is indicated. Notice the branches growing from the side wall and the parabolic shape of the wicks as well as the big gradient in the second layer mentioned above.*

With the dimensions set, and according to the CAD file, this design has capacity to store 1.63 g of lithium. This number is obtained using the same procedure as for the other models. Like in the previous cases, measurements done on the pre-loaded printed target showed that it also stored more Li than expected (see section 8.1).

6.4 Lithium transport

As explained in section 5.3.3, the chosen solution for the wicking channels is to reduce its width following an elliptic profile. The separation at the top is always 60 µm, but at the bottom the separation depends on each structure. The following plots show the evolution of the wicking channels (linear approximation) and the macroscopic porosity of each target as they get closer to the PFS. To calculate the porosity, the empty surface was measured with the CAD software and it was then divided by the total area of every cross section. These measurements were done every 1 mm, and are indicated with a cross in the plots.

As described in section 6.1, the internal structures are divided into 5 layers of 3 mm each. A linear variation is used in every layer to approximate the elliptic profile of the channels, where the gradient $\Delta width/\Delta height$ increases in every layer (the separation of the channel decreases, but the width variation increases in every step).

The separation at the bottom of the wicking channels is influenced by the storage capacity of each structure. For this reason, the distance at the bottom of the conventional target is lower since the reservoir already stored 33% of the necessary Li. For the tree design, this distance is bigger because, according to FEM simulations (see section 7.2), this model was expected to reach higher temperatures. As a result, more Li could be lost with the same exposure conditions, so a bigger storage capacity was designed.

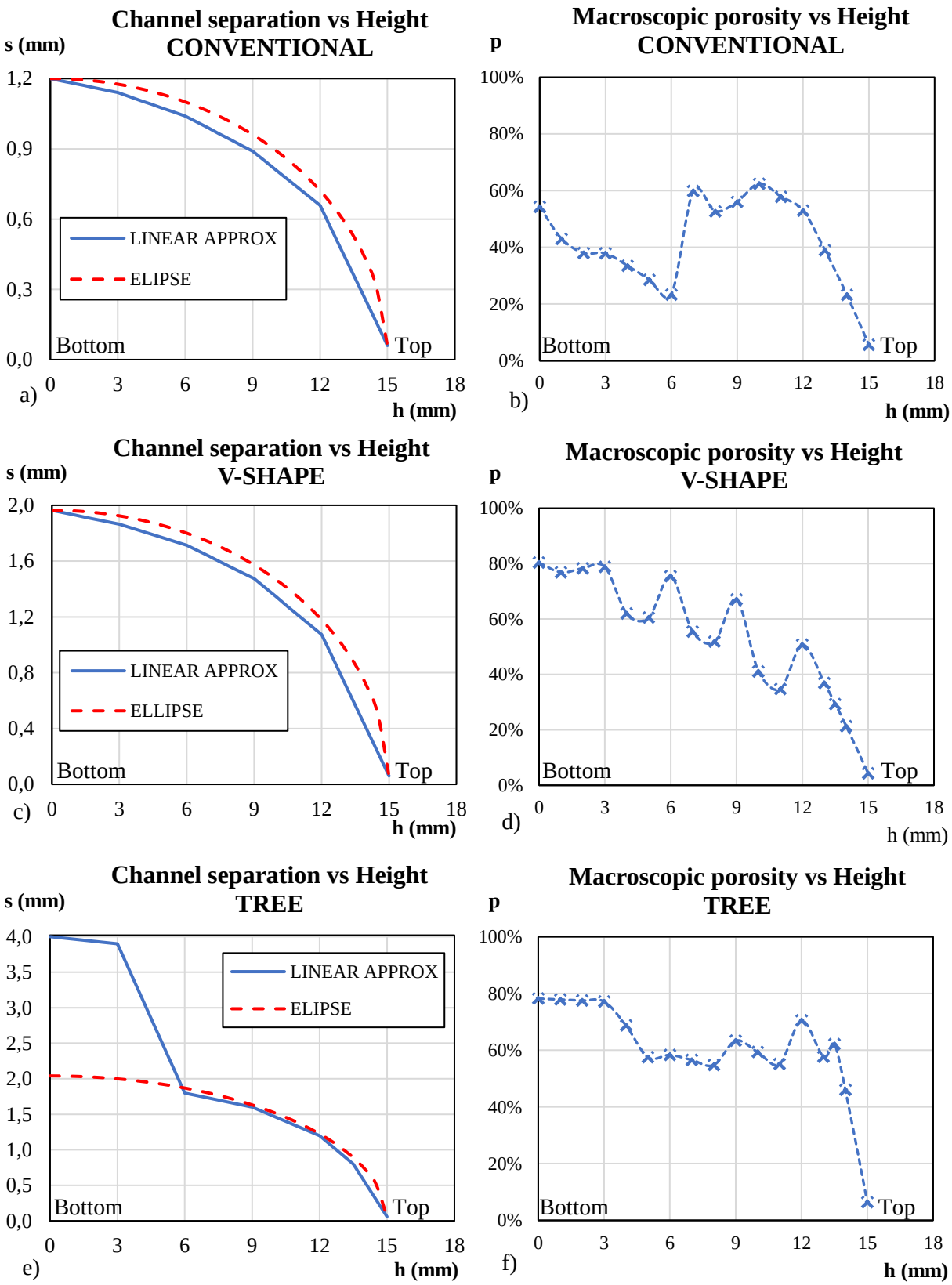

Figure 6-9 *Evolution of the channel separation and macroscopic porosity compared to the altitude of the three internal structures. Height h=0 represents the base of the target, and h=15 mm the PFS. Notice that in the lower layers the wicking channels are more vertical with smaller gradients, and in the top layers the separation decreases faster. In the tree design (e, f), it was necessary to increase the distance at the bottom to be able to store more lithium. The available storage volume is proportional to the area below the curve of the porosity plots. Taking this into account, it can be seen how the tree structure has more Li storage capacity. Notice as well that in the conventional design the reservoir contains around 30% of the total Li (b). This open volume starts at height 0 and finishes at h=9 mm (see* ***Figure 6-5****).*

7 ANALYSIS OF THE DESIGNS

The analysis of the prototypes includes a first part where geometrical decisions are justified and a second part with back of the envelope calculations and FEM simulations.

7.1 Estimations of the maximum LL supply rate

To make sure that enough LL could wick to the surface and compensate for the estimated loss rate, the achievable supply rate for each target was calculated. As a reminder, the expression used to determine this flow is obtained from Darcy's law:

$$\dot{Q} = -\frac{k \cdot A \cdot \Delta P}{\mu \cdot L}$$

An analytical model was made by P. Rindt to calculate the supply rate in his model [19]. The resulting expression is the following:

$$\dot{Q} = \frac{2 \cdot \gamma \cdot cos\alpha / r_u - 2 \cdot \gamma \cdot cos\alpha / r_l}{R_{tot} + \sigma \cdot B^2 \cdot \sum_{i=1}^{n} L_i / A_i} \; ; \; where \; R_{tot} = \sum_{i=1}^{n} R_i = \sum_{i=1}^{n} \frac{\mu \cdot L_i}{k_i \cdot A_i}$$

All the terms are explained in section 2.2.3. This calculation was done with a numerical approximation, dividing the height of the internal structures into 1500 intervals. Referring to the expression above, n = 1500 and L_i = 10 µm for every interval. Additional intervals were added to include the wicking of LL until the center of the textured brushes.

To determine the LL supply rate, some assumptions were made:

a) For such short intervals (10 µm), the wicking channels can be considered as two parallel plates. This allows to use the expression derived from the Poiseuille flow for parallel plates: $k=r^2/3$, being k the permeability and $2 \cdot r$ the separation of the channel.

b) A constant magnetic field (B) of 1T was assumed.

c) To determine the wicking cross section, A_i, the design was cut every 1 mm and the solid surface was measured with the help of the CAD software. With this number and knowing the external geometry of the target, the empty surface at each cross section was obtained. The last part was to estimate the empty cross section for every L_i. This was done by doing a parabolic regression for every 4 measurements (e.g. at 3-4-5-6 mm). Notice that the gradient of the wicking channels changed every 3 mm as explained in the detailed design. For the conventional design, the empty surface that corresponded to the reservoir and the small gates used to lead the LL to the main wick was not considered as wicking channels.

d) The radius r_u is half the width of the separation between the surface blocks (25 µm in the CAD file, 50 µm in the real printed targets) and r_l is half the width of the channel at the bottom (e.g. 2 mm in the tree design).

The values of the properties used can be found in the Appendix C.

With these assumptions, the achievable supply rates for each target are:

Table 7-1 *Achievable supply rates of LL for each target. The designed targets have a separation between the surface blocks of 50 µm. After the printing, surface analysis with an electron microscope showed that this separation in the prototypes is around 100 µm (see* ***Figure 9-18****). Notice that the pore radius (r) is considered as half of this distance.*

[l/s·m^2]	Dimensions from CAD file (r_u = 25 µm)	Real Texture dimensions (r_l = 50 µm)
Conventional design	14.7	9.0
V-shape design	9.7	10.7
Tree design	24.2	23.7

Even though these are rough estimations, the numbers obtained are 4-5 orders of magnitude higher than the loss rate calculated in 2.2.3, which was $2.42 \cdot 10^{-4}$ l/s·m^2. This means that the targets should have enough wicking potential to prevent the PFS from drying while there is still LL inside the prototypes. The values of the supply rates are discussed in section 11.2.

One of the reasons why the tree design has a much higher wicking flow is that the channel separation at the bottom is 4 mm while for the others is 1.2 and 1.96 mm. In addition, the size and number of brushes at the PFS also plays an important role. When the size and number of brushes of the V-shape design are introduced in the flow model for the tree concept, the supply rates are 10.1 and 11.9 l/s·m^2 instead of 24.2 and 23.7 l/s·m^2. This only by changing the squares of the PFS from 2 x 2 mm^2 to 3.4 x 3.4 mm^2 and keeping the same texture.

7.2 FEM simulations

To optimize the designs regarding stress distribution and verify that they could survive the fusion-relevant conditions from Magnum PSI, simulations using FEM were done. To study the worst-case scenario, these analyses were performed considering the targets were dry, so no LL was included in the designs. This implied that heat transfer in the wicking channels was negligible and thus no energy transmission would exist between brushes.

Given the computational limitations, the top texture was eliminated during the simulations. In the same line, the mesh used had quadratic elements of 0.7 mm and a tolerance of 0.035 mm. Tests were done with finer meshes but the difference in the results was negligible for the purpose of these simulations while the necessary time to obtain the results increased exponentially. The size of the mesh was considered as adequate since the most critical parts contained numerous elements, as can be seen in **Figure 7-1**.

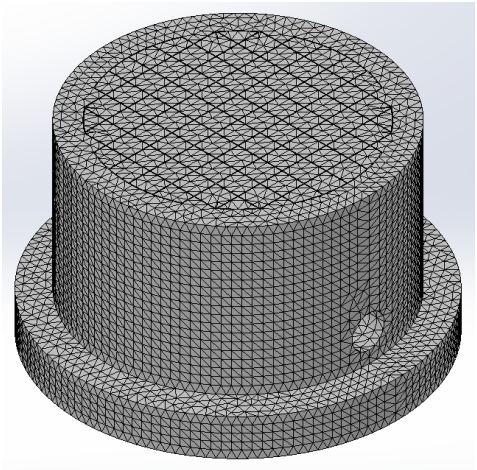

Figure 7-1 *Mesh used for the analysis of the tree design. The elements of the meshes used for the conventional and V-shape models had the same dimensions.*

For the three designs, the same boundary conditions were set:

a) Thermal analysis
   1. Initial temperature of 100ºC.
   2. Constant temperature at the base of 70ºC. The target holder at Magnum PSI is cooled at 20ºC, and according to experience with this machine the grafoil used reduces the cooling at the base by 40-50 ºC/layer.
   3. Heat flux of 15 MW/m^2 with a Gaussian profile (FWHM = 14.7 mm) at the PFS.

b) Structural analysis
   1. Temperature distribution obtained from the previous analysis (thermal load).
   2. Three points at the base with restricted movement as indicated in this diagram:

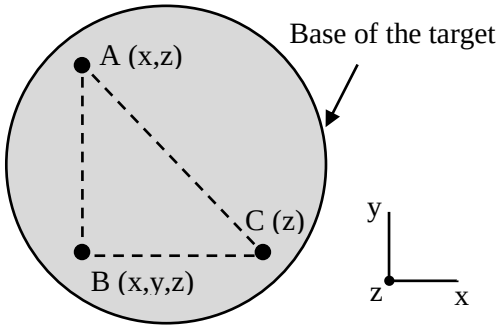

Figure 7-2 *One of the boundary conditions in the structural analysis was to restrict the movement of three points of the targets' base. For each point A-C, the terms in brackets represent the directions with limited movement. The whole base was not fixed because there would be some space available for expansion between the prototype and the clamping ring.*

All the simulations run were time dependent with 10s exposure to the heat load. In the thermal analyses, the results were compared with the melting and recrystallization temperatures of tungsten (3422ºC and 1600ºC for 1h respectively). For the structural analyses, the von Mises criterion was used, with the maximum strength being set at 225 MPa (see section 11.1). The tungsten properties used for the FEM simulations can be found in Appendix D.

7.2.1 Conventional design

The thermal analysis showed that after 10 seconds under a peak heat flux of 15 MW/m^2 on the dry target, the temperature could reach values around 3000ºC. This means that the target would survive without melting but recrystallization could start in the central brushes as can be seen in **Figure 7-3**. Since the exposure is so short, this process would not have a big impact on the tungsten. It must be kept in mind that these prototypes were designed to operate with LL on the PFS and inside them. The LM was expected to protect the surface and improve the heat transfer both in the radial and the axial directions, so the temperature of the wetted targets during the experiments at Magnum should be much lower.

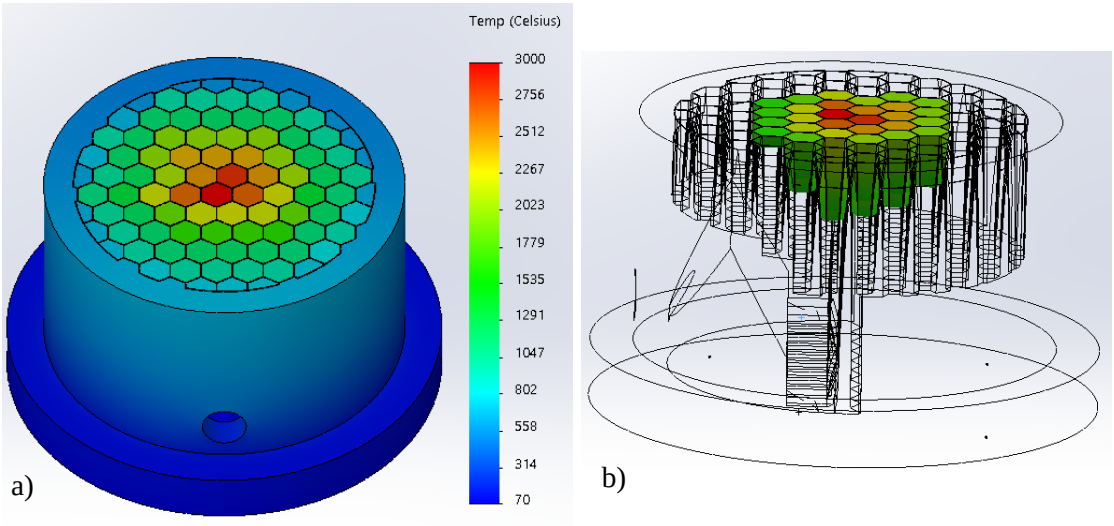

Figure 7-3 *a) Temperature distribution of the conventional design without LL after 10s exposure under peak heat flux of 15 MW/m^2. Notice the temperature difference between two consecutive brushes: this is due to the lack of LL between them, so no heat transfer exists in the horizontal plane. In b), regions with a temperature above 1600ºC are shown. The hottest brushes form a circle around the centre due to the Gaussian profile of the heat flux.*

The structural analysis show that the target would not suffer from big stresses, which is one of the main reasons for using AM. The peak von Mises stress reached is 48.4 MPa (21% of the maximum strength). **Figure 7-4** shows that the region with highest stress is a sharp corner where a brush meets the external wall, meaning that this stress peak is caused by the design restrictions of Magnum-PSI. This channel can be seen in the top left side of **Figure 6-4**. If only the internal structure is considered, the maximum Von Mises stress is around 15 MPa and originates at the edge where the main wick leads for the first time to the secondary channels.

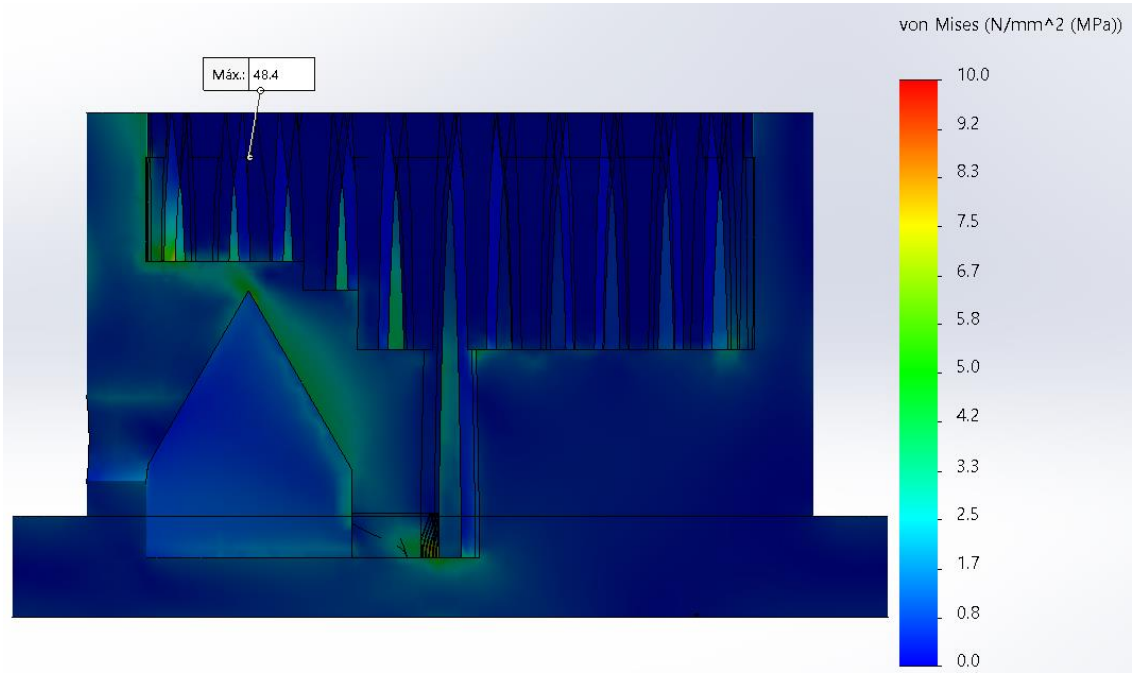

Figure 7-4 *Von Mises stress distribution of the cross section of the conventional design. The plot has been rescaled to appreciate the areas which suffer more, although there are almost no traces of stresses above 15 MPa. The maximum von Mises stress (48.4 MPa) and its location is also indicated in the image. In the internal structure, the peak stress is around 15 MPa.*

7.2.2 V-shape design

After 10 s under a peak heat flux of 15 MW/m^2 on the dry target, the V-shape design reached a maximum temperature of 2624ºC. The temperature is still high but lower than the conventional model. The reason is because in this case all the structure is connected, so even if there is no Li, heat can be transferred to all directions through the consecutive layers. Like in the previous case, the central brushes reach recrystallization conditions, but given the short exposure time, effects on the material would be limited.

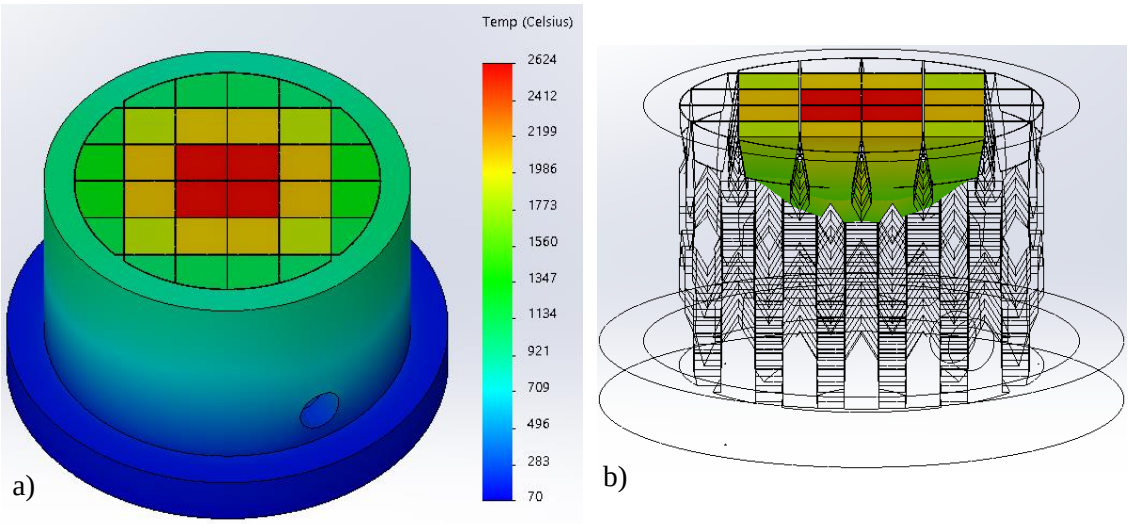

Figure 7-5 *a) Temperature distribution of the V-shape design without LL after 10s exposure under peak heat flux of 15 MW/m^2. In b), regions with a temperature above 1600ºC are shown. The temperature distribution on the PFS and in the vertical direction form a spherical shape given the Gaussian profile of the heat flux.*

The structural analysis shows again very low stresses, being the peak von Mises stress 66.8 MPa (29% of the maximum strength) in a sharp corner where a channel is in contact with the external wall. **Figure 7-6** shows that the third and fourth layer are the regions inside the target with higher stresses. The maximum Von Mises stress in the internal structure is around 18 MPa, and originates in the third layer.

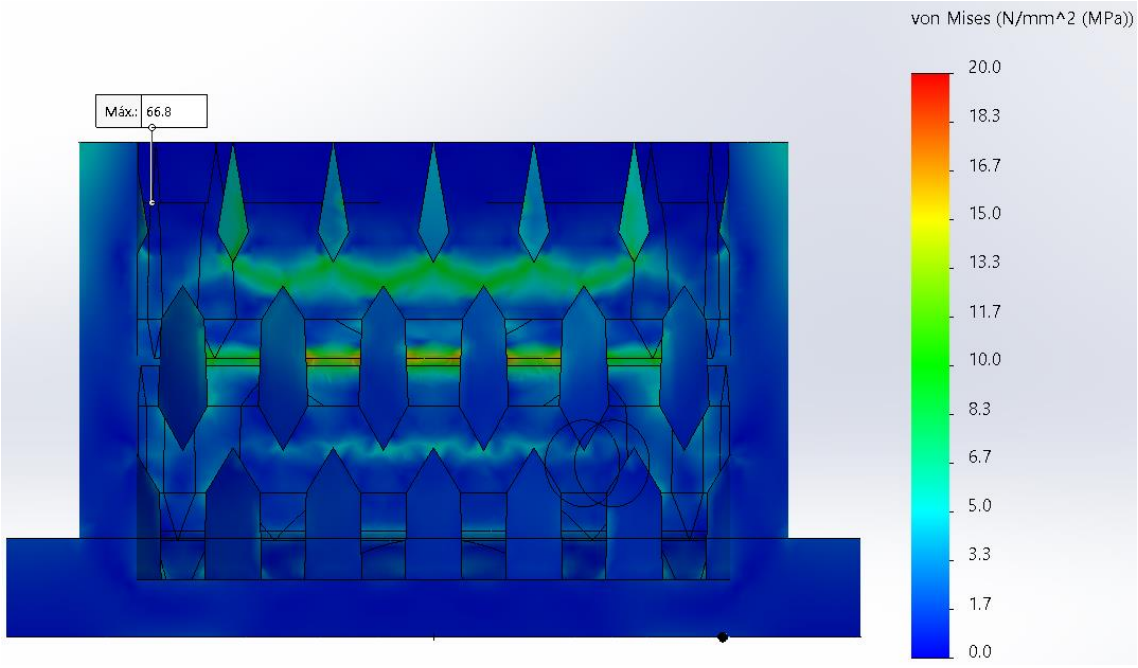

Figure 7-6 *Von Mises stress distribution of the cross section of the V-shape design. The plot has been rescaled to distinguish the areas under higher loads, which are the third and fourth layer. The maximum von Mises stress (66.8 MPa) and its location is also indicated in the image. In the internal structure, the peak stress is around 18 MPa.*

7.2.3 Tree design

In this model the highest temperature among the three proposals is reached. According to the thermal simulation, almost 3400ºC could be reached if the target is exposed without LL at such heat flux. Even though this temperature is below the melting point, there would most probably be damage on the PFS, especially in the texture. Like it was mentioned with the conventional design, these prototypes have been created to operate with the LL, so the top surface should not be so exposed to the heat load and the thermal conductivity inside the target would be much better with the presence of the Li. It is important to mention that the tree design is the one with the highest wicking capacity (see section 7.1), so it is more difficult to get a dry spot on the PFS.

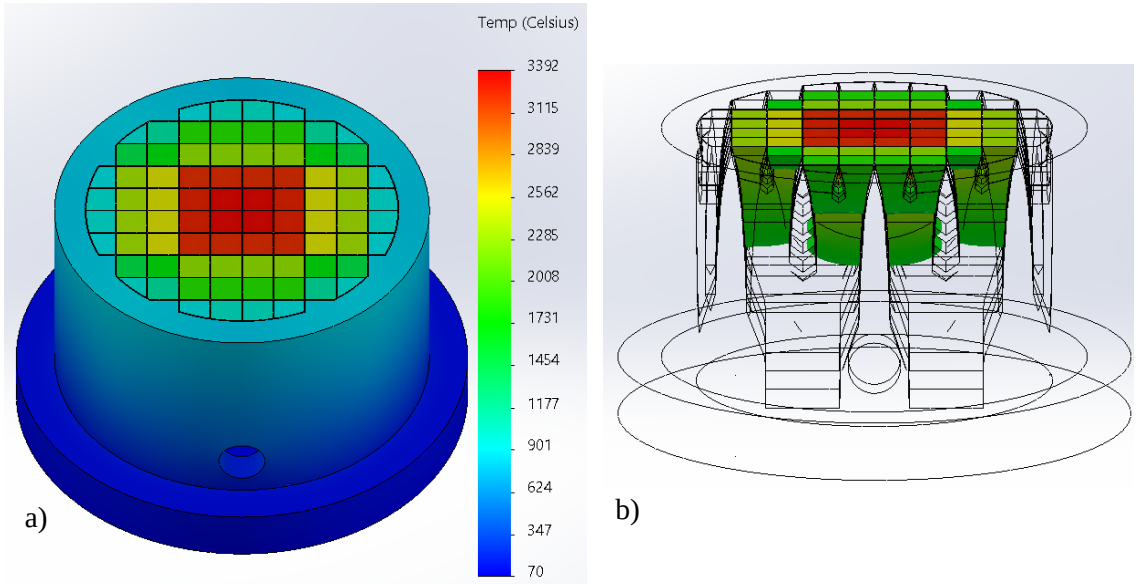

Figure 7-7 *a) Temperature distribution of the tree design without LL after 10s exposure under peak heat flux of 15 MW/m^2. In b), regions with a temperature above 1600ºC are shown. For this model, the recrystallization regime is reached as well in some parts of the third layer from the top, which means more than 6 mm deep.*

While this model has the worse response against temperature, its structure is the one that better copes with stress. The peak Von Mises stress is 14 MPa (6% of the maximum strength) and is located again in a corner between a channel and the external wall. If only the internal structure is considered, without the design restrictions of Magnum-PSI, the maximum Von Mises stress is around 8 MPa. It starts at the bottom of the structure, where the trunk meets the base.

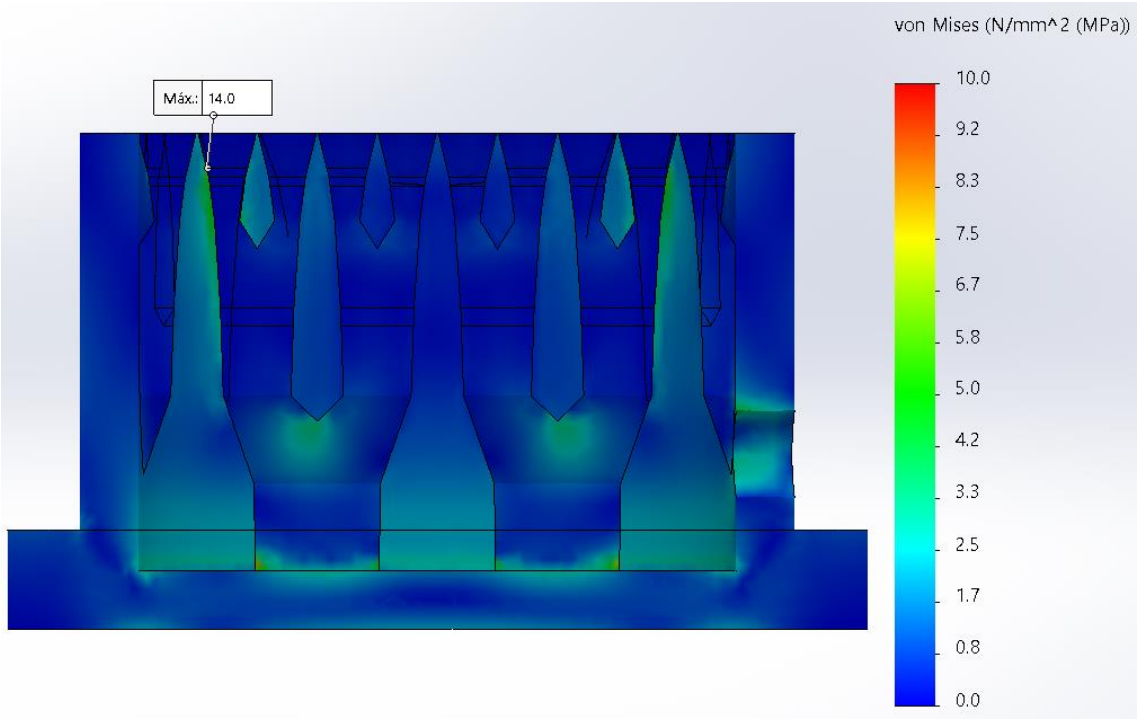

Figure 7-8 *Von Mises stress distribution of the cross section of the tree design. The plot has been rescaled to distinguish the regions under higher loads such as the corners of the bottom trunks. The maximum von Mises stress (14 MPa) and its location is also indicated in the image. In the internal structure, the peak stress is around 8 MPa.*

8 EXPERIMENTAL SETUP

The last phase of the project was to print the designs and test them under relevant fusion conditions at Magnum PSI. In this chapter the preparation of the targets for the experiments will be explained. After this, a brief description of the diagnostics used at Magnum PSI will be presented, finishing with the methodology followed during the tests.

8.1 Printing and preparation of the targets

Eight targets were printed by Smit Röntgen (three V-shape, three Tree and two Conventional) with a relative density of 94%. Before the prototypes were cleaned and heat treated, the PFS was analysed with an electron microscope (see section 9.7).

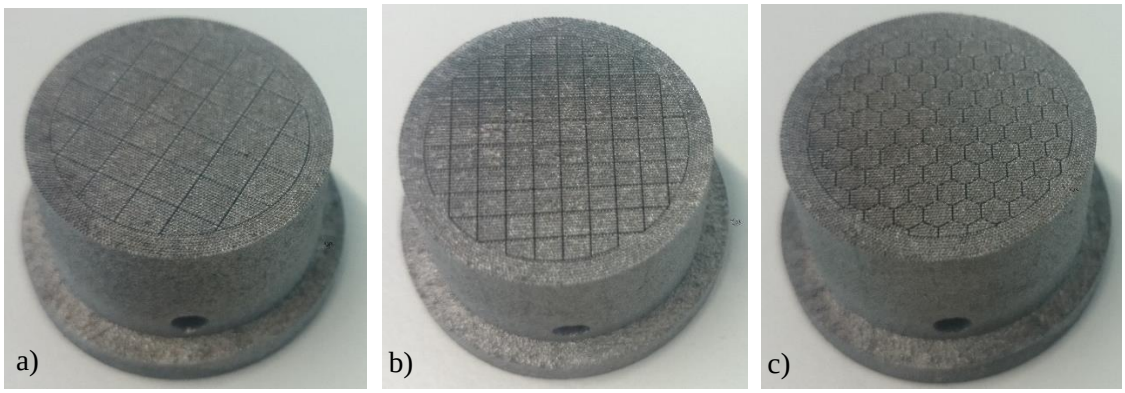

Figure 8-1 *First images of the printed targets without any heat treatment or LL inside them. From left to right, V-shape design (a), Tree design (b) and Conventional design (c). Notice that the PFS is different in every model, but the external geometry is always the same. The outer diameter is 24.5 mm (29.5 mm at the base) and the total height 17.1 mm.*

After verifying the quality of the printed texture, the targets were cleaned with ultrasound in an acetone bath for ten minutes and placed later in a vacuum furnace from DIFFER where the stress relief was performed. The thermal treatment was 2 hours at 1000ºC under vacuum conditions (pressure around 10^{-6} mbar). The heating was done in 1 hour and cooling down to RT took around 5 hours.

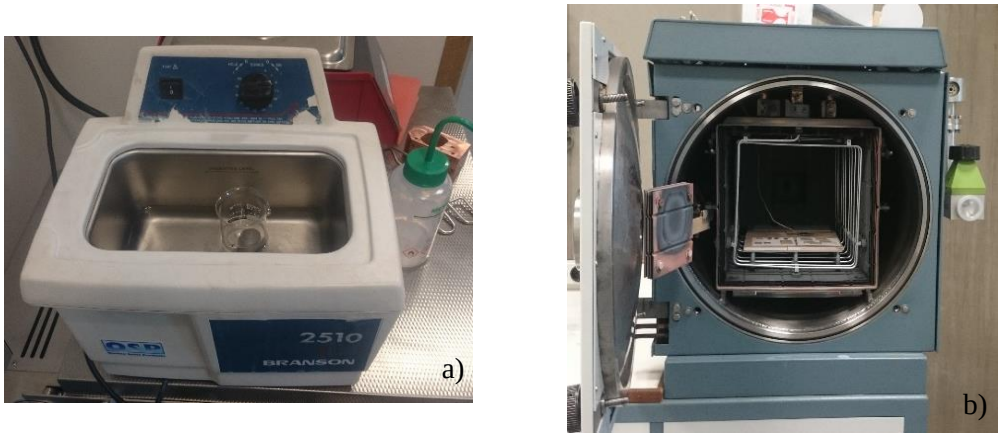

Figure 8-2 *a) The V-shape target inside the equipment used for the ultrasound bath. b) One of the two vacuum furnaces from DIFFER where the stress relief of the targets was done.*

Once the targets were cleaned and heat treated, they were introduced in a glove box where the loading with LL took place. The first step was to create a Li coating on the top surface of the targets to make the wetting of the PFS easier. To do this, the heater was set at 600ºC and Li was left to heat in small cups. The targets were placed upside down covering the cups. After one hour, the vapour had successfully wetted the PFS. Some dark regions were detected on this coating, the main explanation being some black parts detected inside the Li bars even after they were removed.

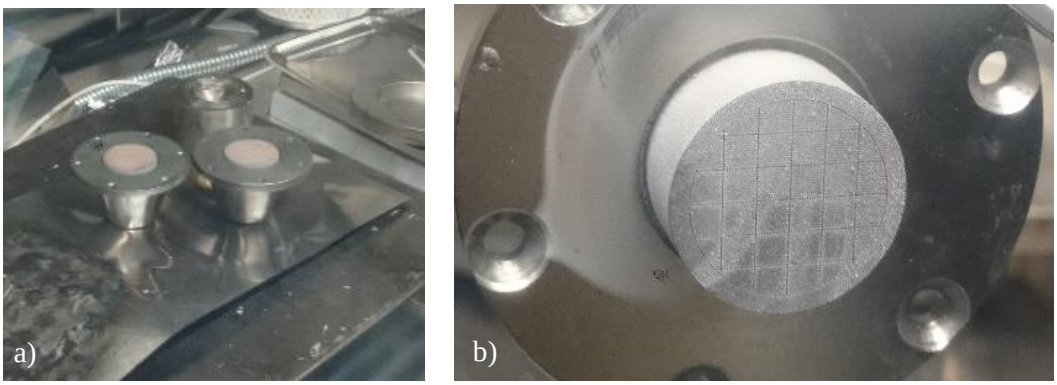

Figure 8-3 *In a) setup prepared to do the coating on the PFS by evaporation of Li. In b) the coated surface of the V-shape design after one hour. Notice the darker regions in the lower half of the PFS and how the Li has also coated the ring that supports the target.*

The initial idea was to fill the targets using an injection tool, but there was a problem with the plunger and this method could not be used. As a consequence, a second approach was proposed to load the prototypes. It consisted in soaking the targets in a LL bath, keeping the filling hole upwards so that air could flow out of the target as LL wicked inside. A bigger cup was filled with Li and heated until 400ºC approximately.

This method worked perfectly, and it was possible to see through the hole how the LL instantly filled the target when it was placed inside the bath (see **Figure 8-4**). The prototypes were left 5 minutes with the hole looking upwards and 5 minutes looking downwards to guarantee the filling.

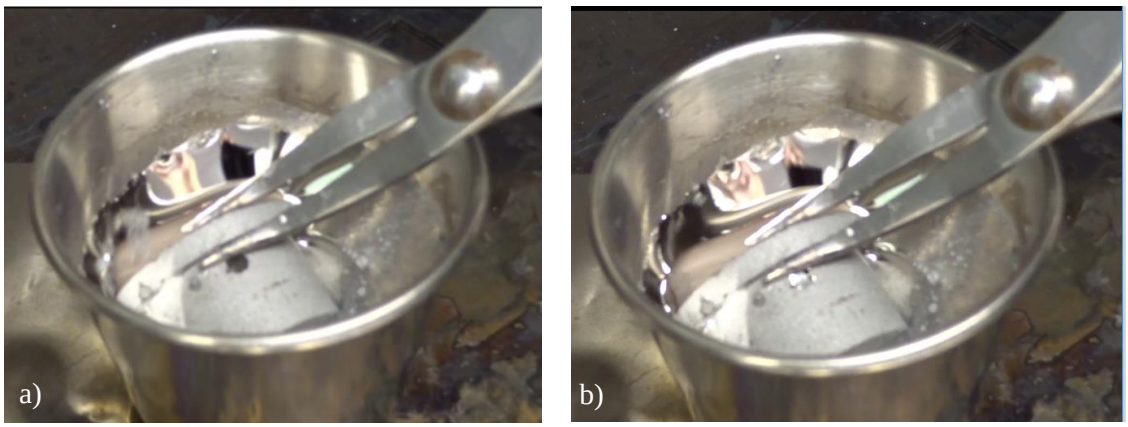

Figure 8-4 *Moment in which the conventional target is introduced in the LL bath. The filling was completed in around 0.6 s, so the filling happened almost instantly since LL can be seen coming out of the hole in the second image. Notice that the hole is above the LL bath level. This implies that the filling can only be completed by the capillary forces.*

The first target to be soaked was a V-shape but the LL was not hot enough so the filling was not as successful as with the other two. For this reason, and since one more prototype of each porous design had been heat treated, it was decided to fill a second V-shape target. During the cooldown, it was noticed that the lithium on the textured surface had contractions every few seconds and produced small bubbles. This was probably caused by the shrinking that the liquid to solid phase involves and the air flowing out of the target.

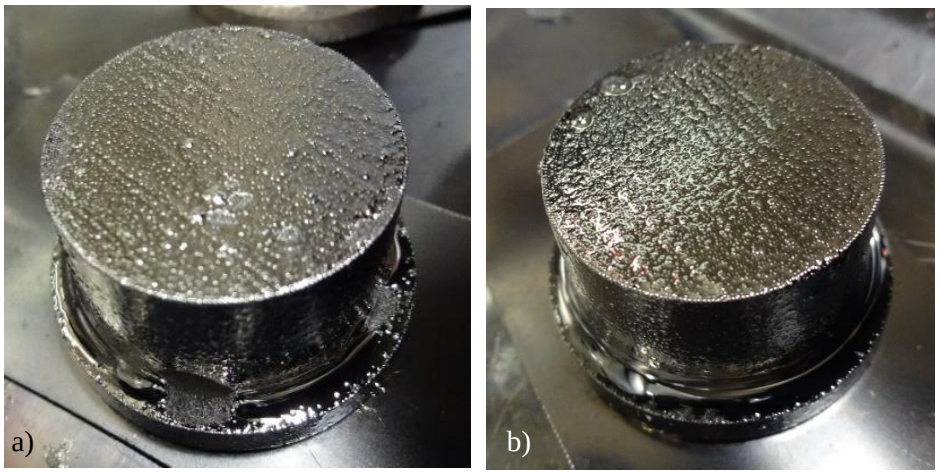

Figure 8-5 *Conventional (a) and tree (b) targets filled with Li and waiting to cool down. On the top left hand side of tree PFS it is possible to distinguish two bubbles. These appeared when the Li was cooling and solidifying.*

The last part of this preparation was to remove part of the excess of Li located outside the targets, both at the base and in the corners between the base and the main body as seen in **Figure 8-5**. This was done with metal files once the targets had cooled down and the Li solidified. Attention had to be payed in order not to damage the walls.

To know how much Li had been inserted inside the targets, they were weighed before and after this process. The results show that more Li than expected according to the CAD files was stored inside the prototypes, making the LL bath approach successful. All the weight measurements can be found in the Appendix E, but the amount of Li stored in the prototypes was in every case above the required 1 g:

- V-shape 1: 1.54 ± 0.01 g
- V-shape 2: 1.79 ± 0.01 g
- Tree: 1.78 ± 0.01 g
- Conventional: 1.24 ± 0.01 g

Other preparations had to be done before starting the experiments. These included cleaning the clamping rings with sandblast and ultrasound bath or cutting the grafoil rings that were placed between the targets and the clamping rings.

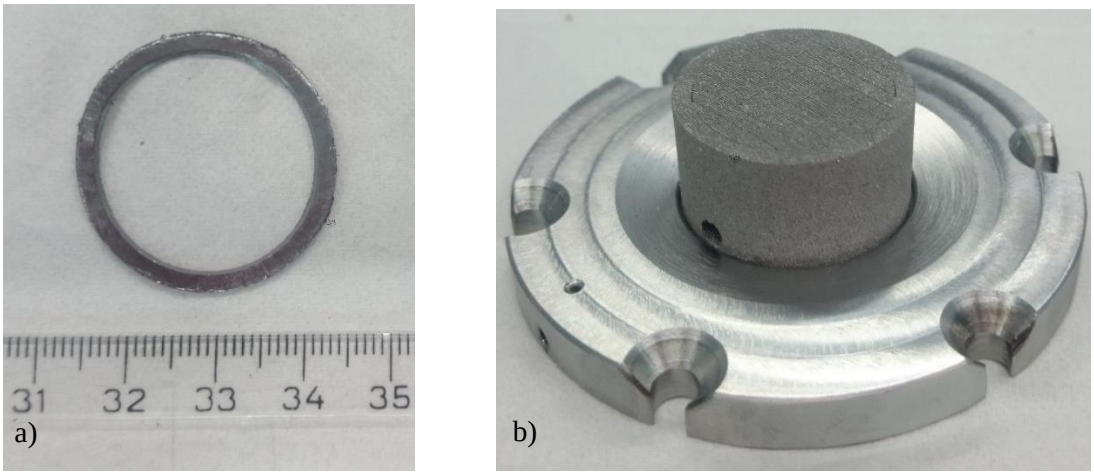

Figure 8-6 *a) One of the grafoil rings prepared to be placed in the interface between the top of the target's base and the clamping ring (see **Figure 8-8.a**). The external diameter is 30 mm and the internal is 25 mm. b) Tree design placed inside the clamping ring before the pre-load to check that everything fitted correctly.*

The dummy target used for the experiments was a 3D printed tungsten disc that had not been used for the Laser Flash Analysis. This was also cleaned with ultrasound bath and stress relieved together with the rest of the targets.

Finally, a reflex camera with a tripod was placed looking at one of the windows of the TEAC to get good images from the targets after each exposure. To improve the lightning inside this chamber, a lamp was attached to one of the roof windows as can be seen in **Figure 8-7**.

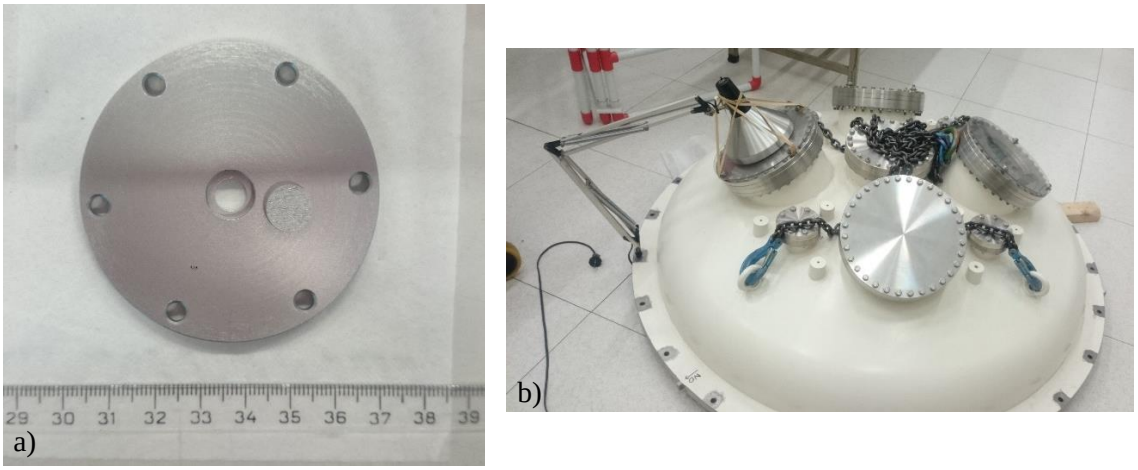

Figure 8-7 *a) The printed disc used as dummy placed on top of the clamping ring used to install it on the target holder. In both types of clamping rings, the distance between two opposite pilot holes is 60 mm. b) The roof of the TEAC with the lamp fixed facing one of the top windows to improve the lightning inside the chamber.*

8.2 Diagnostics used at Magnum PSI

As mentioned in section 2.4, different instrumentation is available to analyse the tests done at Magnum PSI. For the experiments performed in this project, the following equipment was used:

1) Pyrometry: a pyrometer was used to measure the temperature at the centre of the PFS by reading the IR emission. Since this equipment does not give reliable readings for tungsten below 700ºC and is not capable to measure Li radiation, the pyrometer was mainly used to calibrate the radiometry parameters of the IR camera during the shots to the dummy target. The model was the FMPI SpectroPyrometer by FAR Associates.

2) Infrared thermography: an IR camera was used to measure the surface temperature at the PFS and verify that the wetting of the target was correct. A 60% light filter was used to keep the readings within the operation margins of the equipment and it was calibrated with the measurements of the pyrometer. The model used was the SC7500-MB by FLIR Systems, which allows readings down to RT.

3) Fast camera imaging: a Li I filter centered at a wavelength of 670.8 nm was placed in front of the lens. This allows to monitor the radiation of Li from the coated surface and measure its intensity throughout the entire exposure. The fast camera used was the Phantom v12.1 from Vision Research.

4) Optical emission spectroscopy: visible light from the plasma was imaged onto six separate fibres connected to a 2-channel and a 4-channel optical emission spectrometer. Some fibres are located closer to the target and the rest are near the source. The model used was the AvaSpec Multichannel fibre optic spectrometer from Avantes.

5) Thomson Scattering (TS): electron density and temperature of the plasma were measured near the source to calculate the particle flux and the peak heat flux density of the plasmas. This last value was later converted into the real heat flux reaching the target, which was lower than the measured at the source (see section 9.1). TS also calculated the FWHM of the plasma beam, which was necessary to correctly introduce the Gaussian profile of the thermal load in the FEM simulations.

Further description of the equipment including its setup, calibration and error analysis can be found in TW Abrams' PhD dissertation [29]. Most of the diagnostics used for his experiments at Magnum PSI were used as well for this project, with the difference that here the TS was moved closer to the source.

8.3 Experiments at Magnum PSI

The experiments were performed on the 14th and 15th of June 2017. One day was used to mount the prototypes and align and calibrate the diagnostics. During the second day, several shots were done to the lithium targets at different plasma settings.

8.3.1 Preparation of the experiments

Once the targets were filled and the clamping and grafoil rings were ready, the prototypes were mounted on the target holder with a torque of 0.8 Nm. This procedure had to be done quickly since Li oxidizes when it gets in contact with the oxygen from the air as can be seen in **Figure 8-8.b**. Four slots from the target holder were operative, so in the central position the dummy target was placed (0º) and in the sides the V-shape (+90º), conventional (+45º) and tree (-90º) designs were installed. For the dummy it was necessary to place two grafoil layers between the cooled base and the tungsten because the central hole of the clamping ring was deeper than the height of the target.

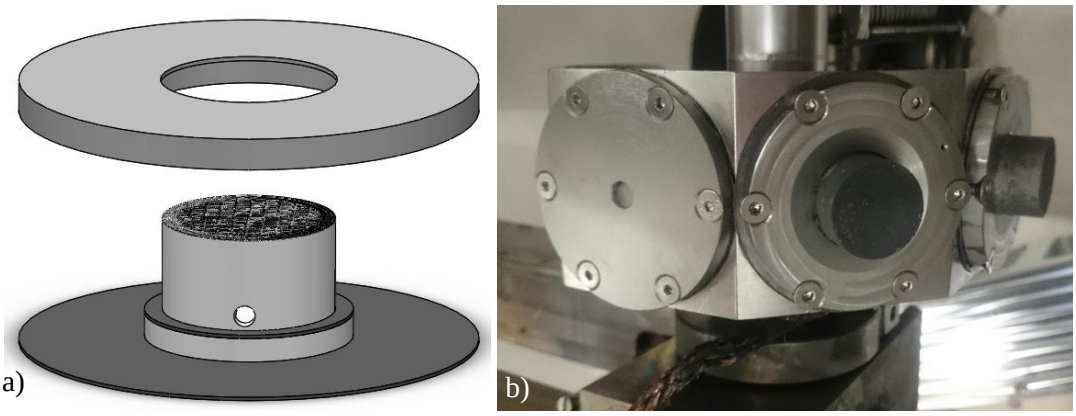

Figure 8-8 *a) Layout for the mounting of the prototypes: grafoil disc, printed target, grafoil ring and clamping ring. B) The dummy (0º) and the conventional (+45º) targets during the mounting on the target holder inside the TEAC. Notice that the prototype is very dark, this is because of the oxidized Li on the surface (remember* ***Figure 8-5****). On the right of the second image it is possible to see the V-shape target as well (+90º).*

After the targets were fixed, the TEAC was closed and vented to vacuum environment. The next step was to align the diagnostics (pyrometer, IR camera, Phantom camera) and calibrate them.

As mentioned in section 8.2, the TS was moved back to the source. Even though this does not provide as accurate readings of the heat flux hitting the prototypes as if it is pointing at the target, this was decided to prevent any sputtered Li from damaging the equipment. A simulation with the dummy was done afterwards using FEM analysis to determine the fraction of power density emitted by the source that reached the plasma-surface interaction region (section 9.1).

8.3.2 Shot sequence

Before starting each shot, the desired target is selected and the target holder rotates inside the TEAC to leave the chosen prototype aligned with the plasma beam. In standby mode, the Magnum PSI has a low power plasma made with Ar gas. This beam is hitting a beam dump that protects the targets when they are inside the TEAC.

When all diagnostics are checked and the selected target is in the parking position inside the TEAC, the operator starts a 25s countdown during which the Ar plasma switches to low power He plasma, known as A mode. Few seconds after reaching A mode and after confirmation, the operator triggers the device. During the next 7 seconds, the beam dump moves down and the target is pushed forward to the plasma-surface interaction region. At the same time, the source increases the power density of the plasma beam, going from A mode to high-power known as B mode. Once the target is in the exposure position and the plasma in B mode, the 10s countdown set for each shot begins. When the timer reaches 0, the plasma switches to A mode, the target is pulled back, the beam dump goes up and standby mode starts again. **Figure 8-9** shows a graph to better understand the shot sequence:

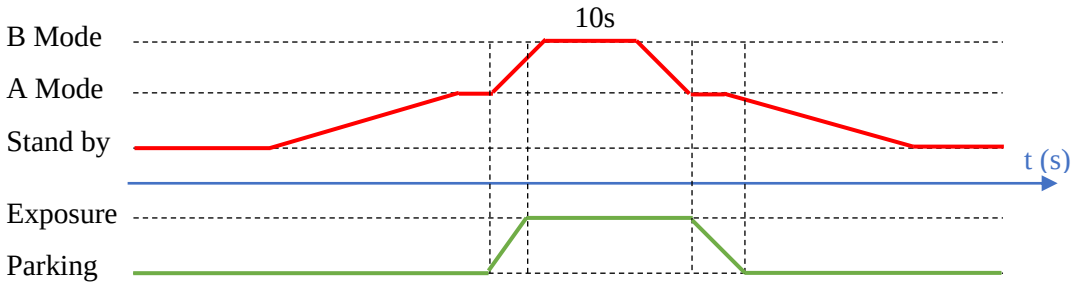

Figure 8-9 *Graphical representation of the shot sequence followed during the experiments at Magnum-PSI. The red line represents the plasma mode and the green line the position of the target. The blue axis is the timeline, in seconds. Notice that the target reaches the exposure position before the mode B starts. This is to prevent the high power plasma from damaging the beam dump.*

During the experiments, every time one setting of the B mode plasma configuration was changed (e.g. gas flow, current or magnetic field), a shot was done to the dummy target to check that the device performed well and that the integrity of the equipment and prototypes was not at risk. After this verification, shots could be done to the LL targets keeping the same settings. For all the shots done to the designs, the plasma was generated with a flow of 8 slm of He gas and a current of 125 A, but additional configurations were tested with the dummy. The most effective way to increase the heat flux was by ramping up the magnetic field. First cleaning shots started at 0.4T (14 MW/m^2 at the source) and at the end a peak value of 1.3T was reached (around 30 MW/m^2 at the source). In all the experiments, the targets were perpendicular to the plasma beam and had no bias voltage. After each round of exposures, photos of the three prototypes were taken with the reflex camera through the windows of the TEAC.

The details of the shots performed to the Li targets together with the TS results are presented in section 9.2.

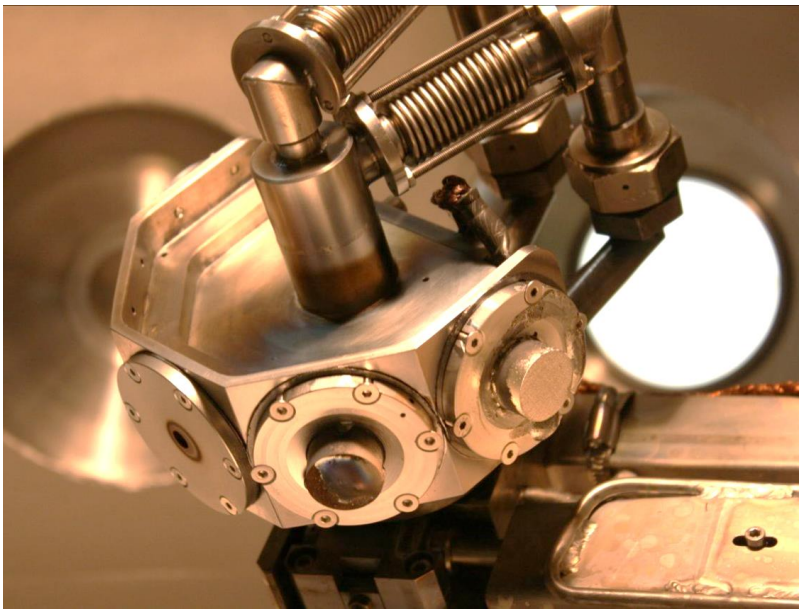

Figure 8-10 *Target holder rotating inside the TEAC with the dummy (left), conventional (center) and V-shape (right) targets. This image was taken after the shot with trigger number 9689 (see* ***Table 9-1****). Conventional model had been exposed under a heat load of 18 MW/m^2 and the V-shape under 25 MW/m^2. Notice the different colour of the targets in this image from the one they had before the exposure when the surface Li was oxidized (see* ***Figure 8-8****).*

9 RESULTS

The following chapter starts with a FEM simulation done to estimate the real heat flux reaching the surface of the targets. After this, a brief description of the shots performed to the targets is given. Finally, the measurements and images obtained with the different diagnostics used during the experiments are presented.

9.1 Heat flux density reaching the targets

As explained in section 8.2, the TS measurements were done closer to the source to avoid damaging the diagnostics with the sputtered lithium. Since an important fraction of the heat flux emitted by the source was dispelled on the way to the target, a FEM simulation was done to estimate the real power hitting the prototypes. For this analysis, the assembly showed in **Figure 9-1** was designed. The properties used for each material can be found in the Appendix D.

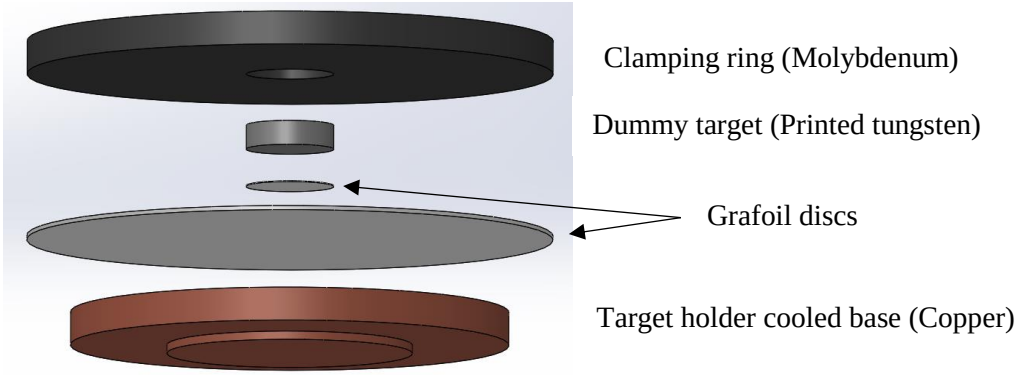

Figure 9-1 *Assembly designed to perform the FEM simulation on the dummy target. In the experiments at Magnum PSI, the target holder had a copper base that was directly cooled by flowing water at around 21ºC. On top of it, two layers of grafoil were placed in the interface with the tungsten, and a Mo clamping ring was used to fix everything.*

The boundary conditions set for the simulations were the following:

1. Fixed temperature of 21ºC at the base of the copper layer. It was directly cooled by water.
2. Initial temperature of 22ºC. Due to the geometry and dimensions of the dummy, it cooled much faster than the printed targets. For this reason, the initial temperature was lower than the one set for the analyses of the prototypes in section 7.2.
3. For the radiation losses of the clamping ring, an ambient temperature of 30ºC was set together with an emissivity of 0.08 and a view factor of 1.
4. A heat flux with a FWHM of 14.7 mm was applied on the top surface of the dummy and the clamping ring. This width was obtained from the TS reading in shot 9694 (**Table 9-1**).
5. The peak heat flux value was modified until the maximum temperature of the dummy after 10 seconds of exposure matched the measurements of the Pyrometer and the IR camera for this shot, which were 1054ºC and 1053ºC respectively. This happens when the heat flux at the center of the dummy target is 17.5 MW/m^2.

According to the FEM simulation, the necessary heat flux to set the temperature of the dummy at 1056ºC after 10s exposure is 17.5 MW/m^2. This represents 60% of the heat flux calculated with the TS reading at the source, which means that approximately 40% of the energy released by the source is lost on the way to the plasma-surface interaction region.

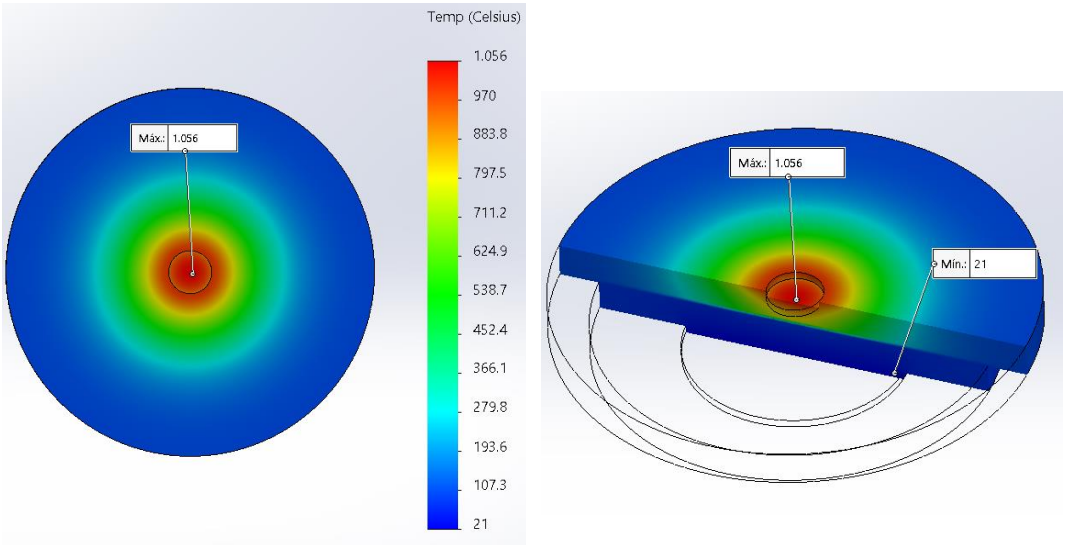

Figure 9-2 *Results of the FEM simulation of the dummy target. With a peak heat flux of 17.5 MW/m^2 and a FWHM of 14.7 mm, the maximum temperature at the center of the assembly is 1056ºC, almost the same as the measured by the pyrometer and the IR camera (1054 and 1053ºC respectively).*

9.2 Shots to the lithium targets

Table 9-1 summarises all the shots done to the Li targets. The TS was not triggered for the exposures of the conventional and the tree designs with a magnetic field of 0.6T, so no heat flux reading at the source was available. The last shot shown in the table is the one performed on the dummy used to determine the heat flux reaching the target (see section 9.1).

Table 9-1 *Summary of the shots done to the pre-loaded LL targets. The table shows the different plasma settings and the results measured with the TS for each target as well as the master trigger. In every exposure, the targets were not tilted and had no bias voltage. Heat fluxes indicated are the ones measured at the source, not the target. Notice that the particle flux calculated with the TS measurements is the same order of magnitude as the one used to estimate the LL loss rate in section 2.2.3. The empty spaces in the TS results columns are because the diagnostics were not triggered.*

		PLASMA SETTINGS				**RESULTS FROM TS AT THE SOURCE**	
Master Trigger	**Target**	**B-field (T)**	**Gas**	**Gas flow (slm)**	**Current (A)**	**Part. Flux (m^{-2})**	**Heat flux (MW/m^2)**
9678	Conventional	0.4	He	8	125	3.0E+24	14.136
9684	Conventional	0.6	He	8	125	-	-
9691	Conventional	1	He	8	125	5.1E+24	27.288
9676	V-shape	0.4	He	8	125	3.0E+24	14.240
9683	V-shape	0.6	He	8	125	3.7E+24	18.516
9689	V-shape	1	He	8	125	4.6E+24	25.028
9695	V-shape	1.3	He	8	125	5.6E+24	30.242
9685	Tree	0.6	He	8	125	3.5E+24	17.230
9686	Tree	0.6	He	8	125	-	-
9696	Tree	1.3	He	8	125	5.0E+24	28.101
9694	Dummy	1.3	He	8	125	5.5E+24	29.354

First exposures started with the magnetic field set at 0.4T and TS measurements at the source around 14 MW/m^2. The goal of these shots was to remove the oxidized layer of lithium from the PFS. After exposing the V-shape and Conventional designs, the IR camera footage showed that no melting of the Li happened. When looking through the windows of the TEAC, it was possible to see that the PFS was still covered with oxide. For this reason, the magnet was ramped up to 0.6T and, at 18 MW/m^2, the cleaning was effective. Two shots were necessary on the tree design to get a major wetting of the PFS.

Visual inspection from the TEAC's windows showed a big accumulation of LL on the PFS of the targets after the cleaning shots. These big droplets were re-melted and spread over the surface during the next shot at 1T (25-27 MW/m^2 at the source) and 1.3T for the tree design (it was not exposed to a magnetic field of 1T).

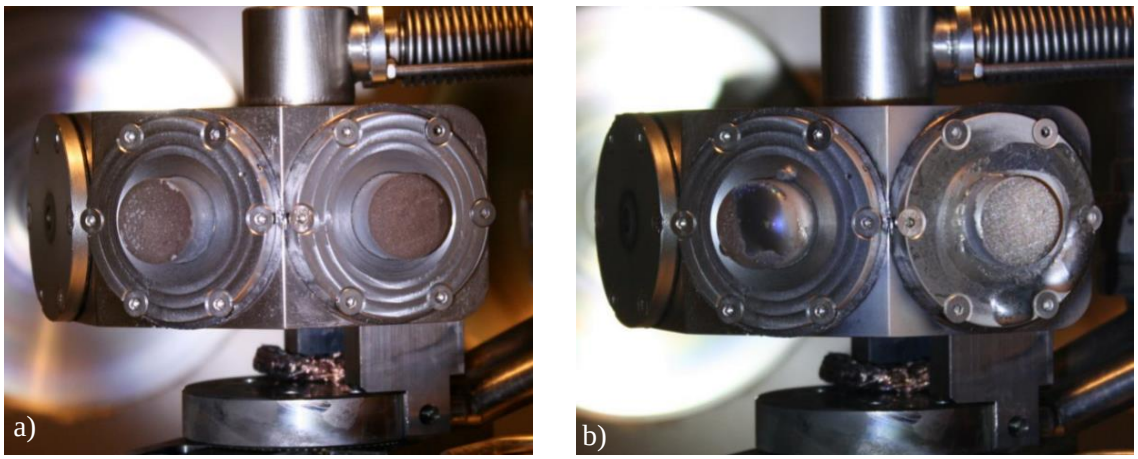

Figure 9-3 *a) Conventional and V-shape targets after the shots at 14 MW/m^2 at the source. The oxide layer can still be seen on the top surface of the prototypes. b) The conventional design after the shot at 18 MW/m^2 (left) and the V-shape design after the shot at 25 MW/m^2 (right). Notice the big Li accumulation on the PFS after the cleaning shot and how this disappeared after the exposure at 1T. Notice also all the LL deposited on the clamping ring of the V-shape design. This happened in the shots at 1T and 1.3T, caused by the LL leaking out through the filling hole of the targets.*

After the cleaning shots, the magnetic field was increased until reaching 1.3 T and around 30 MW/m^2 at the source (estimated 17.5 MW/m^2 at the targets, section 9.1). At 25-30 MW/m^2, some LL flowed out of the targets through the filling hole and deposited on the clamping rings. Higher field was tested with the dummy but there were some problems with the beam dump, so it was not possible to push the targets further. Other configurations were also tested by increasing the current or reducing the gas flow, but the heat flux did not increase according to TS data.

9.3 Lithium balance

Targets were weighed before and after the experiments to determine the lithium lost during the shots. Since no major damage on the printed tungsten is seen from direct sight or with the SEM images (see section 9.7), it is assumed that all the weight difference is caused by the loss of Li. The following table summarises these results:

Table 9-2 *Balance of the Li stored inside each prototype before and after the experiments.*

	CONVENTIONAL	**V-SHAPE**	**TREE**
Initial Li (g)	1.24	1.79	1.78
Max Power density at the source (MW/m^2)	27	30	28
Li lost (g)	0.72	0.76	0.21
Li remaining (g , %)	0.52 , 42%	1.03 , 58%	1.57 , 88%

Most of the lithium was lost during the cleaning shots with the sputtered particles and the big droplet ejected in the case of the V-shape and the conventional targets (see **Figures 9-8** and **9-14**). Another important cause for this loss is the LL that leaked through the ventilation hole of the targets and covered the clamping rings as can be seen in the following images.

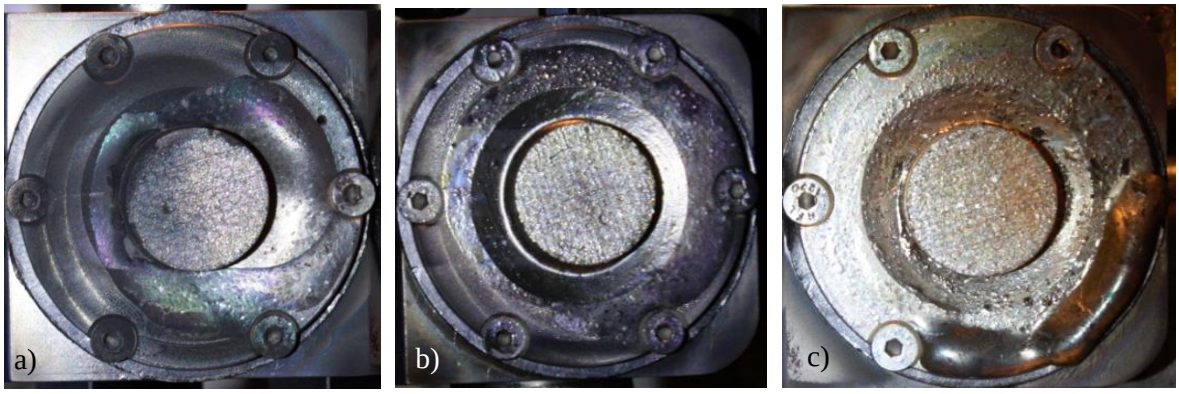

Figure 9-4 *From left to right, top view of the Conventional (a), Tree (b) and V-shape (c) targets inside the TEAC at the end of the experiments. For the three prototypes the PFS was still covered with lithium and no melted or dried areas could be seen. Notice the lithium that leaked through the filling hole and covered each clamping ring.*

9.4 Optical emission spectroscopy

A multi-channel spectrometer with 5 operative fibres was used to analyse the ions present in the plasma. The spectrum observed for all the shots to the Li targets at 0.6 T (around 18 MW/m^2 at the source) is very similar, with strong lines of He and Li during the exposure in B mode and He and Ar during A mode and stand by. Two important K wavelengths are detected as well during high power flux for the three targets, probably coming from the source and indicating it was starting to fail. Even though the integration time was checked with every shot, in some fibres saturation is observed, being the maximum reading 16383 counts per wavelength.

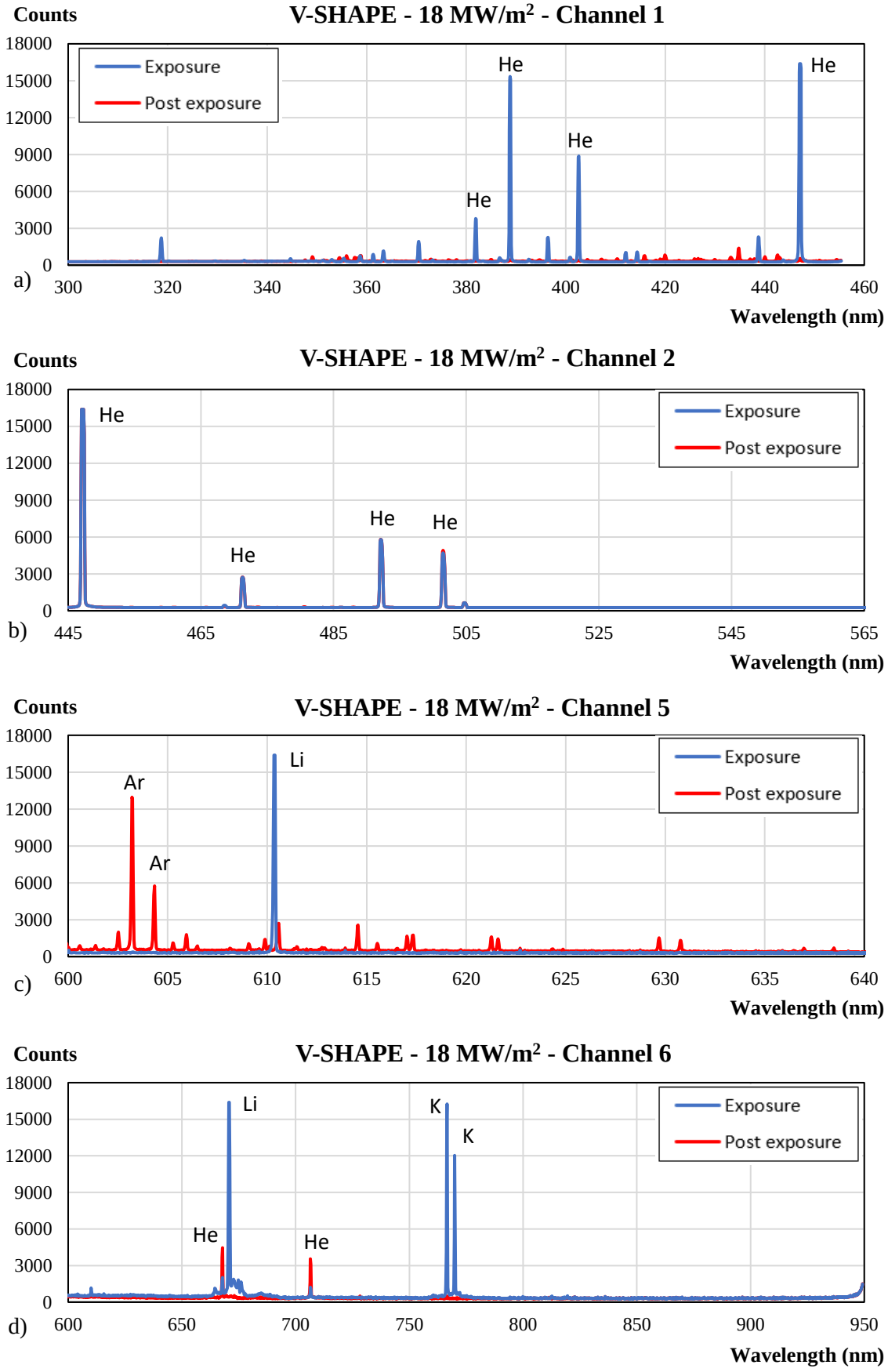

Figure 9-5 *Spectra of the cleaning shot to the V-shape target. During the exposure at mode B, Li and He lines are detected, while during the other measurements basically He and Ar lines from mode A and standby are found. Notice that two K lines are detected during exposure (d), probably emitted by the source and indicating it was starting to fail.*

At higher loads, the spectra of the shot performed to the dummy show important readings of copper, meaning that the source was close to the end of its lifespan. In addition, the spectra started to show other elements such as iron or magnesium (probably from the source). Regarding the Li targets, at higher loads more lines of He, Ar and Li are detected, and the spectra of the three prototypes is again very similar.

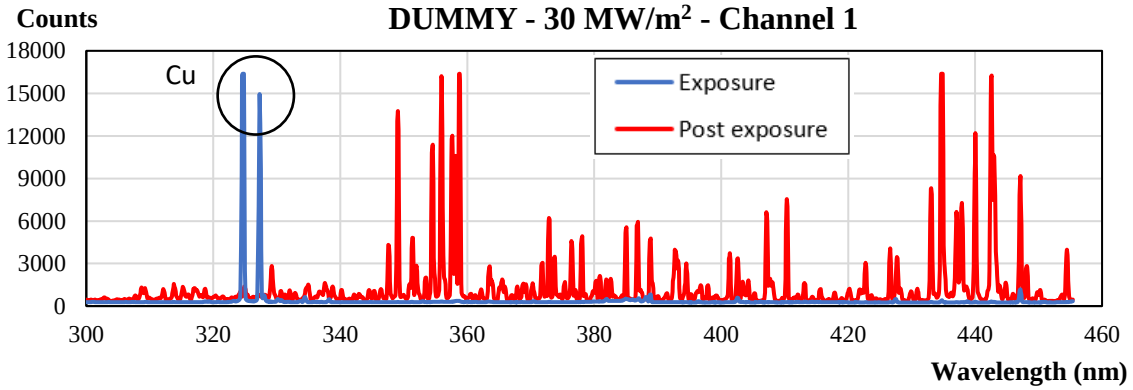

Figure 9-6 *Spectrum measured by the channel 1 on the dummy during the first shot at 1.3T. During exposure at mode B, two Cu peaks are detected. According to previous experience in Magnum PSI, these readings indicate that the source is close to the end of its operative life.*

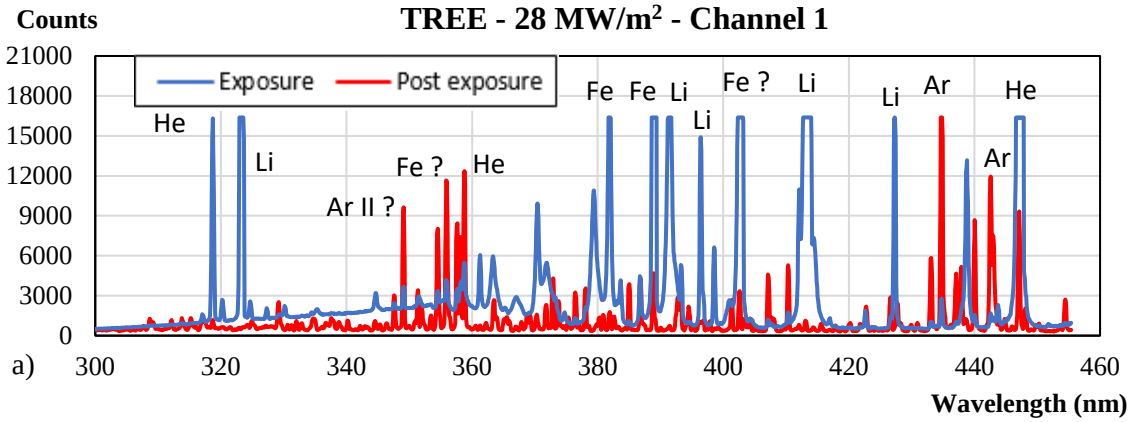

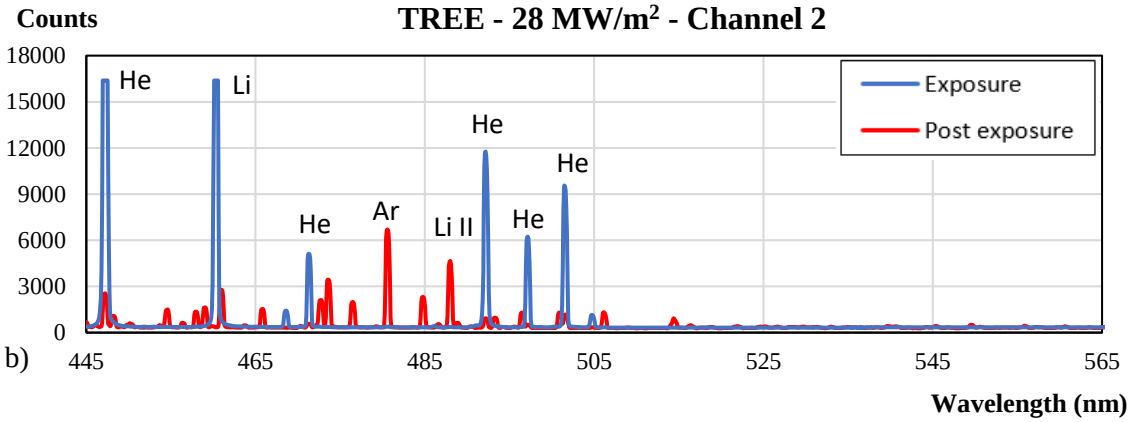

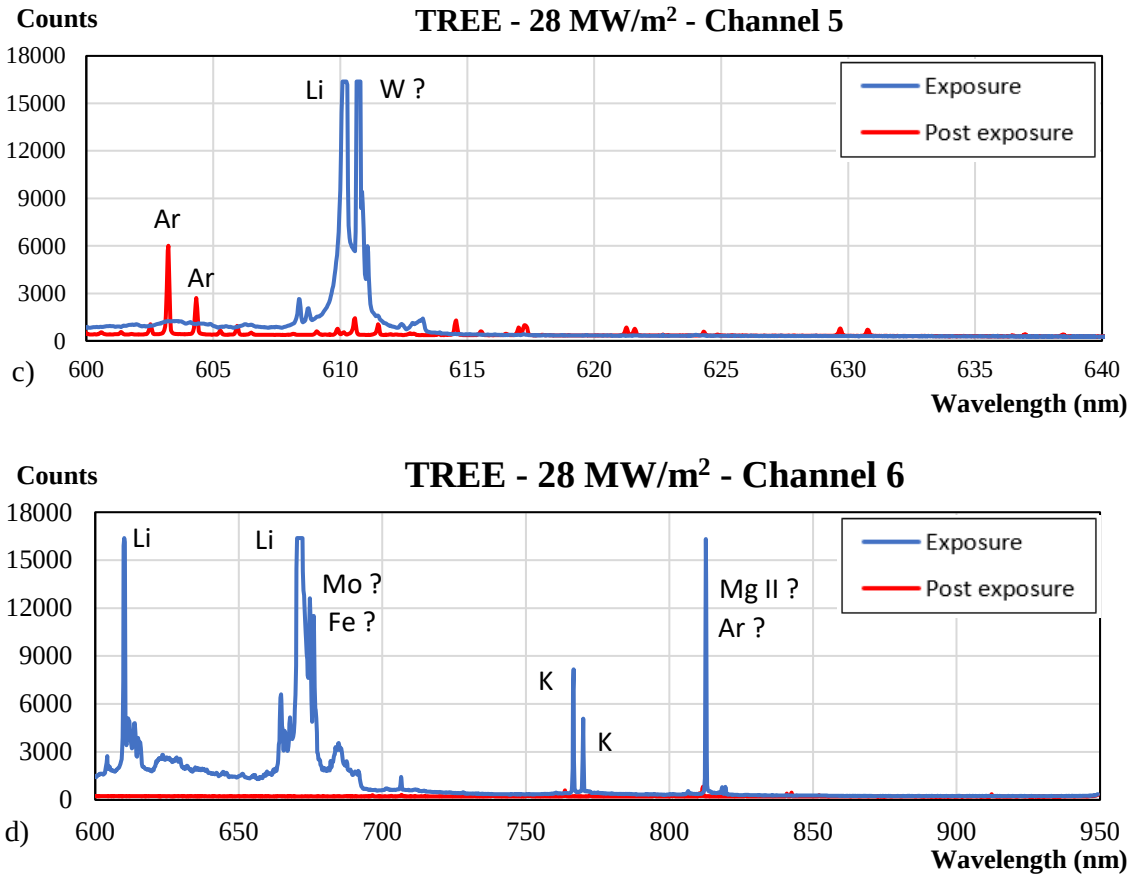

Figure 9-7 *Spectrum of the shot at 1.3T on the tree target. During the experiments with the magnetic field at this maximum value, many more wavelengths appear in the spectra from expected elements like Li, He and Ar. In addition, elements like Fe, Mg or K (a, d) indicate that the performance of the source was getting worse.*

Besides the number of wavelengths with high number of counts, another significant difference between the spectra at 18 MW/m^2 and at 28 MW/m^2 is the profile of the exposure plots. The spectra seen in **Figure 9-5** shows a rather flat line from which individual peaks rise according to the elements detected. In the spectra of the tree target the peaks are not isolated but rise from a continuum that is sometimes above 1000 counts, even though the integration time in channels 5 and 6 is one order of magnitude smaller than for the V-shape at 18 MW/m^2.

9.5 Infrared thermography and Pyrometry

An IR camera was used to monitor the surface temperature of the targets and have real time images of the LL bed on the PFS. The reading of the pyrometer on the tungsten dummy for the shot 9694 (see **Table 9-1**) was used to calibrate the radiometry parameters of the IR camera. Since no measurement of the printed tungsten emissivity was available, it was assumed that it had the same value as the tungsten filament, which at 1054ºC is around 0.17 [44&45]. At this point, the transmission was set at 35% to make the IR measurement match the pyrometer reading (1053 and 1054ºC respectively). To calibrate the LL radiometry, the transmission was kept the same and the emissivity was set at 0.1 [2]. The pyrometer does not give readings of the LL temperature so it is not possible to verify the adequacy of the chosen parameters.

As mentioned before, initial shots at 0.4T (14MW/m^2 at the source) were not enough to remove the oxide layer from the surface, which had to be done with a magnetic field of 0.6T (18 MW/m^2 at the source). The wetting did not occur at the same time in all the surface. For the V-shape and the conventional designs the LL front moved through the PFS in the clockwise direction, while for the tree it happened in the opposite direction. During the cleaning shots, a big droplet of Li was ejected from the surface of the conventional and V-shape designs.

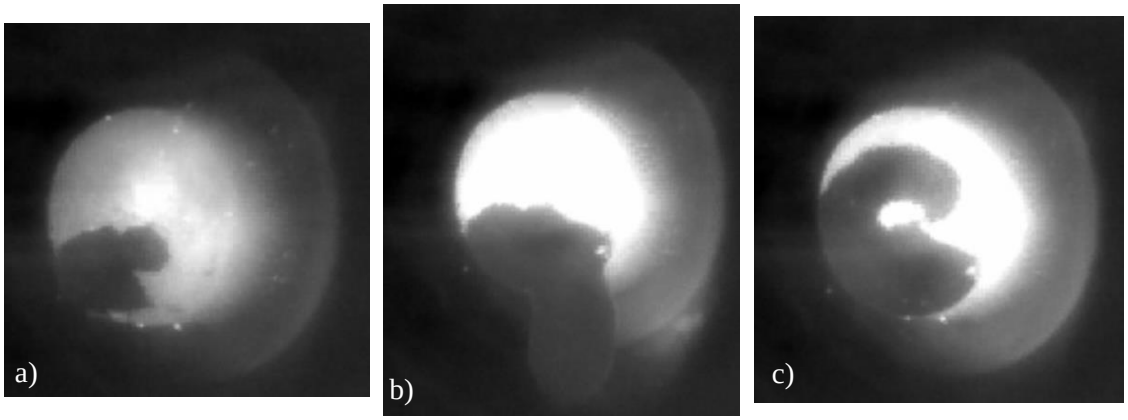

Figure 9-8 *Sequence of the cleaning shot of the V-shape design. During the exposure, the PFS was perpendicular to the plasma beam, which in the image comes from the left in the horizontal direction. The darker regions on the PFS represent the liquid lithium. Notice that a big drop of lithium is ejected during the shot, and can be seen in b). After this, the wetting of the surface began in a clockwise direction (c).*

According to the IR measurements, the maximum temperature reached by the LL is around 300ºC for the V-shape, 290ºC for the conventional and 324ºC for the tree design. The following plots show the evolution of the LL temperature during the cleaning shots of the two porous designs.

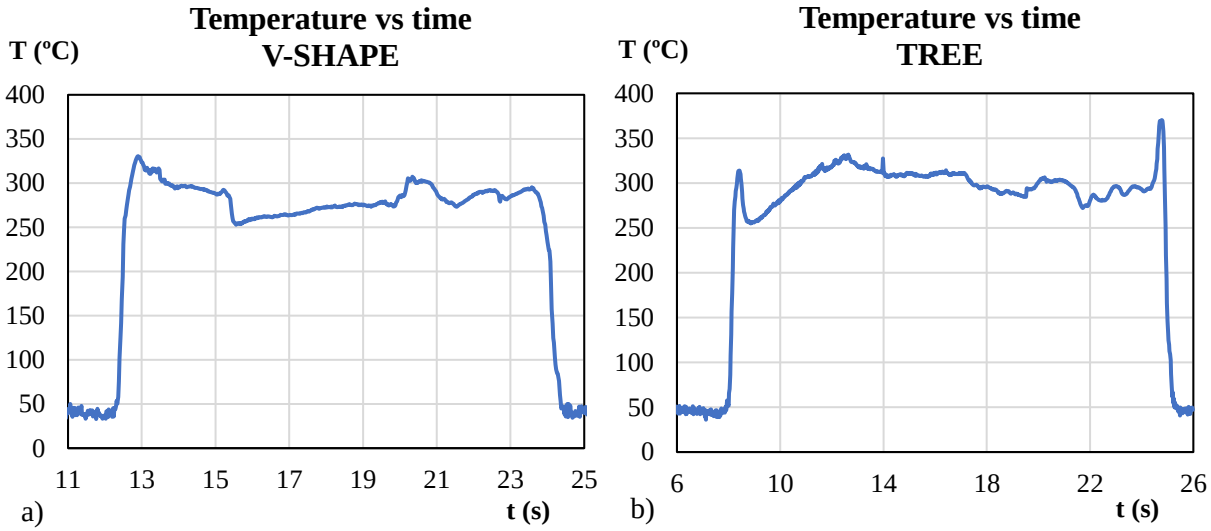

Figure 9-9 *Temperature evolution during the cleaning of the V-shape (a) and the Tree (b) designs. The plot of the tree prototype is for the second shot at 0.6T. This exposure lasted 15s to guarantee the wetting of the PFS started since in the first attempt at 18 MW/m^2 it had not. For the three prototypes, a temperature plateau is reached around 300ºC during the cleaning shots.*

Once the surface of the three prototypes was cleaned and wetted, the magnet was ramped up to 1T and 1.3T reaching heat fluxes between 25 and 30 MW/m^2 at the source and up to 17.5 MW/m^2 at the targets. In the first seconds of the shots, the LL front continued spreading through the surface of the targets. During the rest of the exposure, a bed of LL covered the PFS and no dry areas or peaks of temperature are detected. Brighter spots can be seen in the IR images but they are caused by solid particles attached to the lithium since it is possible to see them moving together

with the LL layer during the . The conventional model was not tested at 1.3T and after the exposure at 1T one edge of the prototype was still not fully wetted.

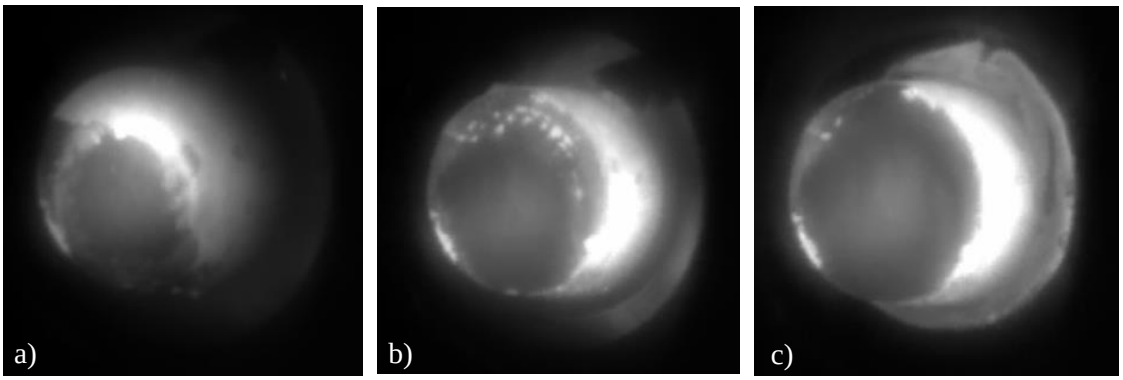

Figure 9-10 *Shot of 27 MW/m^2 at the source to the conventional target. Notice how through this exposure the LL expands to the rest of the surface until covering almost all the PFS as can be seen in the right image. Notice as well the LL that flowed out of the target through the filling hole and covered part of the clamping ring (c). In b) it is possible to see how first the channels were wetted and then the LL covered the top of the brushes.*

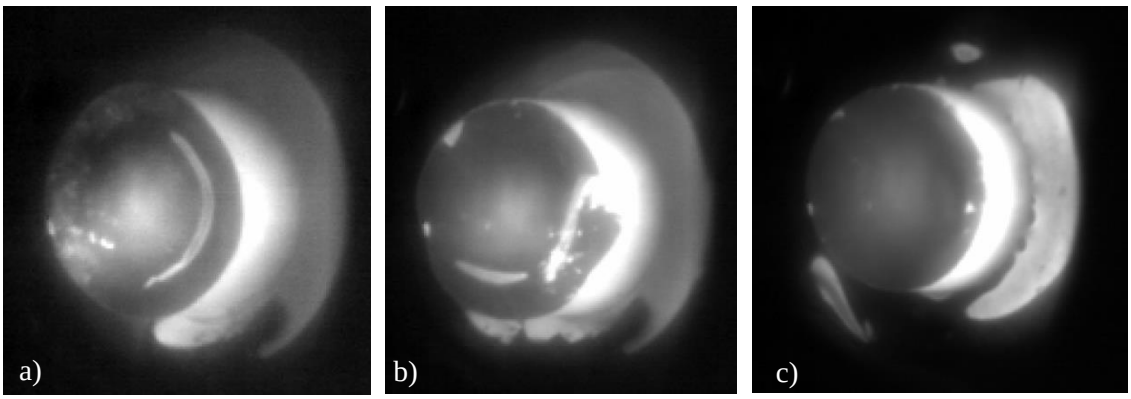

Figure 9-11 *Shot of 28 MW/m^2 at the source to the tree target. In this sequence it can be seen how in the first part of the exposure the LL completed the wetting of the PFS (a). A big drop with attached particles was moving in clockwise direction on the edges of the surface (b), but it was later absorbed by the inner structure. At the end of the exposure (c), a stable LL bed was covering all the PFS and no drops or ejections were detected. In b) it is also possible to see the LL that covered part of the clamping ring.*

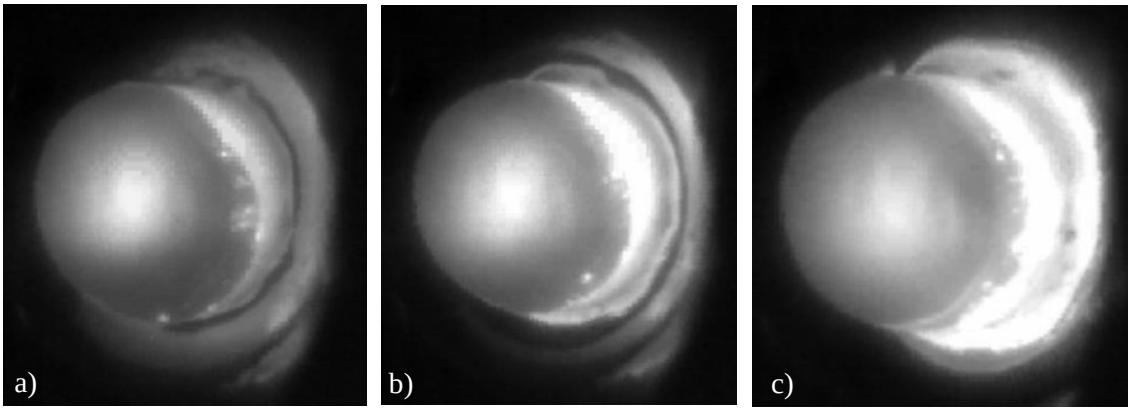

Figure 9-12 *Shot of 30 MW/m^2 at the source to the V-shape target. Through all the exposure the LL bed was present in all the PFS and no dry areas were detected. Notice two white spots at the lowest part of the surface in a), and how they move counter clockwise direction during the shot, meaning they could be particles attached to the Li.*

The pyrometer does not give readings of the LL temperature so it is not possible to contrast the measurements of the IR camera. For the selected radiometry parameters, at 1T the surface of the conventional model reached a peak temperature of 590ºC and the V-shape peaked 556ºC. At 1.3T the maximum temperature of the V-shape was 625ºC and for the tree design it was 572ºC. Temperature evolutions for all the shots can be seen in the following plots:

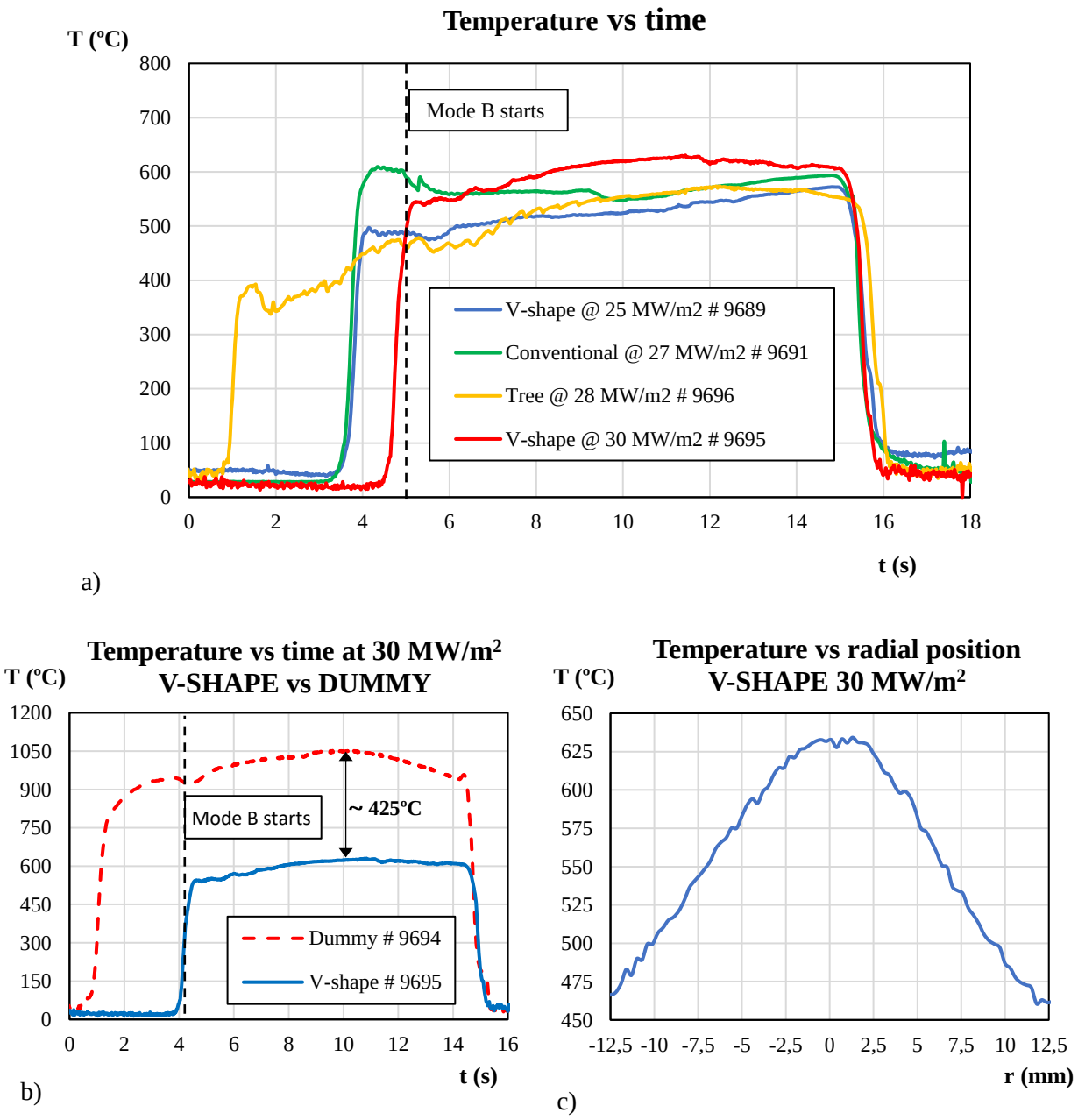

Figure 9-13 *Temperature distributions measured by the IR camera of all the shots to LL targets at high power. The number of every shot is indicated after the hash key #. Since the duration of the Mode A plasma varies in every shot, the time axes of the plots a and b have been adapted to synchronise the end of the exposure at Mode B. In a) the temperature of the LL at the center of the PFS is presented for every prototype. Notice that the measured temperature not only depends on the peak heat flux but also on other factors such as the wetting degree of the surface or the stability of the LL bed. Plot b) shows a difference of 425ºC between the dummy target (3 mm high) and the V-shape (17 mm high) during the shot at 30 MW/m². Considering that the surface cooling is more effective for the dummy, this temperature difference together with the early plateau reached in every shot indicates that the LL layer is an effective protection for the bulk W. Plot c) shows how the temperature distribution on the PFS approximates to a Gaussian profile. This is logic since the heat flux generated at Magnum PSI also follows a Gaussian profile.*

9.6 Fast camera imaging

A Phantom camera with a Li I filter was used during the experiments to monitor the radiation of Li from the PFS of the prototypes and measure its intensity throughout the different exposures.

In the first shots to the Li targets, where the magnet was set at 0.4T and the peak heat flux at the source was around 15 MW/m^2, the recorded images showed almost no trace of Li emission, meaning that the power of the plasma was too low to remove the oxide layer from the surface. The integration time (IT) was set at 800 μs.

The magnet was then ramped to 0.6T and IT for the V-shape was changed to 1200 μs. Li readings revealed that the camera was saturated, so for the conventional target the IT was set at 800 μs (again saturated) and for the tree it was set at 200 μs (still saturated) and then 100 μs (no saturation). Images show irregular shapes on the surface of the targets and a lot of particles being ejected from the PFS. The irregularities can be explained by the drops formed during the cleaning shots, such as the one in **Figure 9-8**.

The images captured with the Phantom camera show the target from the side view, where the white regions represent the emitted Li and the brightness is proportional to the counts measured by the camera. The plasma beam comes horizontally from the left and hits the tungsten target located on the right of the image. The PFS is perpendicular to the direction of the plasma and to the plane of the image, so it is only possible to see the edge of the surface.

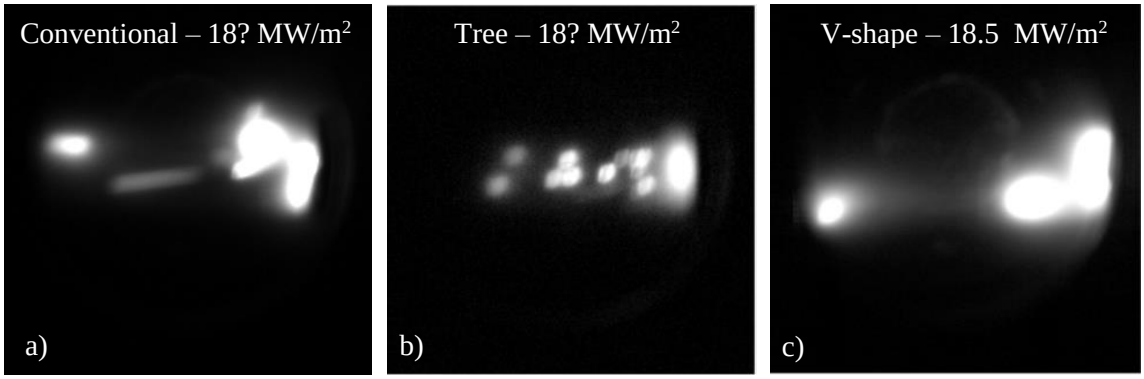

Figure 9-14 *From left to right, conventional (a), tree (b) and V-shape (c) targets during the cleaning shots. Several sputtered particles and ejections are detected with the Phantom camera, meaning that the Li oxide was effectively being removed from the surface. Notice that the camera is saturated for the shots to the conventional and V-shape targets. The indicated heat flux densities are the ones measured at the source for each shot. The TS was not triggered for the shots to the tree and conventional designs at 0.6T, but an estimated heat load has been included.*

After the cleaning, the magnetic field was set at 1T (25-27 MW/m^2 at the source) and the IT was set at 50 μs for the V-shape. The camera was again saturated, so for the conventional target the IT was reduced to 10 μs and it was saturated only in the first two seconds of the shot. When the magnet was set at 1.3T (28-30 MW/m^2 at the source), the IT was reduced to 5 μs for the shot to the V-shape and the tree targets. During these shots at the highest power, the radiated Li transitioned from an irregular profile (**Figure 9-15**) with small Li droplets and instabilities on the PFS to a steady emission (**Figure 9-16**) where the profile has the same geometry for the three targets.

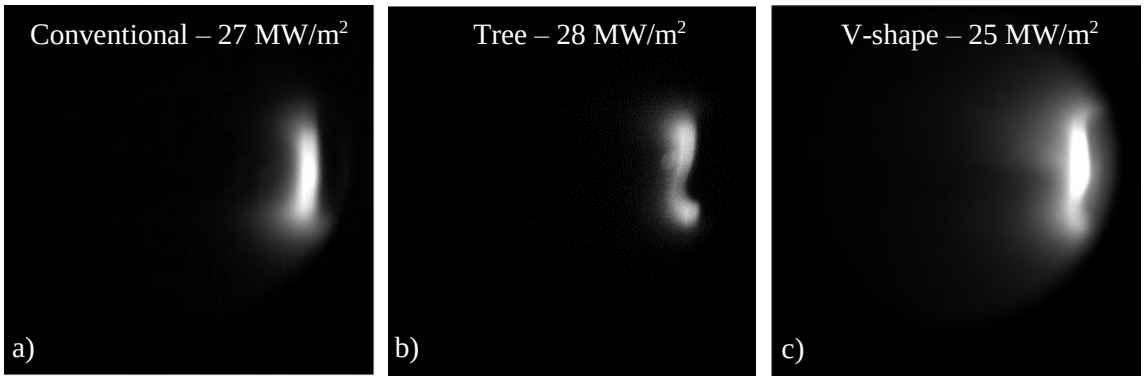

Figure 9-15 *From left to right, conventional (a), tree (b) and V-shape (c) targets before they reached the steady state condition. Notice that the profile of the emitted light is not regular. In the image of the tree target a drop can be distinguished as a round black body emerging from the flat surface. In the V-shape image, two drops can be seen, also with black round geometries.*

The three prototypes reached a stationary state that could be the vapour shield effect described in section 2.2.2. The profile of the emitted light seen in the videos has the same shape and dimensions in the three designs as can be seen in the following figure:

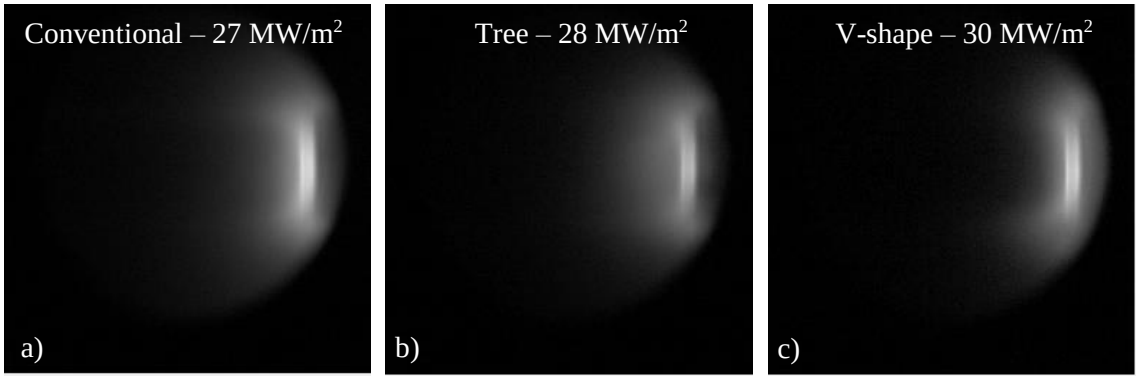

Figure 9-16 *From left to right, conventional (a), tree (b) and V-shape (c) targets once they reached the steady state condition. The profile of the emitted light has the same shape and dimensions for the three designs and no droplet ejections are detected during the rest of the exposure. Notice that in the images the light in the conventional target is brighter. It must be taken into account that the IT is 10 μs while for the other two it is 5 μs.*

According to the previous images, this profile is around 4 mm thick for the three prototypes. This makes the possibility of it being Li from the side walls rather unlikely, since images from the TEAC after the experiments show this layer is around 2.8 mm for the V-shape and does not have the same dimensions for the other two targets.

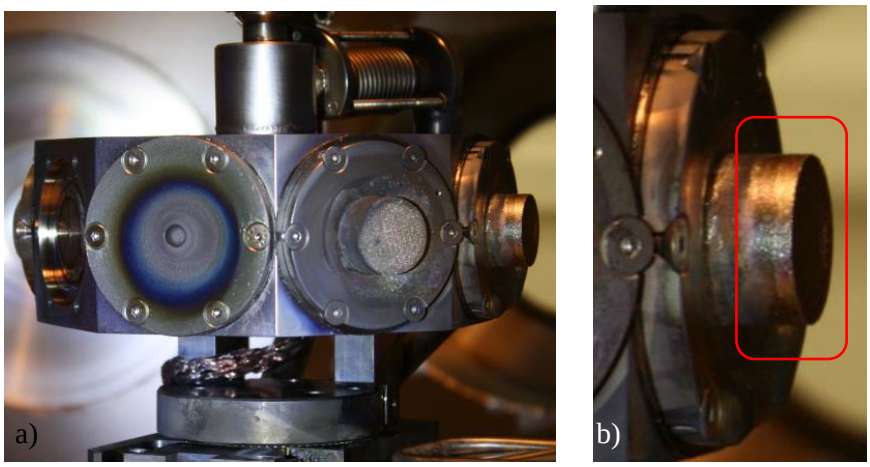

Figure 9-17 *a) Target holder with the dummy, conventional and V-shape targets after the experiments. b) Magnification of (a) showing the Li on the side walls of the V-shape target. This layer measures around 2.8 mm while the profile seen with the Phantom camera is around 4 mm thick.*

9.7 Scanning electron microscopy (SEM)

Images with an electron microscope were taken from the PFS of the targets before and after the experiments at Magnum PSI to analyse the wetting degree and to detect any damage that could occur during the exposure of the prototypes at fusion-relevant conditions.

When the prototypes arrived at the TUe they were placed in an electron microscope to analyse the quality of the textured surface. The first impression was that the distribution of the blocks followed very accurately the pattern from the CAD file, and even the bigger blocks from the edges could be distinguished. However, in **Figure 9-18.b** it can be seen that in some spaces between the blocks there are some melted bubbles, such as the one close to the bottom left corner of the tree brush. This structures are probably caused during the printing process, and are not desirable since they block the path of the LL.

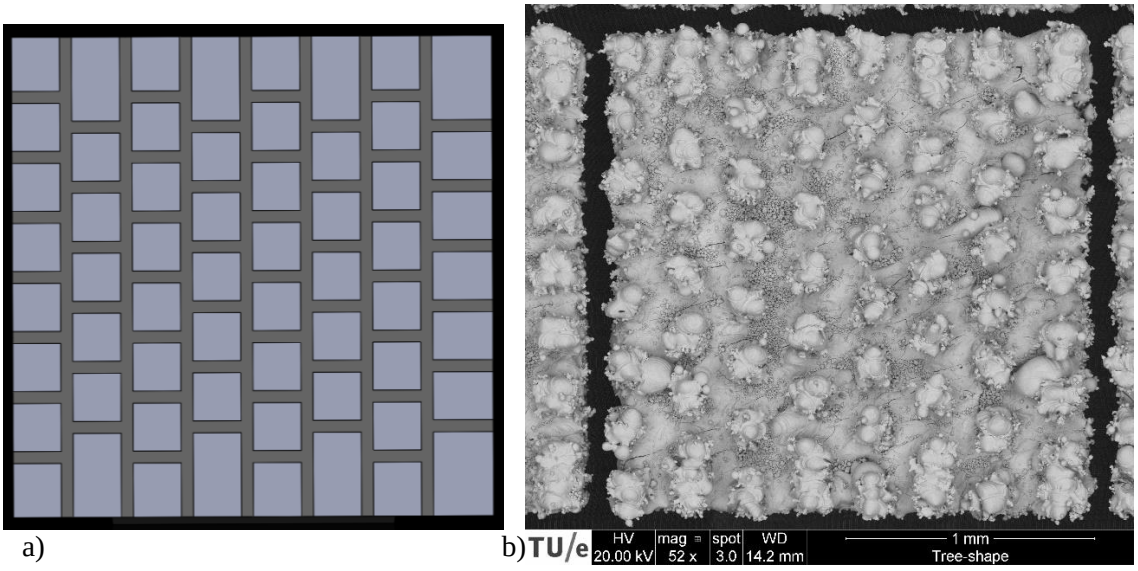

Figure 9-18 *Comparison between a brush from the tree design of the CAD file (a) and the printed target seen with the SEM (b). Notice the pattern of the printed structure and the difference between the size of the central blocks and the ones on the edges of the brush, following with high accuracy the designed texture.*

When giving a closer look as shown in **Figure 9-19**, it is possible to detect the accumulation of un-melted W particles (1) and the formation of small cracks (2) originated during the printing process. Notice as well that the blocks' surface is almost half from the designed value (3) and that the separation channels are a bit wider (~100 µm instead of 50 or 60 µm).

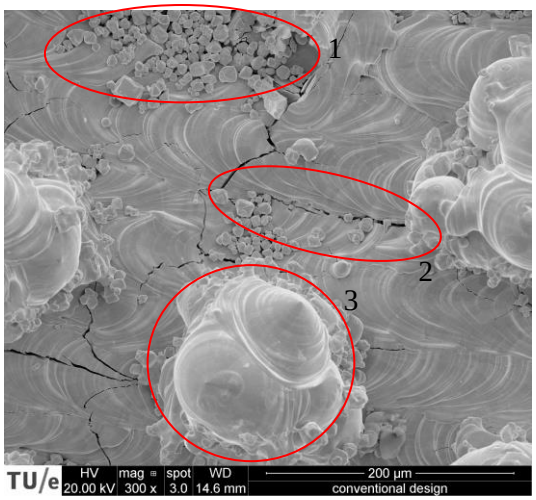

Figure 9-19 *Zoomed image of the printed brush from the conventional design. An example of particles accumulation (1), a small crack (2) and a surface block (3) are marked in red.*

In the three designs, but especially for the tree target, it was seen that many brushes had some blocks missing (see **Figure 9-24.a**). This damage was probably caused during the transport of the printed parts to the TUe facilities since they were not individually packed. Despite these details, the printing precision and the level of detail reached are extremely high, allowing the conceptual design of the textured PFS to become a reality.

After the ultrasound cleaning and the heat treatment, the surface of the tree design was inspected. It was noted that the ultrasound bath had removed most of the un-melted W particles, but there was still some accumulation around the blocks. The cleaning together with the bath were effective to remove the black regions from the tungsten (see **Figure 9-24.a**), probably caused by impurities during the printing process.

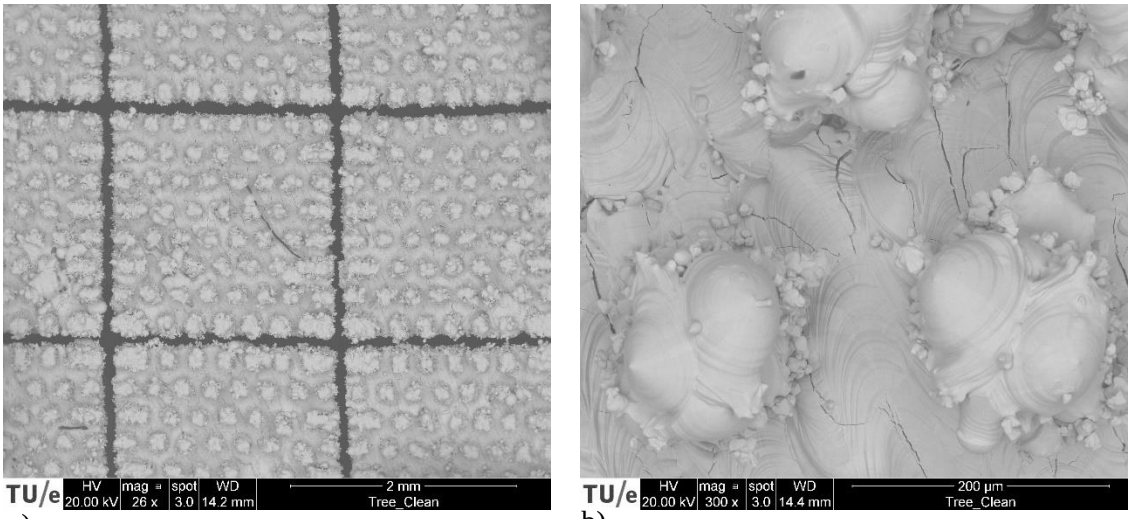

a) b)

Figure 9-20 *Images from the tree prototype after the cleaning with ultrasound bath and stress relief. Notice that almost no un-melted tungsten particles can be seen between the blocks, only some which are attached to the blocks. The dark line in the middle of the brush of the left image is a fibre from the sponges used to protect the targets.*

Four targets were cleaned, heat treated and pre-loaded with lithium but only three were tested at Magnum PSI. Since one of the V-shape designs was not exposed to the plasma, it was scanned with the electronic microscope to see in detail the wetted surface after the filling process.

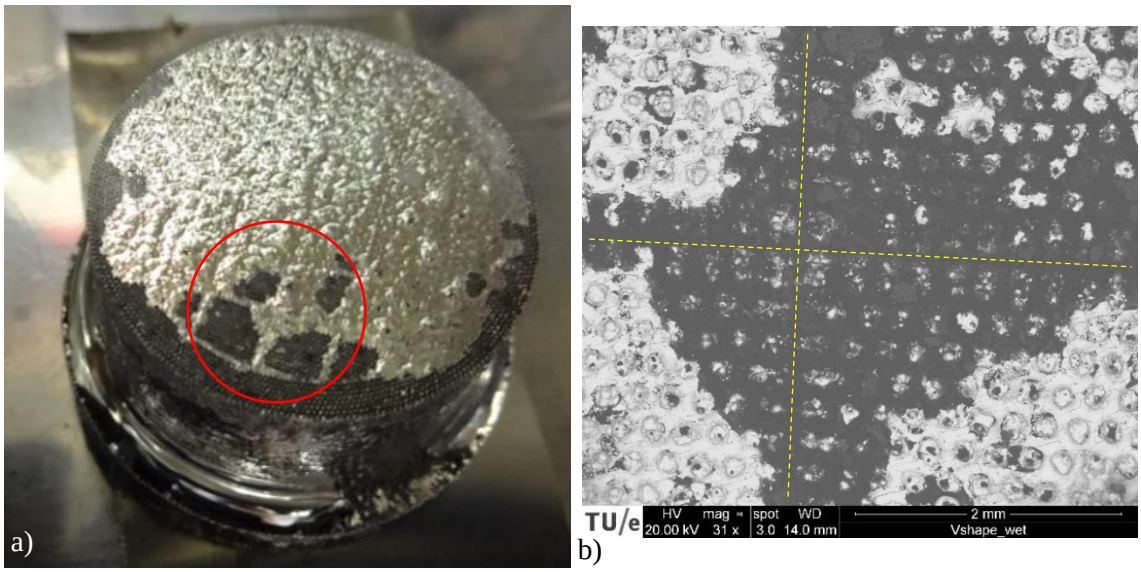

Figure 9-21 *a) V-shape target that was not tested inside the glove box. The marked region in red is the area seen on the right with the SEM (b). The white material in b) is the tungsten and the black areas are the lithium. For a better understanding, the wicking channels have been indicated with a yellow dotted line. From these two images it can be deduced that most of the wetting of the PFS is not through direct deposition but by capillarity from the channels to the center of the brushes.*

Low magnification showed that the LL expanded through the PFS by capillarity from the wicking channels to the center of the brushes. When the image is zoomed in, it is possible to see how the LL wicked between the surface texture. The following image shows as well how LL drops deposited on top of the surface blocks during the LL bath.

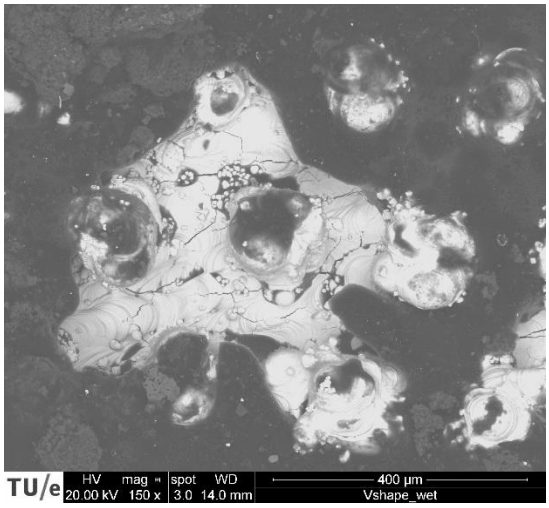

Figure 9-22 *Magnification of the surface of the V-shape target that was not exposed to plasma. The black area represents the lithium and the white region the tungsten. Notice how the LL wicked between the surface texture to wet the PFS and how LL drops were deposited on the blocks during the soaking of the target in the LL bath.*

After the experiments at Magnum PSI, the surface of the three prototypes was analysed again to see the wetting conditions and identify if there was some damage of the PFS. For the three targets, the surface was fully covered with lithium and only the peaks of the blocks could be distinguished. In addition, no melted blocks were identified. A small difference can be seen, however, in the thickness of the Li layer between the center and the edges of the targets. In the three cases, the

visible peaks of the blocks at the edges are smaller than those of the center. This means that the Li layer is thinner in the center, where the plasma beam is more powerful. No significant differences were found between targets.

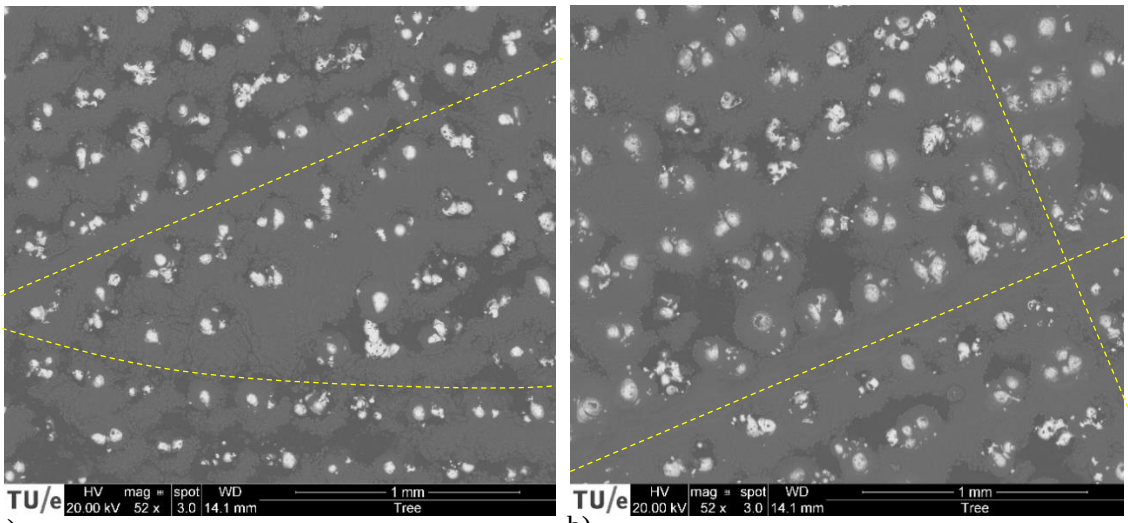

a) b)

Figure 9-23 *PFS of the tree design after exposure at Magnum PSI. a) Detail of an external brush and part of the circular edge. b) Detail of some central brushes. The wicking channels between brushes have been marked with yellow dotted lines. Notice that the white peaks on the left are smaller than those of the right.*

The last part was to remove the Li from the prototypes in a bath with acid solution and check the surface for damaged or melted parts. This analysis had to be performed under low vacuum conditions (0.6 mbar) since the pump of the electron microscope was not capable to reach stable high vacuum (10^{-4}-10^{-6} mbar). At low vacuum, lower voltage had to be used (HV in the legend of the images) and as a result some dirt can be seen on top of the surface as black spots. In addition, fibres from the protection sponges can also be identified in **Figures 9-24.b** and **9-25.a**.

The new images taken from the three exposed targets reveal that the brushes of the conventional and V-shape designs were almost intact, but the tree target had several missing blocks. It is unclear if this damage was caused by the plasma exposure or during the transport and manipulation of the targets, as the central brushes of the prototype had many undamaged blocks as well.

In these SEM images a colour filter was applied by the operator of the microscope to better distinguish the different elements of the surface. The tungsten was not coloured; without this filter the images would have the same look as the ones in **Figures 9-18** or **9-19**.

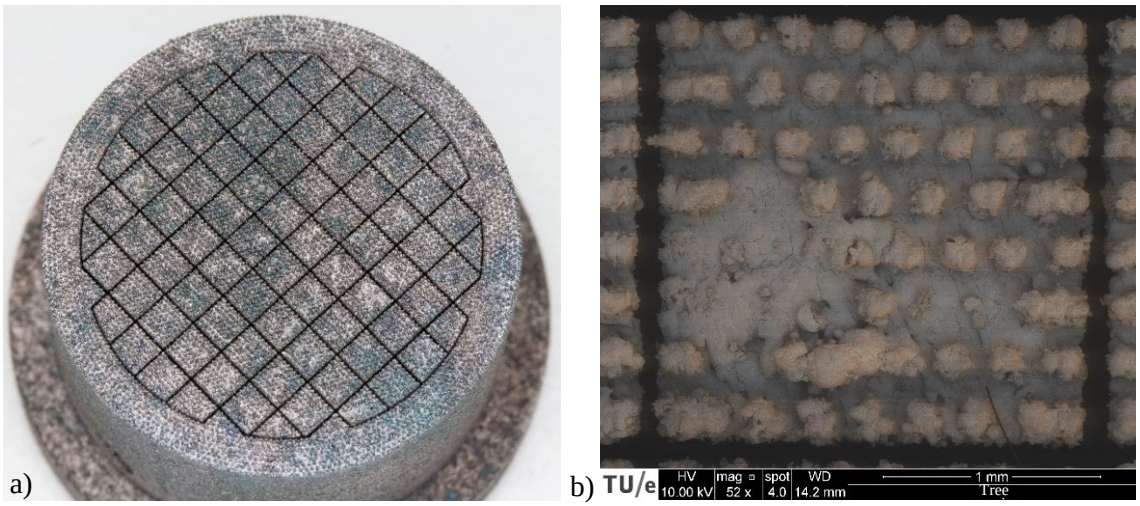

Figure 9-24 *a) Surface of the tree target when it arrived at the TUe facilities, where it can be seen that the brushes had already some damage. b) One of the most damaged brushes of the tree target. It is not clear if this damage was caused by plasma or during manipulation of the prototype since several undamaged blocks were also present. Besides the big area without blocks, it can also be seen that there are almost no un-melted W particles when compared* ***to Figure 9-18.b****.*

The following images show the central brushes of the exposed V-shape and conventional models. Since the plasma had a Gaussian profile, these are the ones under the peak heat flux, but all the texture of the brush is intact.

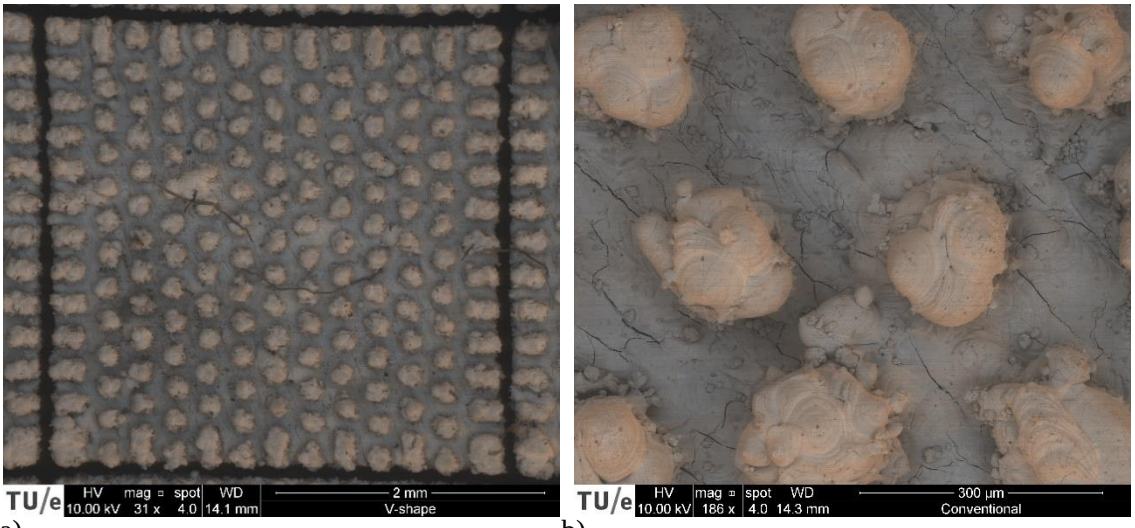

a) b)

Figure 9-25 *a) Central brush of the V-shape design. All the blocks of the texture are intact. b) Magnification of the central brush of the Conventional design, where almost no tungsten particles can be seen. Notice that some dirt can be seen on top of the material as small black spots.*

10 SUMMARY

This chapter is intended so briefly put together all the main results obtained in this project before proceeding with their analysis in the next chapter.

a) Material characterization

The combination of variables that results in the highest strength is to perform a stress relief to the samples and print them with the highest relative density achievable. Unlike conventional metals, higher temperature also seems to bring a higher fracture stress. Regarding the thermal diffusivity, higher density and stress relieving the samples result in the highest values. Temperature plays an important role here, reducing the diffusivity by 34% when heating the specimen from RT to 600ºC. The following table summarises these results:

Table 10-1 *Results of the tensile tests and the laser flash analysis performed on the 3D printed tungsten samples. For the two heat treatments, percentages represent the comparison with the untreated samples.*

Properties	**Stress Relief**	**Recrystallization**	**Density (93% vs 84%)**	**Temperature**
Strength (Tensile)	+20%	-5%	+37%	+10% (600ºC vs 350ºC)
Thermal Diffusivity	+10%	?	+10%	-34% (600ºC vs 21ºC)

b) Experiments at Magnum PSI

Three prototypes of a pre-loaded liquid lithium divertor target were tested at Magnum PSI under different heat loads. Each design has a different internal structure and PFS geometry. Cleaning of the lithium oxides was effective at peak heat fluxes of about 18 MW/m^2 measured at the source. The prototypes were exposed during 10s at maximum heat loads of 30 MW/m^2 at the source (estimated around 17.5 MW/m^2 at the targets). Spectroscopy indicates that during the cleaning shots the source was performing correctly, but when the magnetic field was ramped to 1T and 1.3T the source started to fail, releasing Cu and K ions and causing some oscillations in the plasma. Infrared thermography shows a temperature plateau around 600ºC for the lithium targets while the dummy disc was heated above 1050ºC even though it had better cooling given its dimensions. The images recorded with the different diagnostics after the cleaning shots show a stable LL bed on the surface without dry spots and the profile of the radiated Li light indicates the formation of a vapour shield in the interface between the plasma and the PFS. Analyses with an electron microscope show almost no damage of the tungsten caused by the exposure under fusion relevant conditions. Finally, lithium balance performed on the prototypes suggests that almost all LL loss of the targets is caused by the big droplet ejected during the cleaning shots and the leakage through the ventilation hole that covered the clamping rings with LL.

11 DISCUSSION

One of the major challenges for the fusion community is to develop a divertor that can withstand the increasing heat loads and particle fluxes in the future tokamaks such as ITER or DEMO. The goal of this project was to design a divertor target manufactured using 3D printing technology that could be pre-loaded with liquid lithium and could stand heat loads of 15 MW/m^2 during 10s at Magnum PSI. The results from the printed tungsten characterization, the analyses of the designs and the performance of the prototypes during the exposure under fusion relevant conditions have been presented in chapters 3, 7 and 9 respectively. In this section, these results will be discussed.

11.1 Material characterization

The tensile tests show that, like with other 3D printed materials, the mechanical properties of the conventionally manufactured tungsten cannot be extrapolated to the printed metal. In this case, strength of the metal increases with temperature and by stress relieving the sample at 1000ºC during 2h. Similar results were found in a study performed by NIST on the printed austenitic stainless steel [38]. As it happens with conventional metals, recrystallizing the sample at 1600ºC during 1h or increasing its porosity reduces the strength of the material. It was also observed that both heat treatments reduced the Young's modulus, but since this difference was smaller than 20 GPa, it could originate from the irregularities of the specimen dimensions such as insufficient plane parallelism of the surfaces [1].

None of the tensile specimens tested reached plastic deformation, thus breaking during the elastic phase. One hypothesis is that the tungsten was still in the brittle regime at 350ºC, but the test at 600ºC confirmed that this might not be the cause. The reason why these samples do not reach plastic deformation is probably because of the presence of cracks and irregularities from the printing process. Images taken with the electron microscope, such as **Figure 9-19,** show the number of fissures on the surface, which could have been generated by the fast cooling after the laser melted the material. Stresses accumulate on the edges of the cracks, thus expanding the fissure and causing the failure of the sample.

Since no plastic deformation was reached, the failure stress was used as the limit of the material when applying the Von Mises criterion in the FEM analyses. A safety factor of 1.2 was considered to compensate for the uncertainties of the tensile test (only one specimen tested per condition) and because thinner parts such as the textured surface were expected to be weaker (when the printed part is thinner than 1 mm, lower relative density is achievable and thus the strength is reduced). As a result, the limit of the stress relieved tungsten at 600ºC was set at 225 MPa.

As expected, thermal diffusivity increases with density and decreases with temperature. There seems to be a linear relation between the relative density and the thermal diffusivity, but more tests should be done to confirm this hypothesis since only two grades were analysed (93% and 84%). This result seems logic though since the amount of material to conduct heat is proportional to the density. It was also found that stress relieving the sample improved the diffusivity by 10% approximately.

For the 93% relative density and stress relieved specimen, the thermal diffusivity was slightly lower than that of the conventional pure tungsten with 99.97 wt% purity [1]: 58 vs 73 mm^2/s at RT and 38 vs 50 mm^2/s at 600ºC. If the thermal conductivity is calculated using the density and specific heat capacity provided by Smit Röntgen, the printed tungsten still has lower values, being 166 vs 185 W/m·K at RT and 109 vs 150 W/m·K at 600ºC [1]. The properties provided by Smit Rontgen are measured at RT, but according to M. Wirtz the density of 99.97 wt% purity tungsten only decreases by 0.8% from RT to 600ºC while the specific heat capacity increases by 3% [1].

Thermal diffusivity has not yet been determined for the recrystallized specimen. If it turns out that the diffusivity is higher than the one for the stress relieved sample, the failure criterion mentioned in section 4.2 should not be applicable. Even though the strength of the recrystallized material is slightly lower than the stress relieved, better thermal conductivity in the upper layers of the target is preferable to better exhaust the heat from the PFS. FEM analyses in section 7.2 show that the expected stresses are far below the limit of the material, so it is more critical to optimise the heat transfer towards the cooled base.

Finally, it must be noted that only one sample was tested for each condition. This generates big uncertainties in the results due to low repeatability of the printed parts, especially in such small scale where crack dimensions and other imperfections are more significant.

11.2 Wicking capacity

The maximum LL supply rate achievable is 9 $l/s \cdot m^2$ for the conventional design, 10.7 $l/s \cdot m^2$ for the V-shape design and 23.7 $l/s \cdot m^2$ for the tree design. The estimations show that in every case this flow is at least four orders of magnitude higher than the estimated loss rate caused by plasma exposure ($2.42 \cdot 10^{-4}$ $l/s \cdot m^2$). As mentioned in section 7.1, the geometry of the PFS and the dimensions of the texture have a big effect on the supply rate. In addition, the fact that the channels have 4 mm separation at the base gives the tree design the highest wicking capacity.

In the design proposed by P. Rindt [19] the LL supply rate is around 0.4 $l/s \cdot m^2$, and calculations done for the three prototypes show that this flow is increased by a factor of 20 and 60 for the conventional and tree designs respectively. The changes introduced in the three printed targets, such as the elliptic profile of the wicking channels, the smaller surface texture or the reduction of the brush sizes (thus increasing the channel density) have successfully resulted in an increase of the wicking capacity.

The supply rates of the prototypes seem too high to be realistic, but they have been obtained using the analytical model proposed by P. Rindt. To check whether these flows are possible, a back of the envelope calculation can be done using the images from **Figure 8-4**: the distance from the wetted PFS to the ventilation hole is 19 ± 6 mm, and the time to fill the target was 0.6 ± 0.1s. This results in a wicking speed of 20-50 mm/s which is equivalent to a supply rate of 20-50 $l/m^2 \cdot s$. Care must be taken when using this number given the big uncertainties linked to the result, but it is of the same order of magnitude than the estimated supply rates of the prototypes, concluding that these can indeed be realistic values.

During the experiments at Magnum-PSI, the PFS of the three targets remained wetted with LL throughout all the shots at high heat flux, which indicates that the wicking capacity was enough. Despite this result, exposures at higher heat fluxes will be necessary to find the limits of the wicking potential and longer shots of the order of minutes will allow to determine if the elliptic profile of the channels is effective when the targets start to run out of lithium.

11.3 FEM analyses

Simulations of the three targets were performed to estimate the behaviour of the prototypes during the plasma discharges. The three designs were simulated without lithium to analyse the worst case scenario, which would happen in case the targets dried out. Results show that after 10s under a peak heat flux of 15 MW/m^2 the targets would reach temperatures very close to the melting point, but that stress levels are very low compared to the limits of the material found with the tensile tests (below 30% of the material limit). If the geometry restrictions imposed by Magnum-PSI are not considered (e.g. external walls), the maximum Von Mises stress in the internal structure is around 8% of the material limit for peak temperatures of more than 2500ºC. The induced thermal

stresses caused by the expansion of the tungsten in the tested prototypes would be even smaller as the highest temperature measured at the PFS was around 625ºC.

The performance of the designs is considered as valid since the main goal of the internal structures is to minimize the stresses and optimize the LL flow towards the surface. These targets were conceived to operate with LL, so the temperature is not the main concern as it is expected that the Li on the PFS protects the tungsten during the plasma exposures. **Figure 9-13.a** shows how this is correct since a temperature plateau is reached with every target between 2000-2700ºC lower than the values seen in the FEM analyses.

The simulations include several assumptions regarding the properties of the printed tungsten, such as the coefficient of thermal expansion, the specific heat capacity or the density. These parameters have not been determined at high temperature for the printed W and it was decided to use the values provided by Smit Röntgen when possible and those of the conventional pure tungsten for the missing thermal properties. It was also decided that the limit of the material would be the fracture strength reached by the stress relieved tungsten with a safety factor of 1.2 (225 MPa). If all the correct properties of the printed tungsten had been measured at high temperature, the peak stresses and temperatures observed in the FEM analyses might have been slightly different. Nonetheless, the design of the targets would not have been altered since the stresses in the structure are at least one order of magnitude lower than the material limits.

11.4 Lithium balance

During the filling, more Li than expected was stored in the targets. Some causes that could explain the presence of this extra Li are that the dimensions of the printed structures could be slightly different than the specified in the CAD file or that because of the 6% porosity some LL diffused inside the bulk material, increasing the storage capacity. In addition, the estimations done with the CAD file did not take into account the Li attached to the outside walls of the targets or the base. A back of the envelope calculation shows that if all this extra Li was on the outside surfaces, the LL layer would be 250 µm for the exposed V-shape and around 100 µm for the conventional and tree designs (see Appendix E), which seems like a realistic option after looking the wetted targets in **Figure 8-5**. It must be noted that the exposed V-shape target was not weighed before the filling and the same dry weight as the first pre-loaded V-shape was used (see Appendix E). If the exposed V-shape was 0.2g heavier than the weighed one, this LL layer would be about 0.118 µm instead of 250 µm. The fact that the exposed V-shape was not weighed before the filling could have a small impact on the value of the stored Li but it does not affect the calculation of the lost Li.

An assumption is made that all the weight difference measured before and after the experiments at Magnum PSI was caused by the loss of lithium stored inside the targets. This was because no major damage caused by the plasma is detected on the PFS surface, neither by direct observation nor with the images from the SEM.

Results show that the three designs lost more Li than the predicted with the loss rate expression. One reason for this is that some LL leaked out of the targets through the ventilation hole and covered big part of the clamping rings as can be seen in **Figure 9-2**. Another cause that could have increased this loss are all the ejected particles seen during the cleaning shots (see **Figure 9-14)**. Finally, the conventional and the V-shape models lost around 0.5g more lithium than the tree design (about 1 cm^3 more of LL). One explanation for this can be that during the cleaning shots, a big LL droplet fell from the surface of the two first targets while this did not happen for the tree prototype (see **Figure 9-8**). This would mean that out of the 0.72g and 0.76g lost by the conventional and V-shape designs, around 0.5g would have been because of this big drop, and the other 0.22-0.26 would have been caused by the leakage through the ventilation hole and the

sputtering and evaporation happening on the PFS. Notice as well that the V-shape target was exposed to the plasma under a magnetic field of 1T and 1.3T whereas the other two were tested at 1T or 1.3T. This implies that the V-shape was facing the high power plasma during more time, thus increasing the loss of LM either through the PFS or the ventilation hole.

11.5 Optical emission spectroscopy

The results obtained by the multichannel spectrometer show that at low magnetic field (0.6T) the plasma did not have impurities or unexpected elements and the detected peaks were mainly Li and He during exposure at mode B and He and Ar during exposure at mode A and stand by.

The shots at higher magnetic field (1 and 1.3T) show more peaks of Li, He and Ar and with higher intensity, which is a logic result. In **Figure 9-7** there are two lines that could be W (c) and Mo (d). However, this is very unlikely because the plasma is too cold to sputter these elements. In addition, these lines are not present in the shot to the dummy at 1.3T, which means that they are only detected when there is also Li (notice that in both cases the lines are next to a Li peak). This suggests that maybe they are shifted Li lines, which can sometimes happen with this instrumentation.

Measurements at high magnetic field also show numerous lines of Fe together with some characteristic wavelengths of Mg, K and Cu. These last two ions are carefully monitored during the experiments at Magnum since they are a good indicator of the source's condition. When high peaks appear from both metals it means that the source is reaching the end of its lifespan and should be replaced. This is probably one of the main causes why higher heat loads could not be reached with the chosen settings.

Another interesting result found with the shots at 1T and 1.3T is the profile of the spectra during exposure. Typically, the peaks that correspond to the measured element rise from an almost horizontal line that is close to 0, like it is seen with the measurements at 0.6T. But for the measurements at higher magnetic fields, these horizontal lines are instead a continuum that is usually way above 0, reaching sometimes values between 1000-2000 counts. It is unclear of why this phenomenon happens.

11.6 IR thermography

The pyrometer was pointing at the center of the exposed target and was used to calibrate radiometry settings of the IR camera using the tungsten dummy. The temperatures obtained from the IR camera are highly dependent on the values set in the radiometry parameters. Literature was used to set the emissivity of the printed tungsten, which is assumed to be the same as for conventional tungsten filaments. Because of the 3D printing process, the tungsten dummy does not have a perfectly flat surface even though it was post processed with EDM. As for the LL, it is very difficult to fix a unique value since the motion of the LM or the fact that some particles might be trapped in it affect the emissivity of the material. All this can alter the temperature readings since they depend on the radiometry parameters.

Images during the cleaning shots at 18 MW/m^2 on the target reveal that the wetting was effective since LL started to expand across the surface. Nonetheless, this wetting was not completed after the shot and continued during the exposure at higher power. This suggests that maybe for future experiments the cleaning shots should be done with the same plasma settings but with longer exposures. Higher power loads are not desirable during the cleaning since the LL is not spread all over the PFS and the protection it provides is not yet fully effective.

Images of the high-power exposures show no dry areas on the PFS, which indicates that the designed wicking structures for the three prototypes are effective. Measurements of the top surface of the prototypes show a peaked temperature plateau around 625ºC while the dummy reached 1054ºC. Considering the fact that the PFS of the designs is at 17 mm from the cooled base while the dummy is 3 mm high, it can be stated that the LL bed is an effective protection for the tungsten. In addition, this low temperature plateau combined with the images from the Phantom camera (see **Figure 9-16**) strongly suggest the presence of the vapour shield in the interface between the PFS and the plasma beam.

Similar results were observed in the experiments performed by P. Rindt [2]. Cleaning and wetting of the PFS were also effective at 0.6T shots with He plasma and a temperature plateau around 700-800ºC is observed for peak heat loads of 14 MW/m^2 at the target. The temperature plateau of the printed targets was slightly lower, around 625ºC. There are several reasons that can cause this difference in the temperature plateau, such as the different thermal characteristics of the two designs (properties, structure, etc.) or a different calibration used for the IR camera. Finally, another difference between the experiments that can cause this temperature gap are the plasma conditions: the source used for both experiments was not the same, and in the tests with the printed targets the source was not performing optimally as it was reaching the end of its lifetime.

Tests performed with the printed prototypes have also confirmed that the textured surface is a more effective CPS than a mesh to confine the LL and keep the surface wetted. The mesh also caused additional problems such as swelling of the wires or even melting [2].

11.7 Phantom camera

The images from **Figure 9-14** show that the surface cleaning was effective since a lot of particles were ejected from the PFS during the first melted regions on the surface. The profile of the emitted light is irregular and LL drops can be identified moving on the PFS.

During the exposure at higher heat loads (27-30 MW/m^2 at the source, around 17 MW/m^2 estimated at the targets) a steady state is reached after a few seconds. After this point, no droplets are seen on the PFS and almost no sputtering is detected in the images. In addition, the steady and regular profile of the emitted light seen for every prototype (see **Figure 9-16**) indicates what could be a Li vapour cloud. The thickness of this profile was measured and it is bigger than the Li seen on the external wall of the targets after exposure (see **Figure 9-17**), being the first around 4 mm and the second 2.8 mm for the V-shape target. In addition, the emitted light has the same dimensions for every target whereas the Li on the side walls did not have the same profile for every design.

11.8 SEM images

Images of the printed targets show that the textured surface, despite having some cracks and dust, is very similar to the design from the CAD file. The only noticeable difference is the size of the blocks laying on top of the brushes, which are around 50% smaller than the designed ones. This increases the separation between them from 50 µm to 100 µm, but this is still small enough to pull the LL towards the PFS and confine it with the action of the capillary forces. Besides the dimensions, the printed blocks are also slightly circular while the design specifies square geometries. According to the wicking flow model, this is not optimum for the movement of the LL on the textured brushes since the separation between the blocks can increase in some areas, but the difference is so small that the impact is almost negligible.

Surface scanning of the cleaned tree prototype shows that the ultrasound bath is an effective method to remove particles from the surface, although some still accumulate around the blocks.

SEM images after filling the targets show that the PFS was mainly wetted by wicking of the LL between the blocks and not by direct deposition during the LL bath. This can be seen in **Figure 9-21**, where most of the wetted area is surrounding the channels between the brushes of the V-shape design. No isolated wetted regions are detected in the middle of the brush as a result of the LL bath.

After the experiments, images taken with the electron microscope show that the layer of LL is slightly thinner in the center of the targets than at the edges because the visible tungsten blocks are bigger at the center. This could be possible during exposure since the plasma beam has a Gaussian profile, but when the shot ends the LL layer should homogenize again. It is unclear why this result is observed.

In the last phase, the Li was removed from the targets and the PFS was checked again. Even though some blocks could have been eroded during the exposure, the biggest part of the texture is intact, including the central brushes of the V-shape and the conventional designs that were facing the peak of the heat flux. The tree prototype is the one with the most damaged surface, but it is unclear whether most of the blocks were broken during transport and manipulation of the target, or during plasma exposure, since in the photo taken before the preparation of the samples there are already many blocks missing (see **Figure 9-24.a**). Remember that these parts are around 140 μm wide, so the relative density achievable according to Smit Röntgen is about 82% (Appendix A), making the material weaker as seen in the results of the material characterization.

11.9 Neutron radiation

To conclude this discussion, it should be reminded that neutron effect on the target has not been considered in this project. Liquid lithium is an effective protection against the plasma ions but it cannot prevent the neutrons from reaching the bulk material. If the targets were exposed for longer time under fusion plasmas, the tungsten could suffer from irradiation problems such as embrittlement or heat conductivity reduction. Increasing the working temperature of the tungsten until it reaches recrystallization is a possible solution to partially recover the neutron damage [7]. For tungsten, recrystallization starts around 1150ºC [37].

The pre-loaded LLD targets tested by P. Rindt reached a temperature plateau between 700-800ºC [2], and the plateau in this project was around 625ºC. With such configurations, it has not been demonstrated that it is possible to operate at temperatures where the tungsten can recrystallize. In addition, if such temperatures could be reached, the loss rate of Li would increase due to the proximity to its boiling point (1330ºC), so maybe tin would be a better alternative for the LM given its higher boiling temperature (2600ºC).

Nonetheless, stress levels seen in the simulations and temperatures reached in the experiments at Magnum-PSI open the possibility to rethink the bulk material's choice. Maybe a material with better resistance against neutron radiation could be 3D printed with the proposed structure instead of tungsten. This new alloy could have, for example, a lower recrystallization temperature so that it would still be possible to use LL on the PFS while the divertor target would operate in the recrystallization regime of the solid.

12 CONCLUSIONS

Additive manufacturing is a fabrication method with big potential, allowing the designed components to have complex internal structures and a high degree of detail without affecting the time or cost of the printed part. The goal of this project is to combine the liquid lithium divertor concept with the 3D printed tungsten and demonstrate its feasibility under fusion-relevant conditions. To answer this question, three prototypes were designed, manufactured and tested under fusion-relevant conditions at Magnum PSI.

The novelty of the designed concepts lies on their internal structure: it is optimised to reduce the thermal stresses induced by the heat loads and to enhance the capillary action that drives the LL towards the PFS. FEM simulations show a reduction of up to two orders of magnitude of the induced stresses when compared to the solid tiles proposed so far, and LL flow calculations indicate an increase by a factor of 20 when compared to the LLD proposed by P. Rindt [19].

Results of the experiments performed at Magnum-PSI indicate that the three designs survived 10s exposures to plasma with peak heat fluxes up to 30 MW/m^2 measured at the plasma source, estimated around 17.5 MW/m^2 at the target surface. The lack of dry spots on the PFS or droplet ejections indicate that the LL flow was sufficient and the surface texture was effective to confine the Li. Furthermore, the temperature plateau observed during the exposures, with the maximum temperature being 625ºC, suggests that the LL is an effective solution to protect the bulk material from the plasma.

This encourages future research in the 3D printed LLD, which should include optimization of the bulk material and further analyses of the designed components since it was not possible to find their limits. In addition, the significant stress reduction and the low temperature measured during the exposures open the opportunity to explore new materials for the 3D printed LLD concept which could have higher resistance against neutron radiation. This could be for example some engineered alloy with a lower recrystallization temperature.

13 FUTURE WORK

In this section, ideas that could not be carried out during the project will be presented as well as proposals to be investigated after seeing the effectiveness of the 3D printed tungsten.

13.1 Research within this project

As a direct continuation of the current project, more investigation could be done to further study and optimize the 3D printed tungsten and more experiments could be planned with the prototypes to determine their limits regarding the peak heat flux and the length of the exposures.

13.1.1 Material analysis

More data is necessary from the printed tungsten to know how it can be optimised for fusion applications. For example, maybe recrystallized specimens show better thermal diffusivity than the stress relieved, thus resulting in higher thermal conductivity. For this reason, the first suggestion would be to complete the material test plan proposed in section 3.1, including all the repetitions to reduce the deviation.

Results suggest that thermal treatment can improve the behaviour of the material. For this reason, a recommendation would be to test additional heat treatments with different temperatures and times and see if the strength and/or thermal diffusivity increase. Another option to optimize the material could be to improve the printing atmosphere by reducing the concentration of impurities inside the chamber since some darker regions were detected in the printed parts. By testing new conditions and improving the printing environment it might be possible to increase the strength of the printed tungsten, which could reduce the potential damage on the texture of the PFS.

A common fact among 3D printed materials is that they are not good against fatigue. If printed tungsten is to be placed as PFM in a fusion reactor, it will have to stand repetitive thermal loads. No analysis of the material has yet been done under dynamic loads, which is why another suggestion would be to test the printed tungsten in these conditions.

13.1.2 Prototypes

Machine time at Magnum PSI was limited, so it was not possible to perform all desired tests on the three printed designs. Future campaigns could include exposing the targets without Li to plasma to better determine the protective effect the liquid metal has on the bulk material. In addition, the pre-loaded prototypes should also be exposed to higher heat loads to find the limits of the designs in terms of the wicking capacity to the PFS, the maximum temperature reached and the damage done to the surface texture. Another interesting test would be to increase the exposure time to the order of minutes and study the LL loss rate.

A recommendation for future experiments would be to make a good overview analysis of the entire PFS before and after the tests with a light microscope. This would allow to compare the surface brush by brush and know for sure if the damage is caused by the exposure at the plasma or by the manipulation of the targets.

Finally, other fusion-relevant liquid metals could be introduced in the prototypes instead of the Li, such as Sn, to compare their effectiveness in protecting the bulk material.

13.2 Research beyond this project

Measurements during the experiments at Magnum PSI have showed that peak temperatures of the printed targets were always kept reasonably low. Since the stress requirements and the high melting temperature that characterizes the tungsten are no longer necessary when there is a layer of LL on the PFS, one possibility that could be studied is to print the divertor targets with other metals and alloys that can handle better the neutron load.

Experiments have proven that a 3D printed target with LL on the PFS can survive fusion-relevant heat loads. If a LL divertor is to be installed in a reactor, it will be necessary to design a pumping system to allow for continuous operation of the machine and not make it dependant on the amount of LL inside the reservoir. In addition, a recirculating and filtering system will have to be developed to solve the problem of fuel retention in the LM when operating with H plasmas.

Finally, the concepts developed in this project could also be implemented in other sectors besides the fusion world, especially in systems that have to stand extreme heat loads. One example would be the MHD generators where LL confined in a printed CPS could be used in the inner face of the components that are facing the plasma.

14 REFERENCES

[1] O. M. Wirtz. "Thermal shock behaviour of different tungsten grades under varying conditions". PhD dissertation approved by the RWTH Aachen University, 2012.

[2] P. Rindt et al. "Testing of a pre-loaded liquid lithium divertor target on Magnum-PSI". Conference in the 16th International conference of Plasma-Facing Materials and Components for fusion applications (PFMC-16), Neuss, Germany, 2017.

[3] BP Statistical Review of World Energy (2016). *BP Statistical Review of World Energy 65th Edition.* London (United Kingdom).

[4] World Data Bank website (22/11/2016): http://databank.worldbank.org/data/reports.aspx?source=health-nutrition-and-population-statistics#

[5] Kyoto protocol to the United Nations framework. Convention on climate change. Document available at the United Nations website (05/12/2016): http://unfccc.int/resource/docs/convkp/kpeng.pdf

[6] ITER website (01/12/16): https://www.iter.org/sci/Fusion

[7] J. H. You et al. "European DEMO divertor target: Operational requirements and material-design interface". *Nuclear Materials and Energy 000,* 1-6, 2016.

[8] F.L. Tabares et al. "Reactor divertor designs based on liquid metal concepts". *EuroFusion Preprints*, 2016.

[9] MIT Plasma Science and Fusion Center YouTube Channel (22/03/2017): https://www.youtube.com/watch?v=R_aQECVvzSY

[10] A.B. Martin-Rojo et al. "Exposure of liquid lithium confined in a capillary structure to high plasma fluxes in PILOT-PSI—Influence of temperature on D retention". *Fusion Engineering and Design XXX (2016),* 2016.

[11] M. Ono et al. "Active radiative liquid lithium divertor concept". *Fusion Engineering and Design 89*, 2838-2844, 2014.

[12] V.A. Evtikhin et al. "Technological aspects of lithium capillary-pore systems application in tokamak device". *Fusion Engineering and Design 56-57*, 363-367, 2001.

[13] P. Fiflis et al. "Wetting properties of liquid lithium on select fusion relevant surfaces". *Fusion Engineering and Design 89*, 2827–2832, 2014.

[14] G. Mazzitelli et al. "Review of FTU results with the liquid lithium limiter". *Fusion Engineering and Design 85*, 896–901, 2010.

[15] Z. Sun et al. "Development of and experiments with liquid lithium limiters on HT-7". *Journal of Nuclear Materials 438,* S889-S904, 2013.

[16] J. Ren et al. "A flowing liquid lithium limiter for the Experimental Advanced Superconducting Tokamak". *Review of scientific instruments 86,* 023504, 2015.

[17] I. Lyublinski et al. "Module of lithium divertor for KTM tokamak". *Fusion Engineering and Design 87*, 1719-1723, 2012.

[18] M. Ono et al. “Recent progress in the NSTX/NSTX-U lithium programme and prospects for reactor-relevant liquid-lithium based divertor development”. *IOP Publishing – Nuclear Fusion 53*, 2013.

[19] P. Rindt et al. “Conceptual design of a pre-loaded liquid lithium divertor target for NSTX-U”. *Fusion Engineering and Design 112*, 204-212, 2016.

[20] G. De Temmerman et al. “High heat flux capabilities of the Magnum-PSI linear plasma device”. *Fusion Engineering and Design 88*, 483-487, 2013.

[21] G. G. van Eden et al. “Self-regulated plasma heat flux mitigation due to liquid Sn vapor shielding”. *Physical review letters 116, 135002*, 2016.

[22] Smit Röntgen website (24/07/2017): http://smitroentgen.com/

[23] D.N. Ruzic et al. “Lithium-metal infused trenches (LiMIT) for heat removal in fusion devices”. *Nuclear Fusion 51*, 102002 (4pp), 2011.

[24] F. L. Tabarés et al. “Reactor Divertor designs based on Liquid Metal Concepts”. Conference in the 16th meeting of the General Assembly EUROFUSION, Madrid, Spain, 2016.

[25] V. A. Evtikhin et al. “Calculation and experimental investigation of fusion reactor divertor plate and first wall protection by capillary-pore systems with lithium”. *Journal of Nuclear Materials 271&272*, 396-400, 1999.

[26] M. A. Jaworski et al. “Liquid lithium divertor characteristics and plasma-material interactions in NSTX high-performance plasmas”. Princeton Plasma Physics Laboratory (PPPL), USA, 2013.

[27] V. A. Evtikhin et al. “Research of lithium capillary-pore systems for fusion reactor plasma facing components”. *Journal of Nuclear Materials 307-311*, 1664-1669, 2002.

[28] T. F. Lin et al. “Capillary wicking of liquid lithium on laser textured surfaces for plasma facing components”. *Journal of Nuclear Materials 433*, 55-65, 2013.

[29] T. W. Abrams. “Erosion and re-deposition of lithium and boron coatings under high-flux plasma bombardment”. PhD dissertation presented to the faculty of Princeton University, USA, 2015.

[30] S. J, Zinkle. “Summary of physical properties for lithium, Pb-17Li and /LiF)$_n$·BeF_2 coolants”. APEX study meeting, Sandia National Laboratory, USA, 1998.

[31] J.F. Despois and A. Mortensen. “Permeability of open-pore microcellular materials”. *Acta Materiala 53*, 1381-1388, 2004.

[32] EMPA website (20/07/2017): https://www.empa.ch/web/coating-competence-center/selective-laser-melting

[33] S. Bai et al. “Femtosecond fiber laser additive manufacturing of tungsten”. *SPIE Photonics West 9738-24*, 2016.

[34] DIFFER website (31/07/2017): https://www.differ.nl/research/fusion-facilities-and-instrumentation/magnum-psi

[35] T. Palacios et al. “Mechanical degradation of tungsten alloys at extreme temperatures in vacuum and oxidation atmospheres”. Conference in the Materials Modelling and Simulation for Nuclear Fuels (MMSNF), Chicago, USA, 2013.

[36] T. M. Mower and M. J. Long. “Mechanical behaviour of additive manufactured, powder-bed laser-fused materials”. *Materials Science & Engineering A 651,* 198-213, 2016.

[37] S. Sharafat et al. “Design window for tungsten alloys”. APEX study group meeting, PPPL, USA, 1999.

[38] W. E. Luecke and J. A. Slotwinski. “Mechanical properties of austenitic stainless steel made by additive manufacturing”. *Journal of Research of the National Institute of Standards and Technology 119,* 2014.

[39] A. Warren et al. “Oxidation of tungsten and tungsten carbide in dry and humid atmospheres”. *International Journal of Refractory Metals & Hard Materials 14, 345-353,* 1996.

[40] T. Furumoto et al. “Permeability and strength of a porous metal structure fabricated by additive manufacturing”. *Journal of Materials Processing Technology 219, 10-16,* 2015.

[41] G. L. Kulcinski et al. “The effect of porosity and pore interconnection on the thermal conductivity and electrical resistivity of tungsten”. *Journal of the Less-Common Metals 7, 383-392,* 1964.

[42] Autodesk Netfabb website (12/09/2017): https://www.autodesk.com/products/netfabb/overview

[43] nTopology website (12/09/2017): http://www.ntopology.com/

[44] Table of total emissivity by Omegascope (17/07/2017). PDF available at: http://www.omega.com/temperature/Z/pdf/z088-089.pdf

[45] Emissivity tables for IR thermometer calibrations by Scigiene (17/07/2017). PDF available at: http://www.scigiene.com/pdfs/428_InfraredThermometerEmissivitytablesrev.pdf

[46] GRAFTECH Inc. “GRAFOIL Flexible Graphite, Engineering design manual”, 2nd edition. Cleveland, USA, 2002.

[47] Lithium Metal UK website (11/09/2017): http://www.lithiummetal.co.uk/index.asp

APPENDIX A – Technical Datasheet 3D printed tungsten by 02/2015

smit RÖNTGEN

Tungsten Powder Bed Laser Fusion Technical Datasheet

Technical Datasheet				
Technical Data:				
Typical part accuracy	(solid X-Y plane)	for parts <60mm for parts >60mm and <120mm for parts > 120mm	±25 ±35 ±50	µm µm µm
Typical part accuracy	(z- plane)	min	+100	µm
		max	+300	µm
Minimum geometry size			100	µm
Maximum build size	LxWxH	23 x 23 x 10cm Builds > 10cm require powder re-supply.		cm
Mechanical Properties				
Surface roughness	As-Built Post processed#	Ra Ra	13-14 <3.2	µm µm
Hardness*		Vickers	>150	HV30
Ultimate Tensile strength*			>35	MPa
Young's modulus			50	GPa
Physical Properties				
Density See also graph after this datasheet See also graph at the end of this table	Relative* Absolute*		>97 >18,6	% g/cm^3
Electrical Resistivity*			<250	nΩm
Thermal Diffusivity*			40-55	mm^2/s
Heat capacity			0.16	J/(gK)

Thermal conductivity*		120-170	W/(mK)
Air Tightness	Depending on material thickness 100% air thightness can be achieved. Thin walled products can only be made airtight by sealing.		
Material Composition Powder			
W		>99	%
*Depending on layer thickness and part geometry (solid parts only) #Effect and availability of post processing depending on part geometry			
Post Processing Characteristics			
Abrasive characteristics	Solid material can be polished to specular reflection		
Machining Characteristics	Material can be milled, drilled with standard hard-metal tooling.		
Chemical Resistance	Depending on application		

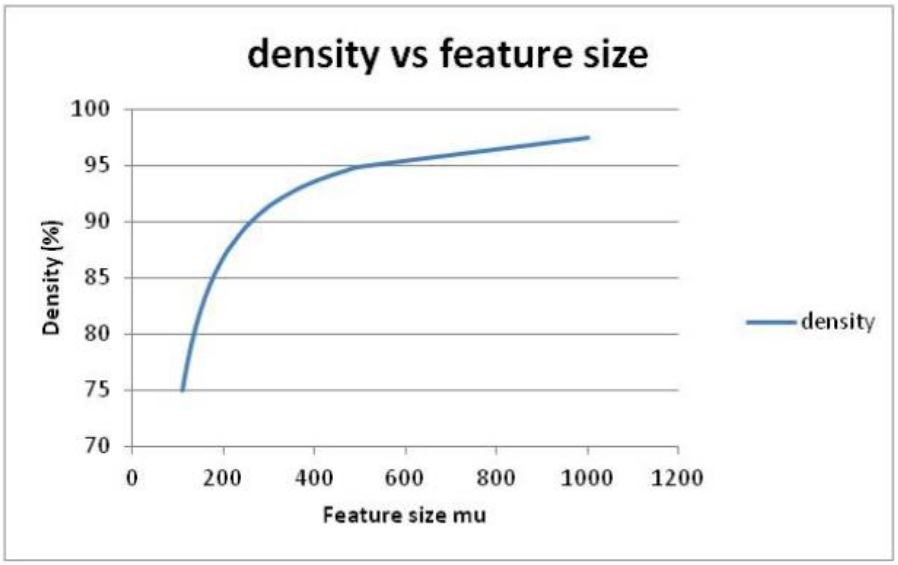

Density relative to 19,25 g/cm-3

Important Notice!

Due to the nature of the powder bed laser fusion process, material characteristics strongly depend on the part design. Therefore the **values below can only be used for guidance and are subject to change**.
Final values to be determined in collaboration with Suppliers Engineering team

APPENDIX B – Specimens used in the material characterization

The following drawings show the dimensions of the samples used for the material characterization. The surface roughness of the printed parts was Ra 13 µm, and the samples that were post processed with EDM reached a roughness around Ra 3.2 µm according to the manufacturer. All dimensions are in mm.

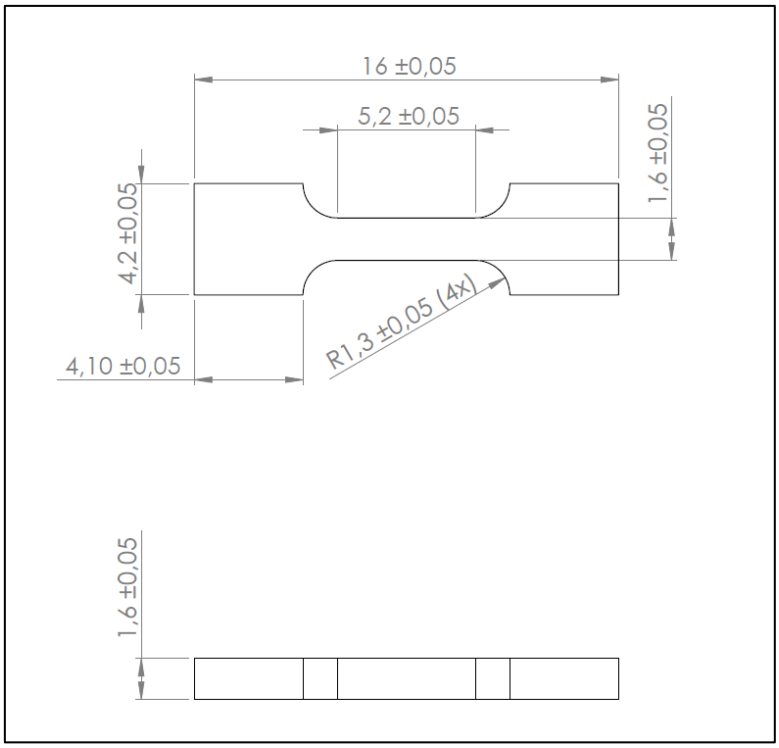

Figure B-1 *Technical drawing of the tensile specimen used for the tensile tests.*

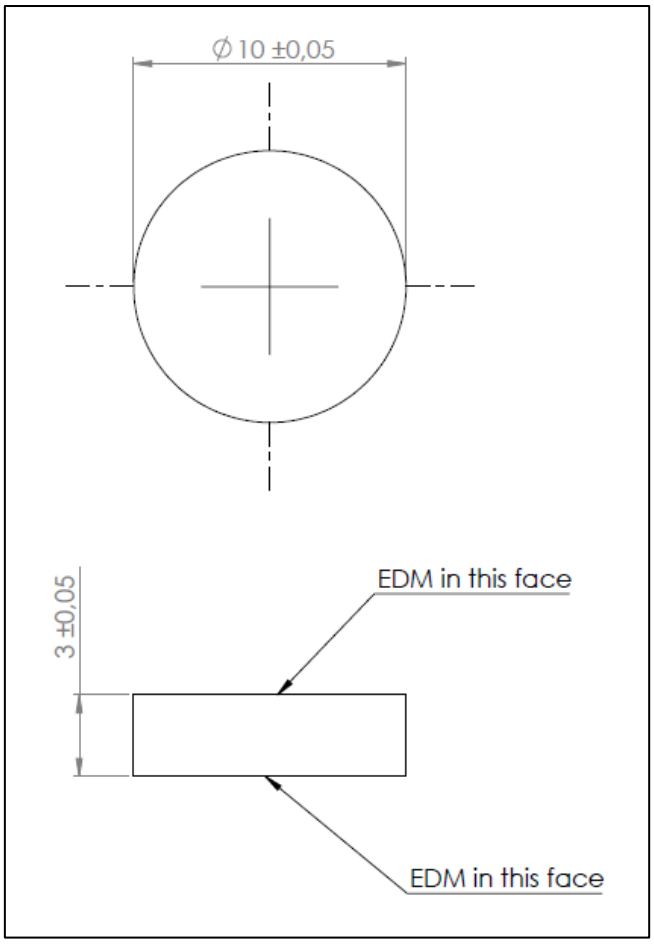

Figure B-2 *Technical drawing of the disc used for the laser flash analyses.*

APPENDIX C – Properties used to estimate the LL supply rate

As a reminder, the expression used to calculate the wicking flow towards the plasma facing surface of the targets is the following:

$$\dot{Q} = \frac{2 \cdot \gamma \cdot cos\alpha / r_u - 2 \cdot \gamma \cdot cos\alpha / r_l}{R_{tot} + \sigma \cdot B^2 \cdot \sum_{i=1}^{n} L_i / A_i} \; ; \; where \; R_{tot} = \sum_{i=1}^{n} R_i = \sum_{i=1}^{n} \frac{\mu \cdot L_i}{k_i \cdot A_i}$$

The following table summarises the properties and values used for the calculation.

Table C-1 *Properties and values used for the estimation of the LL supply rate of the designed targets. The temperature unit in the expressions is Kelvin.*

Property	Units	Expression / Value
Temperature (T)	K	873 K
Surface tension of LL (γ) [30]	N/m	$0.398 - 0.147 \cdot 10^{-3} \cdot T = 0.2697$ N/m
Contact angle LL-W (α) [13]	deg	70º
Elec. resistivity of LL (ρ_e) [30]	nΩ·m	$-64.9 + 1.064 \cdot T - 1.035 \cdot 10^{-3} \cdot T^2 + 5.33 \cdot 10^{-7} \cdot T^3 - 9.23 \cdot 10^{-12} \cdot T^4 = 424.4$ nΩ·m
Elec. conductivity of LL (σ)	S/m	$1/\rho_e = 2.356 \cdot 10^6$ S/m
Magnetic Field (B)	T	1
Dynamic viscosity of LL (μ) [30]	Pa·s	$\ln(\mu) = -4.164 - 0.6374 \cdot \ln(T) + 292.1/T = 2.899 \cdot 10^{-4}$ Pa·s
Permeability of LL (k) [19]	m^2	$2 \cdot r_p/3$

The geometry of the PFS was different for every design. The following table shows the parameters used for the calculation:

Table C-2 *Values used in the LL supply rate estimation for the characteristic parameters of the surface geometry of the designed targets.*

Parameter	V-shape	Conventional	Tree
Number of brushes on the surface	27	82	76
Maximum distance covered by the LL on the surface*	1.7 mm	0.75 mm	1 mm
Wicking channels in the same direction on top of the brushes	12	7	7
Height of the surface blocks	0.1 mm	0.1 mm	0.1 mm
Separation between blocks**	50 & 100 μm	50 & 100 μm	50 & 100 μm

* The maximum distance covered by the LL was considered as the minimum separation between the edge of the brush and its center.

** The 50 μm separation is for the flow calculations of the CAD design and 100 μm is for the flow of the real printed targets.

APPENDIX D – Properties used to estimate the heat flux density reaching the targets

Table D-1 *Material properties used in the FEM analysis of the dummy disc done to estimate the peak heat flux that reached the targets when the TS measured 30 MW/m^2 at the source.*

Property	Molybdenum	3DP Tungsten	Grafoil	Copper
Young's Modulus (MPa)	$3.2 \cdot 10^5$ *	3692 **	2000 [46]	$1.1 \cdot 10^5$ *
Poisson's ratio	0.38 *	0.28 *	0.394 [46]	0.37 *
Density (kg/m^3)	10000 *	17900 ***	1120 [46]	8900 *
Yield strength (MPa)	200 *	225 **	30 [46]	394.3 *
Coefficient of Thermal expansion (K^{-1})	$5.6 \cdot 10^{-6}$ *	$5.5 \cdot 10^{-6}$ ***	x – $4 \cdot 10^{-7}$ y – $4 \cdot 10^{-7}$ z – $2.7 \cdot 10^{-5}$ [46]	$2.4 \cdot 10^{-5}$ *
Thermal conductivity (W/m·K)	110 *	109	x – 120 y – 120 z – 5 [46]	390 *
Heat Capacity (J/kg·K)	270 *	160 ***	850 [46]	390 *

* From the material database of SolidWorks

** From the material characterization done in this project

*** From the technical datasheet provided by Smit Röntgen (Appendix A). The density in the table is the 93% of the absolute density (19.25 g/cm^3) since the disc had a 7% porosity.

The thermal conductivity at 600ºC was calculated using the following expression:

$$k = \rho \cdot C_p \cdot \alpha = 17900 \cdot 160 \cdot 38 = 109 \text{ W/m·k}$$

The density and the heat capacity were obtained from the datasheet provided by Smit Röntgen, and the thermal diffusivity was measured in the material characterization. In this case, the density and heat capacity are the values for room temperature, but according to M. Wirtz the density of pure W at 600ºC is 0.8% lower while the specific heat capacity increases by 3%.

APPENDIX E – Weight measurements used for the Li balance

Table E-1 *Weight measurements and other intermediate calculations used during the lithium balance section.*

(g)	V-SHAPE 1	V-SHAPE 2	TREE	CONVENTIONAL
Dry target 1	110.47	-	102.47	121.55
Dry target 2	110.47	-	102.48	121.55
Dry target 3	110.47	-	102.48	121.55
Relative density*	93.6%		93.4%	93.5%
After filling 1	112.01	112.25	104.26	122.79
After filling 2	112.01	112.26	104.26	122.79
After filling 3	112.02	112.26	104.26	122.79
Total Li in the target	1.54	1.79**	1.78	1.24
Theoretical Li storage capacity (CAD files)	1.41	1.41	1.65	1.08
% filled	109%	126%	108%	115%
Extra Li mass	0.13	0.37	0.14	0.16
Extra Li volume (mm^3)	241.29	696.97	255.42	295.36
Height external Li layer (mm) ***	0.089	0.255	0.094	0.109
After experiments 1	-	111.38	103.93	122.07
After experiments 2	-	111.38	103.93	122.07
After experiments 3	-	111.38	103.93	122.07
Li lost	-	- 0.76	- 0.21	- 0.72
Li remaining (%)	-	58%	88%	42%

* Relative density calculated as the ratio between the measured weight of the printed targets and the theoretical weight provided by the CAD files, which assumes the material is 100% dense. Real relative density is slightly higher than these values since there was small damage on the targets during the transport and a few small blocks of the texture were missing. For these reasons, it was considered that the number provided by Smit Röntgen (94% dense) was valid.

** The V-shape 2 target, which is the one that was exposed to plasma, was not weighed before the filling. To determine the total Li stored it was assumed that the prototype had the same weight as the V-shape 1.

*** It was assumed that the inside of the targets was completely filled with Li and the rest was attached to the external walls. This term represents the height of the Li layer on the outside walls considering it was homogeneous for all the surfaces. The total external area is 2727.1 mm^2.

APPENDIX F – Economic study of the project

In this section, a rough estimation of the costs related to the project is presented. This study includes only the costs referred to the material characterization and experiments performed. No consideration is given to indirect costs such as electricity usage, daily transport or office material.

Table F-1 *List of the direct costs related to the project.*

	Term	Single cost	Amount	Total cost
MATERIAL CHARACTERIZATION	Print samples	3€/sample	11*	33€
	Heat treatment	350€/batch	2	700€
	Tensile test	430€/sample	7	3010€
	Laser Flash analysis	1100€/sample	3	3300€
TOTAL COST FOR MATERIAL CHARACTERIZATION				**7043€**
EXPERIMENTS AT MAGNUM-PSI	Print targets	102€/prototype**	4*	408€
	Sand blasting	35€/hour	0.25	9€
	Ultrasonic cleaning	25€/hour	1	25€
	Heat treatment	350€/batch	2	700€
	Lithium	100€/100g [47]	10	10€
	Glove box	100€/day	4	400€
	Grafoil	50€/sheet (DIN A4 size)	1/10 sheet	5€
	Magnum-PSI	18000€/day	2.5	45000€
	SEM analyses	300€/hour	4.5	1350€
TOTAL COST FOR EXPERIMENTS AT MAGNUM-PSI				**47916€**
TOTAL COST OF THE EXPERIMENTAL PART OF THE PROJECT				**54959€**

Unless indicated, the single cost of each term has been obtained from the contact person in charge of every institution, department or laboratory.

* More samples were printed, but in this table only the ones used for this project have been included. The other specimens for the material characterization and prototypes will be used in future campaigns.

** Estimated from the cost of the specimens used for the material characterization. The extrapolation has been done using the grams of tungsten used for the printed parts.